

Diss. ETH No. 27367

# NOVEL SCHEMES OF ATTOSECOND INTERFEROMETRY

A thesis submitted to attain the degree of  
DOCTOR of SCIENCES of ETH ZURICH  
(Dr. sc. ETH Zurich)

presented by  
JACO FUCHS

MSc Physics, Universität Stuttgart,  
born on 20.09.1993,  
citizen of Germany.

Accepted on the recommendation of

Prof. Dr. Ursula Keller, examiner  
Prof. Dr. Anne L'Huillier, co-examiner

2021



# Contents

<b>Contents</b>	<b>i</b>
<b>List of figures</b>	<b>v</b>
<b>List of tables</b>	<b>vii</b>
<b>List of symbols and acronyms</b>	<b>ix</b>
<b>Publications</b>	<b>xiii</b>
Journal papers . . . . .	xiii
Conference papers . . . . .	xiv
<b>Abstract</b>	<b>xvii</b>
<b>Kurzfassung (German)</b>	<b>xix</b>
<b>1 Introduction</b>	<b>1</b>
<b>2 Attosecond photoionization spectroscopy</b>	<b>7</b>
2.1 Attosecond pulse generation . . . . .	8
2.1.1 High harmonic generation . . . . .	8
2.1.2 Attosecond pulse train . . . . .	11
2.2 Attosecond pump-probe experiments . . . . .	12
2.2.1 Reconstruction of attosecond beating by interference of two-photon transitions (RABBITT) . . . . .	13
2.2.2 Photoionization time delays . . . . .	16
<b>3 Experimental setup</b>	<b>19</b>
3.1 Laser system . . . . .	19
3.1.1 Rainbow laser oscillator . . . . .	20
3.1.2 Chirped pulse amplifier . . . . .	21
3.2 Attosecond front-end . . . . .	22

3.3	COLTRIMS detector . . . . .	24
3.3.1	Momenta reconstruction . . . . .	26
<b>4</b>	<b>Angle-resolved attosecond interferometry</b>	<b>31</b>
4.1	Time delays from one-photon transitions in the continuum	33
4.1.1	Introduction . . . . .	34
4.1.2	Theoretical framework . . . . .	37
4.1.3	Experimental results . . . . .	40
4.1.4	Theoretical results . . . . .	43
4.1.5	Discussion . . . . .	45
4.1.6	Conclusion and outlook . . . . .	51
4.2	Derivation of the anisotropy parameters . . . . .	52
4.3	Analytic solution for the phase differences . . . . .	55
4.4	Investigation of larger atoms . . . . .	58
4.5	Outlook . . . . .	62
<b>5</b>	<b>Attosecond interferometry employing overlapping high harmonics</b>	<b>63</b>
5.1	Towards the complete phase profiling of attosecond wave packets . . . . .	65
5.1.1	Supplemental material . . . . .	76
5.2	Detailed derivation of the angle-resolved spectra . . . . .	79
5.3	Atto- and femtochirp in attosecond pulse trains . . . . .	81
5.4	Reconstruction of absolute phases . . . . .	84
5.5	Outlook . . . . .	88
<b>6</b>	<b>Free-running quantum interferometry</b>	<b>89</b>
6.1	Attosecond resolution from free running interferometric measurements . . . . .	91
6.1.1	Introduction . . . . .	91
6.1.2	The method . . . . .	95
6.1.3	Comparison between TURTLE and the sine-fit analysis . . . . .	96
6.1.4	Proof-of-principle experiment . . . . .	99
6.1.5	Conclusion . . . . .	100
6.2	Investigation of molecular photoionization time delays with TURTLE . . . . .	103
6.3	Outlook . . . . .	108
<b>7</b>	<b>Attosecond photoionization spectroscopy just above threshold</b>	<b>109</b>
7.1	Helium RABBITT measurement just above threshold . . . . .	110
7.2	Photoionization delays arising from the helium excited states resonances . . . . .	112
7.3	Stark effect . . . . .	113
7.4	Delays from one-photon ionization . . . . .	116
7.5	Outlook . . . . .	118
<b>8</b>	<b>Conclusion</b>	<b>119</b>

<b>Author contributions</b>	<b>123</b>
<b>References</b>	<b>125</b>
<b>Curriculum Vitæ</b>	<b>139</b>
<b>Acknowledgements</b>	<b>141</b>



## List of figures

2.1	Simple-man-model . . . . .	8
2.2	High harmonic spectrum . . . . .	9
2.3	Attosecond pulse train . . . . .	11
2.4	RABBITT . . . . .	13
2.5	Wigner scattering phase . . . . .	16
3.1	Layout of the laser oscillator . . . . .	20
3.2	Laser amplifier . . . . .	21
3.3	Attosecond pump-probe delay line . . . . .	23
3.4	COLTRIMS detector . . . . .	25
3.5	Experimental momentum spectra . . . . .	28
3.6	Experimental RABBITT spectrum in helium . . . . .	29
4.1	Schematic of the quantum path interference in helium . . . . .	35
4.2	Experimental anisotropy parameters of the time-resolved photoelectron angular distribution in helium . . . . .	41
4.3	Simultaneous fit of the sideband anisotropy parameters of helium . . . . .	44
4.4	Cc-phase difference between <i>s</i> - and <i>d</i> -partial waves for absorption . . . . .	46
4.5	Cc-phase difference between <i>s</i> - and <i>d</i> -partial waves for stimulated emission . . . . .	48
4.6	Delay and absolute phase offset between <i>s</i> - and <i>d</i> -partial waves . . . . .	50
4.7	Schematic of the quantum path interference in argon . . . . .	59
4.8	Experimental anisotropy parameters of the time-resolved photoelectron angular distribution in argon . . . . .	61
4.9	Simultaneous fit of the sideband anisotropy parameters of argon . . . . .	62
5.1	Illustration of the 1-2-quantum beat method . . . . .	68
5.2	Experimental asymmetry spectrogram . . . . .	69
5.3	Simulated asymmetry spectrogram . . . . .	72
5.4	Influence of periodic spectral phase oscillations on an APT . . . . .	75
5.5	Simulated photoelectron yield in for two-color photoionization . . . . .	77
5.6	Transition rates for the IR induced cc-transitions . . . . .	77
5.7	Atto- and femtochirp in attosecond pulse trains . . . . .	83
5.8	Scheme to retrieve absolute phases . . . . .	84
5.9	Absolute phase reconstructed from the SAE simulation . . . . .	87

5.10	Absolute phase reconstructed from the experiment . . . . .	87
6.1	Example RABBITT spectrum . . . . .	93
6.2	Illustration of the TURTLE method . . . . .	95
6.3	Precision of TURTLE and traditional sine-fitting . . . . .	97
6.4	Experimental RABBITT traces obtained by thermal drift . . . . .	99
6.5	Illustration of the TURTLE ellipse . . . . .	102
6.6	Theoretical acetylene photoelectron spectrum . . . . .	104
6.7	Experimental acetylene photoelectron spectrum . . . . .	105
6.8	Acetylene RABBITT spectra . . . . .	106
6.9	Turtle ellipse fits of the simultaneous acetylene-helium RABBITT . . . . .	107
7.1	Signatures of the helium $1snp$ -excited states in a RABBITT measurement	110
7.2	Sideband oscillations arising from the $1snp$ -excited states . . . . .	113
7.3	Energy shift of the helium $1s4p$ -signature . . . . .	114
7.4	Experimental anisotropy parameters of the helium RABBITT just above threshold . . . . .	115
7.5	Simultaneous fit of the anisotropy parameters for the helium RABBITT sideband 16 . . . . .	116
7.6	Phase differences between $s$ - and $d$ -partial waves just above threshold . . . . .	117



## List of tables

4.1	Algebraic values of the integrals for the derivation of the anisotropy parameters . . . . .	55
4.2	Phase difference between <i>s</i> - and <i>d</i> -partial waves in argon . . . . .	61
6.1	Adiabatic ionization potentials of acetylene . . . . .	105
6.2	Acetylene-helium delay retrieved with Turtle . . . . .	106
7.1	Time delays between the helium excited states signatures . . . . .	113



# List of symbols and acronyms

## Symbols

$A$	vector potential
$\alpha$	electron emission angle
$B$	magnetic field
$c$	speed of light in vacuum
<i>c.c.</i>	complex conjugated
$E$	electric field
$e$	elementary charge
$E$	energy
$E_{cut-off}$	cut-off energy
$E_H$	Hartree energy
$E_{kin}$	kinetic energy
$E_{XUV}$	XUV photon energy
$\epsilon_0$	vacuum permittivity
$f_{CEO}$	carrier-envelope offset frequency
$f_{rep}$	repetition rate
$h$	Planck constant
$\hbar$	reduced Planck constant
$I$	intensity of electromagnetic field
$I_p$	ionization potential
$\lambda$	wavelength

$\ell$	angular momentum quantum number
$L_H$	distance interaction region - Hex detector
$L_Q$	distance interaction region - Quad detector
$m$	magnetic quantum number
$\mathbf{p}$	electron momentum
$\varphi$	polar angle in radial coordinates
$\varphi^{cc}$	continuum-continuum phase
$\varphi_{CEP}$	carrier-envelope phase
$\varphi^W$	Wigner phase
$\varphi^{XUV}$	XUV spectral phase
$U_p$	ponderomotive energy
$\psi$	wave function
$p_x$	electron momentum in x-direction
$p_y$	electron momentum in y-direction
$p_z$	electron momentum in z-direction
$q$	charge
$\tau$	pump-probe delay
$\tau_W$	Wigner time delay
$T_c$	cyclotron period
$\vartheta$	azimuthal angle in radial coordinates
$t_{TOF}$	time-of-flight
$V$	potential
$\omega$	angular frequency
$\omega_{IR}$	IR angular frequency

---

## Acronyms

AIS	active interferometer stabilization
Al	aluminum
AOM	acousto-optic modulator
APT	attosecond pulse train
Ar	argon
BS	beam splitter
CEO	carrier-envelope offset
CEP	carrier-envelope phase
COLTRIMS	cold target recoil ion momentum spectrometer
CPA	chirped pulse amplifier
cw	continuous wave
EWP	electron wave packet
EWS	Eisenbud-Wigner-Smith
FEL	Free-electron laser
FWHM	full width at half maximum
GD	group delay
GDD	group delay dispersion
H	hydrogen
He	helium
HH	high harmonic
HHG	high harmonic generation
IR	infrared
KLM	Kerr-lens mode-locking
MB	mainband
MCP	micro channel plate
Ne	neon
OC	output coupler
PD	photo diode
PES	photoelectron spectrum
PPLN	periodically poled lithium niobate

RABBITT	reconstruction of attosecond beating by interference of two-photon transitions
SAE	single-active-electron
SAP	single attosecond pulse
SB	sideband
SE	Schrödinger equation
SPM	self-phase modulation
TDSE	time-dependent Schrödinger equation
Ti-sapph	titanium-doped sapphire
TOF	time-of-flight
UV	ultra-violet
WKB	Wentzel-Kramer-Brillouin
Xe	xenon
XUV	extreme ultra-violet

## Publications

Within the scope of this thesis, the following journal papers and conference contributions were published. The original manuscripts of the journal publications are re-printed with permission in this thesis. The text and figures are printed as published, while the formatting has been adapted to fit the page format of this thesis. Further, the numbering of the figures, tables, references and equations has been adjusted. The reference list of the publication has been included in the reference list at the end of this thesis. The copyright of the publications is held by the respective copyright holders.

### Journal papers

1. **Jaco Fuchs**, Nicolas Douguet, Stefan Donsa, Fernando Martin, Joachim Burgdörfer, Luca Argenti, Laura Cattaneo and Ursula Keller, «Time delays from one-photon transitions in the continuum», *Optica* 7(2), 154-161 (2020), [doi.org/10.1364/optica.378639](https://doi.org/10.1364/optica.378639)
2. Constantin Krüger,\* **Jaco Fuchs**,\* Laura Cattaneo, and Ursula Keller, «Attosecond resolution from free running interferometric measurements», *Optics express* 28(9), 12862-12871 (2020), [doi.org/10.1364/OE.391791](https://doi.org/10.1364/OE.391791), (editors pick)

3. **Jaco Fuchs**, Nicolas Douguet, Stefan Donsa, Fernando Martin, Joachim Burgdörfer, Luca Argenti, Laura Cattaneo and Ursula Keller, «Towards the complete phase profiling of attosecond wave packets», ArXiv:2012.07426, <http://arxiv.org/abs/2012.07426>

## Conference papers

1. Johanna Vos, Laura Cattaneo, Luca Pedrelli, **Jaco Fuchs** and Ursula Keller, «Dynamical decay of a Shape Resonance in N<sub>2</sub>O», *Molecular Ultrafast Science and Technology (MUST) Annual Meeting (7th)*, Grindelwald, Switzerland (2017). (Poster).
2. **Jaco Fuchs**, Nicolas Douguet, Stefan Donsa, Fernando Martin, Joachim Burgdörfer, Luca Argenti, Laura Cattaneo and Ursula Keller, «Time delays from one-photon transitions in the continuum», *7th International Conference on Attosecond Science and Technology (ATTO2019)*, Szeged, Hungary (2019). (Talk).
3. **Jaco Fuchs**, Nicolas Douguet, Stefan Donsa, Fernando Martin, Joachim Burgdörfer, Luca Argenti, Laura Cattaneo and Ursula Keller, «Time delays from one-photon transitions in the continuum», *Ultrafast Science and Technology Spain 2019 (USTS meeting 2019)*, Madrid, Spain (2019). (Poster).
4. **Jaco Fuchs**, Nicolas Douguet, Stefan Donsa, Fernando Martin, Joachim Burgdörfer, Luca Argenti, Laura Cattaneo and Ursula Keller, «Time delays from one-photon transitions in the continuum», *Conference on Lasers and Electro-Optics (CLEO)*, San Jose, USA (2020), (Talk, Maiman student paper award).
5. Luca Argenti, **Jaco Fuchs**, Nicolas Douguet, Stefan Donsa, Fernando Martin, Joachim Burgdörfer, Laura Cattaneo and Ursula Keller, «Time delays from one-photon transitions in the continuum», *APS*



*division of Atomic, Molecular and Optical Physics (DAMOP meeting), virtual (2020). (Talk).*

6. **Jaco Fuchs**, Nicolas Douguet, Stefan Donsa, Fernando Martin, Joachim Burgdörfer, Luca Argenti, Laura Cattaneo and Ursula Keller,  
«Time delays from one-photon transitions in the continuum», *Ultrafast Phenomena 2020*, Shanghai, China (2020). (Talk, given by L.A.).
7. **Jaco Fuchs**, Constantin Krüger, Laura Cattaneo and Ursula Keller,  
«Attosecond resolution from free running interferometric measurements», *Ultrafast Phenomena 2020*, Shanghai, China (2020). (Talk).
8. **Jaco Fuchs**, Nicolas Douguet, Stefan Donsa, Fernando Martin, Joachim Burgdörfer, Luca Argenti, Laura Cattaneo and Ursula Keller,  
«High-order phase profiling of attosecond wave packets», *Ultrafast Phenomena 2020*, Shanghai, China (2020). (Poster).



# Abstract

Attosecond science investigates physical phenomena on the attosecond timescale. On this timescale, exclusively optical pulses enable the required temporal resolution. However, state-of-the-art attosecond light sources are too weak to enable pure attosecond pump - attosecond probe measurements. One of the major challenges of attosecond science is, therefore, the development of alternative techniques to achieve attosecond resolution.

In this thesis, novel interferometry schemes for the measurement of attosecond dynamics are presented. These schemes are based on the quantum path interference in attosecond XUV pump - femtosecond IR probe experiments. The well-established Reconstruction of Attosecond Beating by Interference of Two-photon Transitions (RABBITT) technique is developed further and new fundamental physics discoveries are made.

First, an experimental procedure is presented, which allows for the quantification of time delays in the photoionization process arising from single-photon transitions in the electronic continuum. The found delays demonstrate an angular momentum contribution to the photoionization time delay. Together with numerical simulations and analytic estimates, the experimental values suggest a universal character across different chemical species.

Second, a RABBITT-type experiment employing spectrally broad, overlapping high harmonics is presented. The broad harmonics lead to a quantum beating between one-photon and two-photon transitions, which reveals additional phase information about the underlying attosecond pulse train. Periodic oscillations of the spectral phase of an attosecond pulse train are found, demonstrating that each harmonic is individually chirped.

Finally, an analysis procedure of RABBITT-type experiments is presented, which demonstrates that an attosecond delay control is not required to achieve attosecond resolution. This technique relaxes the experimental demands of attosecond interferometric measurements and moreover enables attosecond measurements at Free-electron lasers, where a femtosecond timing jitter is present.

For the experiments presented in this thesis, a COLTRIMS detector is used. In contrast to existing attosecond interferometry methods, the here presented methods involve not only the phase but also the amplitude and modulation depth of the resolved oscillations in the time-dependent photoelectron spectra, to infer information about the underlying attosecond dynamics. The coincidence detection capability of the detector of the COLTRIMS detector supports this approach.

## Kurzfassung (German)

Das Ziel der Attosekunden-Physik ist die Untersuchung von Naturphänomenen auf einer Attosekunden-Zeitskala. Ausschliesslich optische Lichtpulse ermöglichen die dafür erforderliche zeitliche Auflösung. Selbst hochmoderne Attosekunden-Lichtquellen sind allerdings nicht ausreichend stark, um reine Attosekunden-Pump-Probe-Messungen durchzuführen. Eine der grössten Herausforderungen in der Attosekunden-Physik ist daher die Entwicklung alternativer Messmethoden, welche dennoch eine attosekundengenaue Auflösung ermöglichen.

In dieser Dissertation werden neue Interferometrie-Methoden zur Messung von Attosekunden-Dynamiken vorgestellt. Die vorgestellten Methoden basieren auf der Quantenpfad-Interferenz in kombinierten Attosekunden-XUV-Pump-Femtosekunden-IR-Probe-Messungen. Dabei werden die bereits etablierte RABBITT-Methode (Reconstruction of Attosecond Beating By Interference of Two-photon Transitions) weiterentwickelt und neue physikalische Entdeckungen präsentiert.

Als Erstes wird eine experimentelle Methode zur Messung von Attosekunden Zeitverzögerungen im Photoionisationsprozess eingeführt, welche durch die Interaktion mit einzelnen Photonen verursacht werden. Die gefundenen Zeitverzögerungen weisen einen Beitrag auf, welcher durch den Drehimpuls der emittierten Elektronen bestimmt wird. In Verbindung mit numerischen Simulationen und einer analytischen Abschätzung zeigen die experimentellen Messungen, dass dieser Beitrag universell für die

Elektronen-Emission in unterschiedlichen chemischen Elementen ist.

Als Zweites wird ein der RABBITT-Technik ähnliches Experiment mit spektral überlappenden, höheren Harmonischen präsentiert. Die spektral verbreiterten Harmonischen führen zu einer Quantenpfad-Interferenz von 1-Photonen- und 2-Photonen-Übergängen, welche zusätzliche Phasen-Informationen über den zugrunde liegenden Attosekunden-Pulszug enthüllt. Dabei werden periodische Oszillationen in der spektralen Phase der Attosekunden-Pulszüge entdeckt, welche einen individuellen Chirp der einzelnen Harmonischen implizieren.

Zum Schluss wird eine Technik zur Auswertung von RABBITT-Messungen vorgestellt, welche aufzeigt, dass prinzipiell weder Attosekunden-Pulse noch Attosekunden-Scans notwendig sind, um eine Attosekundengenauigkeit zu erreichen. Diese Technik vereinfacht zukünftige RABBITT-Experimente und ermöglicht Attosekunden-Messungen an Freie-Elektronen-Lasern, welche einer Femtosekunden-Zeitinstabilität unterliegen.

Für die Experimente, welche in dieser Arbeit vorgestellt werden, wurde ein COLTRIMS-Detektor benutzt. Im Gegensatz zu herkömmlichen Attosekunden-Interferometrie-Methoden werden in den hier vorgestellten Methoden nicht nur die Phase, sondern auch die Amplitude und Modulationstiefe der gemessenen Oszillationen in den zeitabhängigen Photoelektronen-Spektren ausgenutzt, um Informationen über die Attosekunden Dynamik zu erhalten. Die Koinzidenz-Detektions-Möglichkeit des COLTRIMS-Detektors trägt maßgeblich zu diesem Ansatz bei.

## Chapter 1

---

# Introduction

*How can one measure time?* - In everyday life, a "stopwatch" method enables a convenient and suitable timing method. When starting a process, say a 100 m-sprint, a stopwatch is started, and at the finish the time is read out. For many important scientific questions the stopwatch method is, however, not suitable: How old is the human race? How old is the earth? Or even: How old is the universe? And on the shorter timescale: How long does a virus need to enter a cell? How long do chemical reactions take? How long does it take for an electron to leave an atom? To answer these questions, other timing techniques are required.

The stopwatch method has two fundamental limitations. First, one needs to wait for the entire duration of the process. This sets an upper limit for the measurable time, e.g., one cannot wait for the full 4.5 billion years of the formation of another earth-like planet. For longer timescales, indirect methods have to be used, such as the radiocarbon method for dating the age of fossils or the extrapolation of the Hubble-constant for estimating the age of the universe. However, for such indirect methods, preliminary knowledge is required.

Second, on the shorter timescales, the stopwatch method is limited by detector times. Naturally, one cannot measure shorter times than it takes to monitor the process. Let's consider a high-speed microscope that tries to observe a virus entering a cell. The camera acquires a single picture in a few milliseconds, but the virus may enter the cell during a few microsec-

onds. The resulting high-speed movie would not reveal any information about the actual penetration. One may give a lower boundary for the stop-watch method of a few picoseconds ( $1 \text{ ps} = 10^{-12} \text{ s}$ ), corresponding to the fastest transistor switching times.

Besides indirect methods, stroboscopic measurements can be employed. Let's consider again the virus entering the cell. If one synchronizes a short flash with the virus docking into the cell, the camera is exposed only for the duration of the flash, in an otherwise dark surrounding. Then, even if the acquisition time of a single picture is much longer than the entire process, only the short period of the flash is imaged. By repeating the experiment with different timings of the flash, the resulting series of pictures can be combined to a movie, with a better temporal resolution than the actual camera acquisition time. The only limitations are the synchronization of the flash, the flash duration, and, of course, repeatability of the process.

Optical pump-probe measurements follow this principle. A "pump" laser pulse initiates a process and a delayed "probe" laser pulse tests the process. The usage of laser pulses proved to be very successful since extremely short pulse durations can be achieved, orders of magnitude shorter than, e.g., electrical signals. Only three decades after the first laser in 1960 [1], laser pulses of a few femtoseconds ( $1 \text{ fs} = 10^{-15} \text{ s}$ ) became available in the visible/infrared (IR) regime[2]. Then, with the turn of the millennium attosecond pulses ( $1 \text{ as} = 10^{-18} \text{ s}$ ) were demonstrated [3, 4]. A few years later, attosecond photoionization time delays were measured in a pump-probe experiment [5, 6].

In principle, also for the short timescales, indirect timing methods are available. In the attoclock method, the emission angle of photoelectrons in a few-cycle elliptically polarized laser field is used to infer information about attosecond tunneling times[7]. In the LIGO experiment, length changes of the interferometer arms in a Michelson interferometer are detected, essentially corresponding to a delay of the laser light  $< 10^{-27} \text{ s}$ . However, indirect methods cannot probe different instants of time.



---

*Why attosecond science?* - Within one attosecond light travels  $3 \cdot 10^{-10}$  m, i.e., about the size of a small atom. Being restricted by the speed of light, generally, no physical information can travel farther in this time. Consequently, no observable effect at all can be expected on this timescale on a macroscopic level, and, in principle, not even on a molecular level. Naively, one may ask: Why is the attosecond timescale relevant? For typical electron binding energies, the associated oscillation period of the quantum mechanical wave function,  $\tau = \hbar/E$ , lies exactly on this timescale (e.g., the atomic unit of time, defined as  $\tau_a = \hbar/E_H$ , is 24 as). In turn, the quantum mechanical interference, which ultimately leads to relevant macroscopic effects, is determined on this timescale. For example, the interference of different wave functions and partial waves may influence the emission angle of a photoelectron, determine the outcome of a chemical reaction, or even increase or decrease the efficiency of a solar cell.

In the past two decades, attosecond science contributed to our understanding of electron dynamics in various types of systems ranging from single atoms [6] and molecules [8] to liquids [9], dielectrics [10], semiconductors [11] metals [5], nanostructures [12], and certainly more. The common ground of the field is the spectroscopic, methodological knowledge rather than specific knowledge about the investigated materials. Furthermore, attosecond science drives the development of cutting-edge laser and detector technologies.

Due to the required spectral bandwidth, attosecond pulses have a center wavelength that lies in the extreme ultraviolet (XUV) spectral range or at even shorter wavelengths. Measuring with attosecond pulses, hence, comes with several technical challenges. The major challenge, however, is that state-of-the-art attosecond XUV light sources are not bright enough to carry out attosecond pump - attosecond probe experiments. Intriguing and innovative pump-probe schemes using a combination of attosecond XUV pump and femtosecond IR probe have to be developed to enable attosecond resolution. Ultimately, it is exactly the above-described quantum interference that allows for attosecond measurements.

*What is this thesis about?* - In this thesis novel XUV-IR interferometric measurement schemes are developed and the thereby found, fundamental physics discoveries are presented. The developed interferometry schemes are based on the quantum path interference in two-color attosecond photoionization experiments. They build on the well-established Reconstruction of Attosecond Beating By Interference of Two-photon Transition (RABBITT) technique [4, 13] and try to advance it in different facets. Therefore, the research findings presented in this thesis shall not only expand the knowledge horizon at the time of writing but, moreover, contribute to the field of attosecond science on a long-term basis.

Chapter 2 introduces the field of attosecond science, with a particular focus on attosecond photoionization spectroscopy and the RABBITT technique. The generation of attosecond pulse trains via HHG and the retrieval of photoionization time delays via the RABBITT technique is detailed. Relevant other attosecond spectroscopies are mentioned.

Chapter 3 describes the experimental setup, which has been used throughout the research work for this thesis. The commercial laser system for the generation of intense femtosecond laser pulses and the subsequent attosecond XUV-IR pump-probe delay line is presented. Further, the coincidence detection of photoelectrons and ions with the COLTRIMS detector is described. Details on the experimental acquisition are given.

Chapter 4 presents an angle-resolved RABBITT measurement, which enables the quantification of time delays arising from one-photon transitions in the electronic continuum. To this end, a simultaneous fitting method of the anisotropy parameters of the time dependent electron angular distribution in helium is developed. The found delays suggest a universal character across different chemical species. Analytical estimates of the delays are presented. Finally, the method is employed to larger atoms.

Chapter 5 presents the results of a two-color interferometry scheme employing spectrally overlapping high harmonics. The induced quantum beating between one-photon and two-photon transitions enables the retrieval of detailed phase information about an attosecond pulse train, complementary to the RABBITT technique. The additional phase information

---

enables the observation of periodic spectral phase oscillations due to the femtochirp in an attosecond pulse train, which are inherently inaccessible in the conventional RABBITT technique. An analytic model of attosecond pulse trains and an approach towards the reconstruction of absolute phases is presented.

Chapter 6 demonstrates a novel analysis technique of conventional RABBITT experiments which allows for the retrieval of attosecond delays from free-running quantum interferometers. The presented analysis procedure facilitates the measurement of attosecond photoionization time delays in table-top experiments and enables the measurement of attosecond delays at large scale facilities, where a femtosecond timing jitter is present.

Chapter 7 presents the results of a conventional RABBITT experiment in helium in the regime just above threshold. This regime enables a monitoring of the ultrafast excited state dynamics and the investigation of resonant two-photon ionization transitions via the excited states. Photoionization time delays, induced by the excited states resonances, as well as the ultrafast Stark-shift are analyzed. The last chapter concludes.



# Attosecond photoionization spectroscopy

Attosecond science is an emerging experimental research area that, by definition, aims to answer scientific questions on an attosecond timescale. As such, it addresses various types of physical and chemical phenomena, deals with a wide range of materials, and covers investigations in all states of matter. Being unrestricted in *what* is studied, the common ground of the field is rather *how* things are studied.

Precise physical triggers in the form of attosecond light pulses are required to probe dynamics on the attosecond timescale. The generation and characterization of attosecond light pulses thereby comprise a major part of the research area. Section 2.1 provides a qualitative, high-level introduction on the generation of attosecond light pulses via high harmonic generation (HHG).

Due to the required spectral bandwidth, attosecond pulses necessarily have a center frequency in the XUV (or even higher energetic) spectral range. Thus, commonly used pulse characterization methods for optical pulse are not applicable. Instead, due to their higher energetic frequency components, attosecond pulses can photoionize typical valence electrons, such that time-resolved photoelectron spectroscopy can be used to reveal phase information about the ionizing light pulses. Attosecond photoionization spectroscopy, therefore, comprises both state-of-the-art pulse characterization methods as well as precise timing tools for the study of one of the most fundamental physical processes, Einsteins' photoelectric ef-

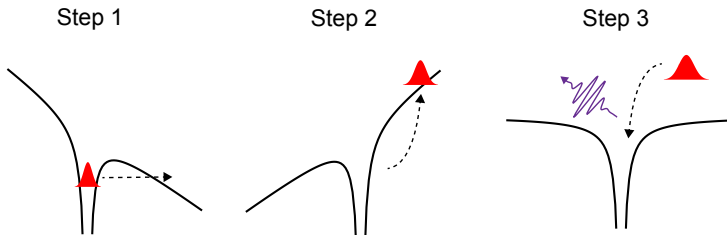


**Figure 2.1:** Simple-man-model (three-step model) : Step 1: An electron tunnels through the binding Coulomb potential, which is bend by a strong laser field. Step 2: In the following laser half cycle the liberated electron wave packet acquires kinetic energy and is accelerated back towards the parental ion. Step 3: The electron radiatively recombines with the parental ion, emitting a high energetic photon.

fect. Section 2.2 provides an introduction to the RABBITT technique for the characterization of attosecond XUV pulses and the measurement of attosecond photoionization time delays. The understanding of RABBITT is a prerequisite for the understanding of the subsequent chapters.

## 2.1 Attosecond pulse generation

For more than 15 years, attosecond pulses could exclusively be generated via the so-called high harmonic generation (HHG) process [14–16]. Applicable in table-top-experiments, the method has been successfully established in many research laboratories worldwide. Only recently (2020), attosecond light pulses generated by Free-electron lasers have been demonstrated [17]. However, the achieved pulse durations are still crucially longer than from table-top experiments based on HHG.

### 2.1.1 High harmonic generation

High harmonic generation (HHG) describes the generation of high-order harmonics (HH) of a fundamental laser field. It can be intuitively understood in a semi-classical picture known as the three-step model (also simple man’s model) [15], illustrated in Figure 2.1. When an atom or molecule is exposed to a strong optical laser field, its binding potential is dressed by the electric field such that bound electrons can tunnel through the resulting potential barrier, effectively releasing a well-localized electron wave

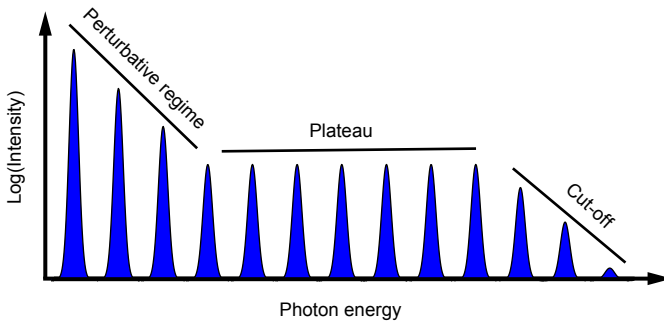


**Figure 2.2:** High harmonic spectrum. High order harmonics are generated at odd multiples of the fundamental laser frequency. After a drop of the harmonic yield in the perturbative regime, the harmonic yield stays constant in the plateau region, extending over a larger energy range. The yield drops again at the cut-off energy, which depends on the ponderomotive energy  $U_p$  and the ionization potential  $I_p$  of the gas target.

packet in the electronic continuum nearby the ion. This tunnel-ionization is referred to as the first step. When the electric field is reversed in the next laser field half-cycle, the electron wave packet is accelerated back towards its parental ion and gains kinetic energy. This acceleration is referred to as the second step. Finally, when the electron wave packet hits the parental ion, three processes may occur: i) The electron scatters elastically. ii) The electron scatters inelastically, ionizing further electrons or exciting the ion. iii) The electron radiatively recombines with the ion, emitting a high energetic photon. This last process, i.e., the radiative recombination, completes the three-step-model. Intuitively, as the recombination occurs during a small fraction of the optical laser field, the emitted radiation burst can be expected to have a much shorter pulse duration than one half-cycle, effectively suggesting attosecond light pulses.

The three-step model also allows for quantitative considerations. After tunnel-ionization, the electrons can be treated classically as point charge for which Newton's equation of motion can be solved (with or without Coulomb potential). The analysis of the return time and return energy of the liberated electrons reveals two prominent characteristics of the high harmonic generation.

First, there is a maximal return energy, which depends on the intensity  $I$  and angular frequency  $\omega_0$  of the fundamental, driving laser field. Hence, there is also a maximal energy for the emitted photons, which is given by

$$E_{\text{cut-off}} = I_p + 3.17U_p, \quad (2.1)$$

where  $I_p$  is the ionization potential of the target gas and

$$U_p = \frac{2e^2}{c\epsilon_0 m_e} \frac{I}{4\omega_0^2} \quad (2.2)$$

is the ponderomotive potential. The retrieved harmonic yield can be distinguished in three regimes, illustrated in Figure 2.2. For low harmonics (e.g. 3rd harmonic, 5th harmonic) a perturbative picture is applicable to describe the harmonic yield. Here, the generation efficiency decreases significantly with higher orders. Next, for higher-order harmonics until the cut-off energy  $E_{\text{cut-off}}$  the simple-man picture is applicable. In this highly non-linear regime, the efficiency only weakly depends on the harmonic order. Therefore, it is referred to as plateau region. For higher energies than  $E_{\text{cut-off}}$ , the efficiency finally drops to zero.

Second, the dependence of the return energy on the return time leads to different photon energies being emitted at slightly different times, implying a so-called attochirp [18]. In principle, for each return energy (except for the cut-off) two possible trajectories with different return times exist. These short and long trajectories lead to opposite signs of the chirp. Most HHG driven experiments are optimized for short trajectories, where the attochirp is positive.

In principle, the three-step model can also be treated fully quantum mechanical [16]. Historically, high harmonics and the plateau region have been observed experimentally for the first time by McPherson and coworkers in 1987 [14]. The explanation via the three-step model followed 6 years later by P. B. Corkum [15]. The experimental proof of attosecond bursts finally followed in 2001 by Paul et al. [4].

### Phase matching

The above section discusses the microscopic response of a single atom in the HHG. In order to determine the high harmonic yield in physical



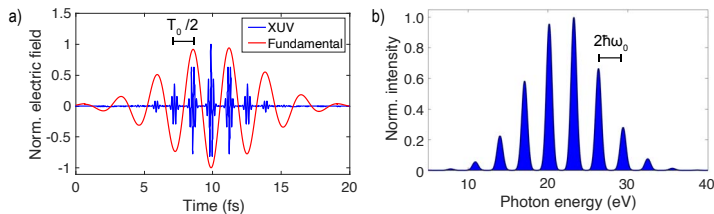


**Figure 2.3:** Attosecond pulse train in the time and frequency domain. a) XUV attosecond pulse train and fundamental, driving laser field in the time domain. An attosecond XUV burst is emitted at each half-cycle of the fundamental laser field. b) XUV spectrum of the APT. The APT consists of odd high harmonics of the fundamental laser frequency. The spectral envelope is determined by phase-matching effects and the cut-off energy.

experiments, the macroscopic response of a collection of atoms has to be considered. Reabsorption and phase matching effects [19, 20] set high technical demands for the geometry of the generating gas target and the employed gas pressure.

### 2.1.2 Attosecond pulse train

The generation of attosecond pulse trains (APTs) via HHG can be inspected both in the time and in the frequency domain, with complementary insights.

In the time domain, using the three-step model, attosecond XUV light bursts are emitted within a fraction of the half-cycle of the driving laser field, repeating every half cycle. This leads to sequence of attosecond bursts with a repetition time of  $t_{rep} = T_0/2$ , or respectively, a repetition frequency of  $f_{rep} = 2f_0$ , see Figure 2.3 a). Here,  $T_0$  and  $f_0$  are the period and the frequency of the fundamental laser field. Generally, for HHG, high field strengths are required, typically provided by tightly focused femtosecond laser pulses in the optical or infrared regime. As only the most intense half-cycles of the few-cycle driving field can efficiently generate high harmonics, the envelope of the attosecond pulse train is slightly shorter than the envelope of the driving field.

In the frequency domain, odd-order harmonics are generated within the overall spectral bandwidth of the APT, see Figure 2.3 b). Even order harmonics are (typically) suppressed for symmetry reasons. Only if a

non-centrosymmetric HHG target gas or a combination of the fundamental and the second harmonic of the driving field is used, even harmonics are generated<sup>1</sup>. The high harmonic spectrum can be considered as a frequency comb consisting of high harmonics  $\text{HH}_{2n+1}$  with frequencies  $f_{2n+1} = (2n + 1)f_0$  where  $n = 1, 2, 3, \dots$ . Then, indeed, the comb spacing  $\Delta f$  corresponds to the burst repetition rate,  $\Delta f = 2f_0 = f_{rep}$ . The overall spectral bandwidth determines the pulse duration of each attosecond burst (and vice versa), and the bandwidth of the individual harmonics determines the duration of the temporal envelope of the APT (and vice versa). A mathematical model, which also allows for an analysis of different types of chirps, is presented in Section 5.3.

### Single attosecond pulses

Single attosecond pulses (SAPs) can also be generated. Compared to the generation of APTs, the radiative recombination has to be confined to a single half-cycle of the driving field. To this end, the fundamental laser field is beforehand compressed to very few cycles. Then, multiple schemes to confine the actual HHG to a single half-cycle are available [21–23]. Alternatively, isolated SAPs can also be selected posterior via amplitude gating [24] or the attosecond lighthouse technique [25].

## 2.2 Attosecond pump-probe experiments

Attosecond pump-probe experiments comprise several time-resolved pump-probe measurement techniques using attosecond pulses. As in most experiments, the high harmonic yield is too low to perform XUV pump - XUV probe measurements, typically attosecond XUV pump - femtosecond IR probe measurements are performed. However, measurement schemes have been developed which still achieve a precision of a few attoseconds. It has to be noted that in some schemes a clear distinction between pump and probe cannot be made. Among others, the most prominent schemes are attosecond transient absorption [26, 27], RABBITT [4, 13] and the attosecond streaking [28].

---

<sup>1</sup>Also for the generation of a second harmonic component, a non-centrosymmetric material is required to break the symmetry

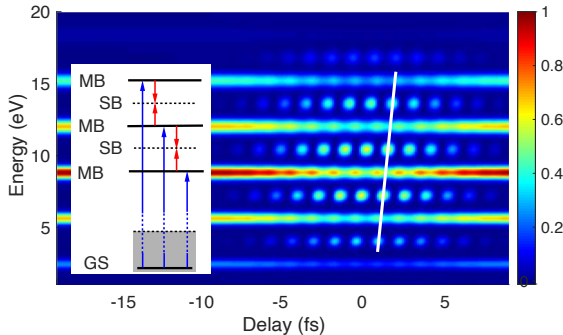


**Figure 2.4:** Typical RABBITT spectrogram. The photoionization yield is shown in a 2-d histogram as a function of energy and time delay between the XUV-APT and IR laser pulse. The inset indicates the energy levels of the MBs and SBs, as well as the contributing quantum pathways. The SB yield follows the envelope overlap of the two light fields and oscillates as a function of the pump-probe delay. The white line indicates a phase offset between the different SBs.

While attosecond transient absorption aims to measure transient changes in the optical density, RABBITT and Streaking are photoionization spectroscopies. RABBITT and Streaking, in principle, target the same physical observables. However, RABBITT relies on the use of APTs while Streaking relies on the use of isolated single attosecond pulses. For the further understanding of this thesis, only the RABBITT scheme is relevant.

### 2.2.1 Reconstruction of attosecond beating by interference of two-photon transitions (RABBITT)

In RABBITT, the spectral phase of a photoelectron wave packet ionized by an XUV-APT is measured. This phase can be related to the spectral phase of the APT.

An XUV-APT is focused together with a time-delayed replica of its generating laser field on the target under investigation. The one-photon ionization by the XUV harmonics leads to replicas of the harmonics in the photoelectron spectrum, so-called Mainbands (MBs). The kinetic energy of these MBs is equal to the photon energy of the corresponding high harmonic minus the ionization potential. In the presence of the IR laser field, the liberated electrons can further undergo continuum-continuum

(cc) transitions, either via additional absorption or stimulated emission of an IR photon. These 2-photon transitions (also called 2-photon quantum pathways) give rise to sidebands (SBs) in the photoelectron spectrum, which lie in between the MBs. Given the absorption of a certain XUV photon, the final kinetic energy of the two accessible SBs are

$$E_{kin} = E_{XUV} - I_p \pm \hbar\omega_0. \quad (2.3)$$

In turn, two quantum pathways contribute to each SB: i) The quantum pathway following the XUV ionization to the lower-lying MB and additional absorption of an IR photon. ii) The quantum pathway following the XUV ionization to the higher lying MB and stimulated emission of an IR photon. As these quantum pathways, which end at the same final kinetic energy, are coherent, they give rise to a quantum path interference, leading to an oscillation of the SB yield as a function of the pump-probe delay. From the phase of this SB oscillation, phase and timing information about the contributing quantum pathways can be inferred. Figure 2.4 shows a simulated RABBITT spectrogram, highlighting the MBs and SBs as well as the different quantum pathways.

In a perturbation theory approach [29] the complex two-photon transition matrix element can be split into a product of the underlying one-photon-transition induced by the XUV and the subsequent cc-transition induced by the IR. The phase of the two-photon matrix element is then given as a sum of the phases of the one-photon and cc-process. In detail, the two-photon quantum pathways comprise a total of four phase terms: i) The XUV harmonic phase  $\varphi^{XUV}$  which is imprinted on the photoelectrons spectral phase, ii) The scattering phase  $\varphi^W$  (also Wigner phase, detailed in the next section) for the one-photon ionization, iii) the cc-phase  $\varphi^{cc}$  induced by the cc-transition and iv) the phase of the IR electric field  $\varphi^{IR} = \omega_0\tau$ , with  $\tau$  being the delay of the IR pulse with respect to the XUV pulse (positive delays refer to IR pulses coming after the XUV pulse). The complex amplitudes of the quantum pathways contributing to a SB of order  $2n$  can thus be written as

$$A^{(+)}(\tau) = |A^{(+)}| e^{i(\varphi_{2n-1}^{XUV} + \varphi_{2n-1}^W + \varphi_{2n-1}^{cc+} + \omega_0\tau)} \quad (2.4)$$

and

$$A^{(-)}(\tau) = |A^{(-)}| e^{i(\varphi_{2n+1}^{XUV} + \varphi_{2n+1}^W + \varphi_{2n+1}^{cc-} - \omega_0\tau)}, \quad (2.5)$$

for the quantum pathways including the further absorption (+) or stimulated emission (−) of an IR photon. Note the negative sign of  $\omega_0\tau$  in the emission case. The lower index  $2n \pm 1$  on the XUV phase indicates the phase of harmonic  $2n \pm 1$ . Similarly, for the Wigner and cc-phase, the index indicates the corresponding MB kinetic energies. The total time dependent ionization yield of the SB then gives

$$\begin{aligned}
 I_{SB}(\tau) &= |A^{(+)}(\tau) + A^{(-)}(\tau)|^2 \\
 &= |A^{(+)}|^2 + |A^{(-)}|^2 + [A^{(+)}(\tau)A^{(-)*}(\tau) + c.c.] \\
 &= |A^{(+)}|^2 + |A^{(-)}|^2 \\
 &\quad + |A^{(+)}||A^{(-)}| (e^{i(2\omega_0\tau - \Delta\varphi_{2n}^{XUV} - \Delta\varphi_{2n}^W - \Delta\varphi_{2n}^{cc})} + c.c.) \\
 &= |A^{(+)}|^2 + |A^{(-)}|^2 \\
 &\quad + 2|A^{(+)}||A^{(-)}| \cos(2\omega_0\tau - \Delta\varphi_{2n}^{XUV} - \Delta\varphi_{2n}^W - \Delta\varphi_{2n}^{cc}).
 \end{aligned} \tag{2.6}$$

Here  $\Delta\varphi_{2n}^{XUV} = \varphi_{2n+1}^{XUV} - \varphi_{2n-1}^{XUV}$ ,  $\Delta\varphi_{2n}^W = \varphi_{2n+1}^W - \varphi_{2n-1}^W$  and  $\Delta\varphi_{2n}^{cc} = \varphi_{2n+1}^{cc,-} - \varphi_{2n-1}^{cc,+}$  correspond to the XUV, Wigner and cc-phase differences of the two quantum pathways. The sign of the phase differences in Equation (2.6) may vary for different literature works since it depends on the definition of the delay axis direction. The total SB phase offset  $\varphi_{SB2n} = \Delta\varphi_{2n}^{XUV} + \Delta\varphi_{2n}^W + \Delta\varphi_{2n}^{cc}$  can then be fitted from the experimental RABBITT spectrogram or alternatively retrieved Fourier Transform. The retrieved phase offsets of different SBs can be used either to determine the attochirp [4, 13, 18] or to isolate so called photoionization time delays [6, 30]. It has to be noted that, in principle, an additional arbitrary phase offset which corresponds to the unknown time zero of the delay axis in the experiment, adds up to each SB phase. However, when taking phase differences between different SBs this phase offset cancels out.

### Determination of the attochirp

In order to determine the chirp of the XUV pulse (attochirp) from the retrieved SB phases in RABBITT, either theoretical values for the Wigner and cc-phase terms have to be used or, particularly for high kinetic energies, they can simply be neglected. The phase difference between different SB

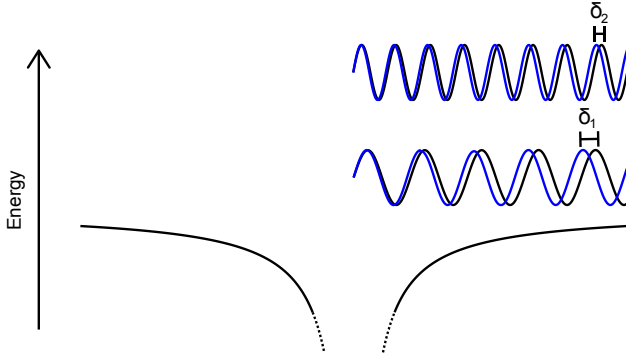


**Figure 2.5:** Wigner scattering phase. Two electron partial waves which propagate across the underlying ionic potential (blue) are compared to free-electron waves (black). Depending on the kinetic energy, they acquire a certain scattering phase, i.e., the Wigner phase. The group delay of an electron wave packet associated with the Wigner phase is called the Wigner time delay.

orders then directly reveals the attochirp [18]

$$\begin{aligned}
 c_{XUV} &= \frac{\varphi_{SB2n+2} - \varphi_{SB2n}}{(2\omega_0)^2} \\
 &= \frac{\frac{\varphi_{2n+3}^{XUV} - \varphi_{2n+1}^{XUV}}{2\omega_0} - \frac{\varphi_{2n+1}^{XUV} - \varphi_{2n-1}^{XUV}}{2\omega_0}}{2\omega_0} \\
 &\approx \frac{\varphi_{2n+2}^{XUV'} - \varphi_{2n}^{XUV'}}{2\omega_0} \\
 &\approx \varphi_{2n+1}^{XUV''},
 \end{aligned} \tag{2.7}$$

where  $\varphi^{XUV'}$  and  $\varphi^{XUV''}$  are the first and, respectively, second derivative of the XUV spectral phase with respect to frequency.

### 2.2.2 Photoionization time delays

Photoionization time delays describe the group delay of the released photoelectron wave packet after photoionization. A localized photoelectron wave packet is composed of partial waves with different kinetic energies, which experience a different scattering phase when escaping the residual ionic potential. Figure 2.5 illustrates this scattering phase compared to a free electron wave of the same energy. Quantum mechanically, due to the underlying Coulomb potential, the electron has higher kinetic energy

compared to the free electron wave such that it acquires a larger phase. In turn, this Wigner phase probes the underlying potential energy landscape of the ion immediately upon photoionization. It can also be considered as a half-scattering phase of the full ionic potential. The derivative of the Wigner phase, i.e., the group delay, is referred to as Wigner time delay (also Eisenbud-Wigner-Smith delay, EWS-delay) [31, 32].

In order to isolate Wigner time delays from a RABBITT measurement, the phase difference between SBs originating from different ionization channels or from different target species has to be retrieved. For simplicity, the *cc*-phase is neglected in the following. When taking the phase difference of SBs from two species, S1 and S2, and of the same SB order, the XUV phase cancels out, revealing a photoionization time delay,

$$\begin{aligned} \frac{\varphi_{SB2n}^{S2} - \varphi_{SB2n}^{S1}}{2\omega_0} &= \frac{\Delta\varphi_{2n}^{XUV} + \Delta\varphi_{2n}^{W2} - \Delta\varphi_{2n}^{XUV} - \Delta\varphi_{2n}^{W1}}{2\omega_0} \\ &= \frac{\Delta\varphi_{2n}^{W2}}{2\omega_0} - \frac{\Delta\varphi_{2n}^{W1}}{2\omega_0} = \Delta\tau_{2n}^{S2-S1}. \end{aligned} \quad (2.8)$$

Relative photoionization time delays have been successfully measured between different atomic and molecular species [33–36] or, respectively, different ionization channels [6, 37–39] in the gas phase, in different types of solids [5, 40–42], and only recently (2020) also in liquids [9]. Typically being on the order of a few attoseconds, experimentally measured photoionization time delays also set benchmarks for state-of-the-art time-dependent quantum mechanical simulations.

The *cc*-phase, in contrast, received much less attention. However, it has been shown that, particularly for low kinetic energies ( $< 15$  eV), it can be on the same order of magnitude as the Wigner phase [29]. It is an open question if the *cc*-phase varies with different species. The research presented in Chapter 4 addresses this question.





# Experimental setup

This chapter walks through the experimental setup, which has been used during the research work carried out for this thesis. It is split into three sections: The commercial femtosecond laser system, the attosecond front-end, and the COLTRIMS detector.

Femtosecond laser pulses are generated by a Ti:sapphire laser oscillator and further amplified in a chirped pulse amplifier, detailed in Sections 3.1.1 and 3.1.2. The femtosecond laser pulses are used to generate attosecond pulses in the "attosecond front-end", described in Section 3.2. A replica of the generating laser pulse is focused together with the attosecond XUV pulses into the COLTRIMS detector, where time-resolved photoelectron spectra of the target gas under investigation are recorded, detailed in Section 3.3.

The setup is capable of RABBITT, Streaking, and also strong-field ionization experiments. Here, the focus is put on RABBITT-type experiments. Due to the combination of the attosecond pump-probe delay line and the COLTRIMS detector, the setup is called AttoCOLTRIMS.

### 3.1 Laser system

The commercial laser system comprises a Rainbow<sup>TM</sup> laser oscillator, a Femtopower PRO V CEP chirped pulse amplifier and a hollow-core fiber compression setup.

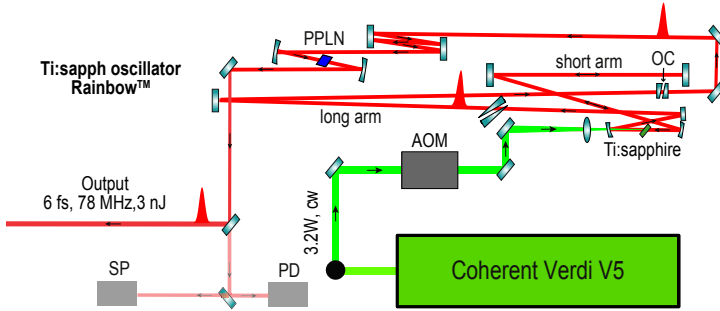


**Figure 3.1:** Rainbow<sup>TM</sup> laser oscillator. The Ti:sapphire laser crystal is pumped with a Coherent Verdi V5 continuous wave laser at 532 nm. The pump power can be controlled via an acousto-optic modulator (AOM). The laser cavity consists of a long and a short arm. After the output coupler (OC) the laser beam is focused into a periodically poled lithium niobate (PPLN) crystal. The oscillator output is monitored on a spectrometer (SP) and a photodiode (PD). Adapted from [43].

### 3.1.1 Rainbow laser oscillator

The Rainbow<sup>TM</sup> oscillator provides few-cycle laser pulses with a pulse energy of 3 nJ and a pulse duration of  $< 6$  fs at FWHM, at a repetition rate of  $f_{rep} = 78$  MHz. The layout of the oscillator is illustrated in Figure 3.1. The oscillator is pumped with a 3.2 W continuous wave laser at 532 nm (Coherent Verdi V5). The laser cavity consists of a long arm and short arm, whereby the titanium-doped sapphire (Ti:Al<sub>2</sub>O<sub>3</sub>) laser crystal [44] is passed twice during each cavity round-trip. The end mirror of the short arm is mounted on a moveable stage, which is used to initiate Kerr-lens modelocking [45]. The end-mirror of the long arm is used as output coupler (OC). In modelocked operation, the optical spectrum covers wavelengths from 600 nm to 1200 nm.

A weak second harmonic replica of the laser pulse is created in a periodically poled lithium niobate (PPLN) crystal for the detection of the carrier-envelope offset (CEO) frequency via  $f$ - $2f$ -interferometry [46]. The CEO frequency is stabilized at  $f_{CEO} = f_{rep}/4$  via an acousto-optic modulator (AOM) which controls the pump power. In the subsequent laser amplifier only multiples of each 4th pulse are amplified, which then leads to pulses with the same carrier-envelope phase (CEP).

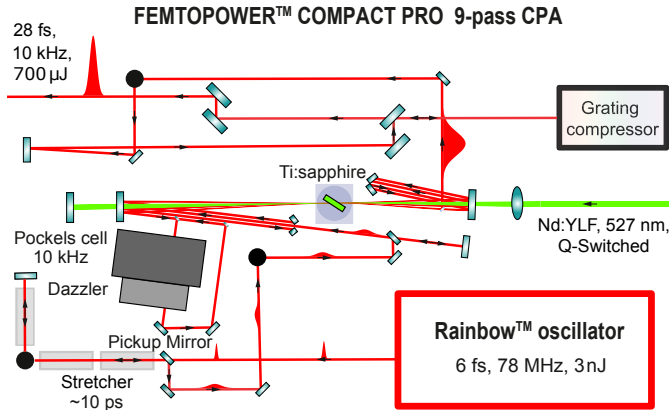


**Figure 3.2:** Femtopower™ Compact PRO V chirped pulse amplifier. The few-cycle laser pulses generated by the Rainbow™ oscillator are stretched by three prism pairs to  $\sim 10$  ps. The pulses are amplified during 4 passages through the Ti:sapph amplifier crystal before being sent into a Pockels cell and a Fastlite Dazzler. After 5 further passages through the amplifier crystal the pulses are recompressed by a grating compressor. The amplifier is pumped by a 527 nm Q-switched Nd:YLF laser (Coherent Evolution). Adapted from [43].

### 3.1.2 Chirped pulse amplifier

In the Femtopower™ Compact PRO V CEP chirped pulse amplifier<sup>1</sup> the few-cycle laser pulses generated by the Rainbow laser oscillator are amplified from 3 nJ to 700 μJ. The repetition rate is reduced to 10 kHz. The layout of the CPA is presented in Figure 3.2.

First, the input pulses are stretched via a prism stretcher to  $\sim 10$  fs. Next, the pulses are amplified during four passages through the Ti:sapphire amplifier crystal before being coupled into a Pockels cell and an acousto-optical programmable dispersive filter (Fastlite Dazzler HR-800). The amplifier crystal is pumped by Q-switched Nd:YLF laser (Coherent Evolution) at 527 nm and  $\sim 60$  W, which is temporally synchronized with the Dazzler and Pockels cell. The Pockels cell reduces the repetition rate to 10 kHz, thereby picking a multiple of each fourth pulse to select for pulses with the same CEP. The Fastlite Dazzler is used to fine-tune and precompensate higher-order dispersion terms in the output pulse. The

<sup>1</sup>G. Mourou and D. Strickland received the Nobel price 2018 for the development of chirped pulse amplification [47], right during the research work carried out for this thesis.

pulses are amplified at the reduced repetition rate during five further passages through the amplifier crystal before being recompressed by a grating compressor. The transform-limited output pulses have a pulse duration of 28 fs at FWHM and a center wavelength of 790 nm.

#### **Fiber compression**

The amplified 28 fs laser pulses can be optionally compressed in a hollow-core fiber compression setup. The pulses are focused into a hollow-core fiber with a length of 1 m and a diameter of 250  $\mu\text{m}$ . The fiber can be filled with up to 2.5 bar of neon gas, leading to a spectral broadening of the pulses via self-phase modulation (SPM). The positive chirp induced by the SPM is compensated by a series of chirped mirror pairs, which enables the generation of down to  $\sim 6$  fs pulses at a pulse energy of 400  $\mu\text{J}$ . The fiber compression setup can also be bypassed.

## **3.2 Attosecond front-end**

The attosecond front-end comprises the attosecond pulse generation via HHG and the pump-probe delay line. The layout is illustrated in Figure 3.3.

The femtosecond laser pulses generated by the combined laser amplifier system, described in Section 3.1, are split by a 80:20 beam splitter. The transmitted part (80%), in the following referred to as pump beam, is loosely focused into a 3 mm long argon gas cell with a backing pressure of up to 200 mbar. The gas cell is located in the otherwise high vacuum HHG chamber with  $10^{-3}$  mbar. XUV-APTs with photon energies between 15 eV and 45 eV are generated. The XUV-APTs pass a 300 nm thick aluminum filter, where the residual IR is filtered out. The XUV-APTs are recombined with the IR probe beam via a holey mirror, where the XUV pump beam passes through and the IR probe beam is reflected. The probe beam, corresponding to the reflected 20% of the input beam beforehand passes a delay stage. The delay stage can be coarse-controlled via a micrometer-precision stepper motor and fine-controlled via a piezo crystal. For the experimental acquisition only the piezo-control is used. The probe beam passes a defocusing mirror to match the beam divergence of the pump beam at the

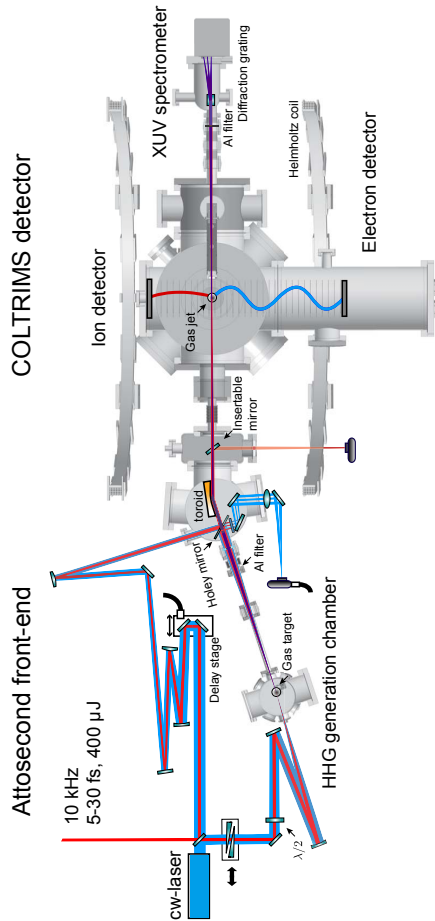


**Figure 3.3:** The femtosecond input laser pulses are split by a 80:20 beam splitter. The transmitted 80% of the beam (pump) is focused into a gas cell with the HHG target gas. The generated XUV-APTs pass through a 300 nm thick aluminium filter where the residual IR is filtered out. It is recombined with the reflected 20% of the beam (probe), which passes a delay stage. The copropagating beams are then focused together into the interaction region of the COLTRIMS detector. The XUV spectrum is monitored. An active interferometric stabilization with a blue narrow linewidth cw-laser is used to stabilize and control the length of the two arms. Adapted from [48].

holey mirror. After recombination, the XUV-pump and IR-probe beams are focused into the interaction region of the COLTRIMS detector by a toroidal mirror. After passing through the detector, the XUV beam is monitored on an XUV spectrometer. The vacuum pressure is  $10^{-6}$  mbar in the recombination chamber and  $10^{-9}$  mbar in the COLTRIMS chamber.

#### **Active-interferometric stabilization**

In order to precisely control the pump-probe delay, i.e., to compensate for vibrations and thermal drifts of the two arms, the delay line is actively stabilized. The output of a blue narrow-linewidth laser (Cobolt Blues 473 nm) is merged with the IR beam on the beam splitter and co-propagates with the IR through both two arms. It is coupled out via the holey-mirror. Here, the pump part of the blue laser is reflected and the probe-part passes through the hole. The resulting interference pattern is monitored on a camera. Analog to a Michelson-type interferometer, the phase of the interference pattern serves as feedback for a PID-control of the delay line [49].

### **3.3 COLTRIMS detector**

In short, the COLTRIMS [50] (COLd Target Recoil Ion Momentum Spectrometer) allows for an angle-resolved detection of photoelectrons and photoions, in coincidence, and with a  $4\pi$ -solid angle detection capability. The energy- and angle-resolved measurement of individual electrons and ions enables a selection of individual reaction channels via a momentum conservation filter.

The combined XUV-pump and IR-probe pulses are focused onto a continuous, supersonic cooled target gas jet, which is perpendicular to the laser beam. Photoelectrons and -ions stemming from the photoionization of the target gas under investigation are created in the small overlap region, which is referred to as interaction region. A constant and homogeneous electric field generated by a series of copper plates around the interaction region sucks the electrons and ions to different sides of the spectrometer. The electric field direction also defines the COLTRIMS spectrometer axis (in the following: *z*-axis). It is perpendicular to both the

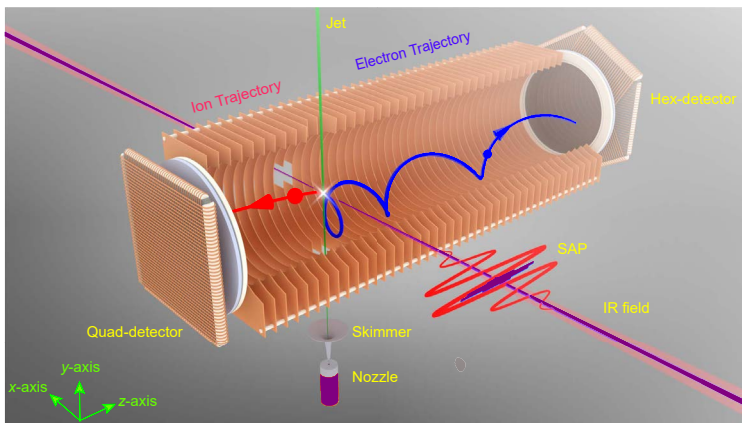


**Figure 3.4:** Schematic view of the COLTRIMS spectrometer. The laser beam direction, the supersonic gas jet, and the COLTRIMS spectrometer axis are orthogonal to each other. Atoms or molecules are ionized in the small interaction region in the center of the spectrometer. A constant electric field generated by 77 equidistant copper plates sucks the released photoelectrons and ions on different sides of the spectrometer. After a certain flight distance the photoelectrons and photoions are detected on a stack of MCP position sensitive delay line anodes. Taken from [43].

supersonic jet and the laser beam. Depending on their initial momentum, the particles follow different trajectories through the spectrometer. Figure 3.4 illustrates the geometry of the COLTRIMS. An additional constant magnetic field, which is generated by a pair of Helmholtz coils<sup>2</sup> and is parallel to the electric field, confines the particles on helical trajectories around the spectrometer axis. After a certain flight distance the charged particles are detected on a stack of micro-channel plates (MCPs) and position sensitive delay line anodes, where the time-of-flight and the impact position of the particles are detected.

In detail, a high voltage is applied across the MCPs, which leads to the release of an electron avalanche when hit by the accelerated photoelectrons, or respectively ions. The corresponding voltage drop of the MCP is used for the time-of-flight detection. The electron avalanche is accelerated onto a mesh of copper double wire, which is the anode. The signal of the induced image charge in the double wire travels along the wire until it reaches the anode holder. From the signal arrival times and the

<sup>2</sup>The earth magnetic field is compensated by additional two sets of Helmholtz coils.

known signal speed, the spatial position of the particle impact is determined. The delay line of the ion detector is composed of two orthogonal layers of anode wire, referred to as Quad-anode. The delay line for the electron detector is composed of three layers of anode wire in a hexagonal configuration, referred to as Hex-anode.

The initial 3-dimensional momenta of both photoelectrons and ions can then be reconstructed from the time-of-flight and impact position of the particles on the detectors. For an ideal acquisition, one electron and one ion are created per laser shot. In the case of multi-particle detection, e.g., when two electrons hit the electron detector, different combinations of x- and y- positions and time-of-flight times are possible, which may lead to false reconstructions. The count rates are adjusted by the gas jet density and the XUV flux, accordingly. For the acquisition and the reconstruction of the particle impact positions from the signal arrival times, the customer adapted software CoboldPC 2011 GmbH is used.

### 3.3.1 Momenta reconstruction

In order to reconstruct the initial momenta of the particles after photoionization, their trajectories have to be analyzed. The Lorentz force acting on a charged particle is

$$\vec{F}_L = q\vec{E} + q\vec{v} \times \vec{B}, \quad (3.1)$$

where  $\vec{E} = [0, 0, E]$  and  $\vec{B} = [0, 0, B]$  are the electric and magnetic field vector which only have a contribution in z-direction,  $q$  is the charge and  $\vec{v}$  is the velocity of the particle. The Newtons equation of motion can then be solved yielding the possible trajectories with

$$x(t) = \frac{1}{Bq} \left[ p_x \sin\left(\frac{Bqt}{m}\right) + p_y \left(1 - \cos\left(\frac{Bqt}{m}\right)\right) \right], \quad (3.2)$$

$$y(t) = \frac{1}{Bq} \left[ p_y \sin\left(\frac{Bqt}{m}\right) - p_x \left(1 - \cos\left(\frac{Bqt}{m}\right)\right) \right], \quad (3.3)$$

$$z(t) = \frac{1}{2} \frac{Eq}{m} t^2 + \frac{p_z}{m} t. \quad (3.4)$$

Here,  $\vec{p} = [p_x, p_y, p_z]$  is the initial 3d-momentum of the particle. The starting point of the trajectory, i.e., the interaction region, is considered to coincide with the origin. While the particles follow circles in the  $xy$ -plane



at the cyclotron period  $T_c = 2\pi m/(Bq)$ , they are constantly accelerated in the z-direction leading to helical trajectories. At the time-of-flight time  $t_{TOF}$  the particles hit the detector at  $x = x(t_{TOF}), y = y(t_{TOF})$  and  $z = L$ , where  $L$  is the length of the electron or ion side of the spectrometer. The linear system of equations (3.2)-(3.4) can then be inverted to retrieve the initial momentum,

$$p_x = -\frac{1}{2}Bq \left( y + \frac{x}{\tan\left(\frac{Bqt_{TOF}}{2m}\right)} \right), \quad (3.5)$$

$$p_y = -\frac{1}{2}Bq \left( x - \frac{y}{\tan\left(\frac{Bqt_{TOF}}{2m}\right)} \right), \quad (3.6)$$

$$p_z = \frac{mL}{t_{TOF}} - \frac{1}{2}Eq t_{TOF}. \quad (3.7)$$

The electric and magnetic field strengths are chosen for each experiment individually to ensure an optimal resolution and detection efficiency in the targeted region of interest. The energy and angular resolution strongly varies with energy and angle. As can be seen in Equations (3.2)-(3.4), particularly for time-of-flight times which equal a multiple of the gyration period, all trajectories end at  $y(t_{TOF}) = x(t_{TOF}) = 0$ . In this case there is no resolution for the transversal momenta  $p_x$  and  $p_y$  at all, leading to nodes in the photoelectron angular distribution. For the experiments presented in this thesis the electric and magnetic field strengths have each been optimized for the highest possible energy resolution on the electron detection, while in parallel assuring that nodes are avoided. The electric field strength was varied between 50 V/m and 450 V/m and the magnetic field strength was varied between 0.6 mT and 1 mT. The length of the electron detector is  $L_H \approx 0.36$  m and the length of the ion detector is  $L_Q \approx 0.11$  m.

In order to filter out electrons stemming from other species than the one under investigation, e.g., due to impurities of the sample gas or background gas in the chamber, an ion time-of-flight filter is applied. The different ion masses lead to well separated ion time-of-flight times for different gas species. In order to avoid false coincidences, i.e., photoelectrons and photoions not stemming from the same photoionization reaction, a

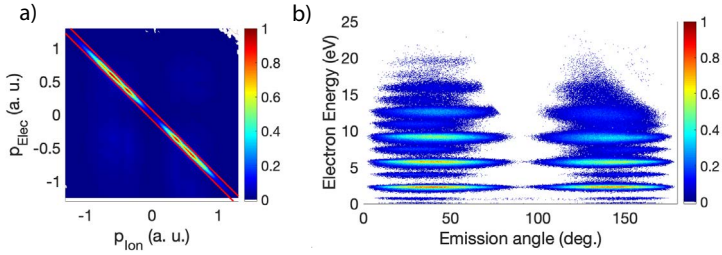


**Figure 3.5:** a)  $p_z$ -momentum correlation of electrons and ions. Due to momentum conservation the electron-ion pairs, which arise from the same atom, follow a diagonal line with negative slope. Events in the bottom left or top right corner correspond to false coincidences. The red lines indicate the acceptance range of a momentum conservation filter. b) Delay integrated photoelectron angular distribution from a RABBITT experiment in helium. MBs and SBs appear as stripes across the electron emission angle  $\alpha$ .

momentum conservation filter is applied. Since the photon momentum as well as the initial momentum of the neutral particle in the gas jet are negligible in the investigated energy range, the momenta of photoelectrons and ions stemming from the same reaction have to satisfy the momentum conservation

$$\vec{p}_e + \vec{p}_{ion} = 0. \quad (3.8)$$

Figure 3.5 a) shows the momentum correlation of captured electron-ion pairs in a photoionization experiment carried out in helium. The acceptance range of a momentum conservation filter, indicated by the red lines, is chosen individually for each experiment as a trade-off between mistakenly discarded counts and unremoved false coincidences.

In the experiments carried out in Chapters 4 and 5 the photoelectron angular distribution is analyzed. In particular, the electron emission angle with respect to the collinear polarization axis of the XUV and IR light fields is determined. Throughout this thesis, the polarisation axis of the employed XUV and IR light fields are both chosen parallel to the spectrometer axis, i.e., the  $z$ -direction. Hence, the electron emission angle with respect to the polarisation axis is given by

$$\alpha = \arctan \left( \frac{\sqrt{p_x^2 + p_y^2}}{p_z} \right). \quad (3.9)$$

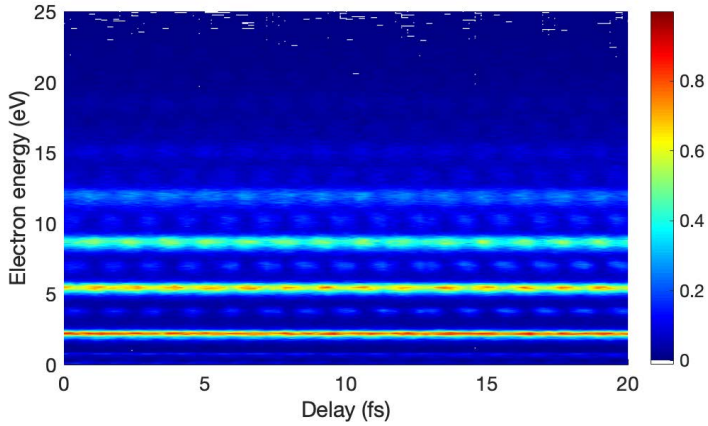


**Figure 3.6:** Experimental RABBITT spectrogram acquired in helium.

Further, the electron kinetic energy is given by

$$E = \frac{1}{2m_e} \sqrt{p_x^2 + p_y^2 + p_z^2}. \quad (3.10)$$

Figure 3.5 b) shows a typical angle-resolved photoelectron energy spectrum for a RABBITT experiment carried out in helium from which later the anisotropy parameter can be calculated. The MBs appear as dominant stripes at the specific MB kinetic energies. The SBs appear as faint stripes in between the MBs. Finally, Figure 3.6 shows a typical experimental RABBITT spectrogram with helium as target gas. Delay steps of 210as are used throughout this thesis. The energy bin size varies for the different experiments, depending on the integration time and the performed analysis.



## Angle-resolved attosecond interferometry

By virtue of its experimental simplicity, the RABBITT technique established itself as the most frequently used method in attosecond photoionization spectroscopy. Among slight variations of the technique, the principle of a phase measurement via the interference of two-photon quantum pathways always remains. Recently (2017), a significant angle dependence of the sideband phase caused by the interplay of partial waves with different angular momenta has been observed [51]. Due to the underlying continuum-continuum (cc) transitions, such an interplay is intrinsically present in any variant of RABBITT experiment. Different experimental and theoretical studies of this angular dependence followed [52–54].

In the publication presented in this chapter, Section 4.1, a novel experimental protocol is developed, which allows one to disentangle the amplitudes and phases of all contributing quantum pathways and their associated partial waves to a single sideband. The procedure is demonstrated to give access to time delays arising from different cc-transitions in helium. In Section 4.2, a step-by-step derivation of the anisotropy parameters of the photoelectron angular distribution used in the publication is carried out. Further, analytic estimates for the observed cc-phase differences are presented in Section 4.3. Finally, in Section 4.4, the presented experimental technique is applied to other, larger species before concluding.

Details about the publication printed in this chapter are listed below. The text and figures are as in the publication. Only the style of the text, figures and equations has been adapted to the style of the thesis. Further, the numbering of the figures and references has been adjusted. The reference list of the publication has been included in the reference list of the thesis. The mathematical notation is kept as in the original publication and slightly varies from other parts of this thesis.

**Title:** "Time delays from one-photon transitions in the continuum", [55]  
**Journal:** *Optica*  
**doi:** 10.1364/OE.391791  
**URL:** <https://doi.org/10.1364/OPTICA.378639>  
**Published:** 3<sup>rd</sup> February 2020  
**License:** Creative Commons Attribution 4.0 License

©2020 Optical Society of America. Users may use, reuse, and build upon the article, or use the article for text or data mining, so long as such uses are for non-commercial purposes and appropriate attribution is maintained. All other rights are reserved.

## 4.1 Time delays from one-photon transitions in the continuum

*Jaco Fuchs*<sup>1,\*</sup>, *Nicolas Douguet*<sup>2</sup>, *Stefan Donsa*<sup>3</sup>, *Fernando Martin*<sup>4,5,6</sup>,  
*Joachim Burgdörfer*<sup>3</sup>, *Luca Argenti*<sup>2,7</sup>, *Laura Cattaneo*<sup>1</sup>, *Ursula Keller*<sup>1</sup>

<sup>1</sup> Department of Physics, Eidgenössische Technische Hochschule Zürich, Zürich, Switzerland <sup>2</sup> Department of Physics, University of Central Florida, Orlando, Florida, USA <sup>3</sup> Institute of Theoretical Physics, Vienna University of Technology, Vienna, Austria, EU <sup>4</sup> Departamento de Química Modulo 13, Universidad Autónoma de Madrid, 28049 Madrid, Spain, EU <sup>5</sup> Condensed Matter Physics Center (IFIMAC), Universidad Autónoma de Madrid, 28049 Madrid, Spain, EU <sup>6</sup> Instituto Madrileño de Estudios Avanzados en Nanociencia (IMDEA-Nano), 28049 Madrid, Spain, EU <sup>7</sup> CREOL, University of Central Florida, Orlando, Florida 32186, USA

\* [jafuchs@phys.ethz.ch](mailto:jafuchs@phys.ethz.ch)

Attosecond photoionization time delays reveal information about the potential energy landscape an outgoing electron wavepacket probes upon ionization. In this study we experimentally quantify, for the first time, the dependence of the time delay on the angular momentum of the liberated photoelectrons. For this purpose, electron quantum-path interference spectra have been resolved in energy and angle using a two-color attosecond pump-probe photoionization experiment in helium. A fitting procedure of the angle-dependent interference pattern allows us to disentangle the relative phase of all four quantum pathways that are known to contribute to the final photoelectron signal. In particular, we resolve the dependence on the angular momentum of the delay of one-photon transitions between continuum states, which is an essential and universal contribution to the total photoionization delay observed in attosecond pump-probe measurements. For such continuum-continuum transitions, we measure a delay between outgoing *s*- and *d*-electrons as large as 12 as close to the ionization threshold in helium. Both single-active-electron and first-principles *ab initio* simulations confirm this observation for helium and hydrogen, demonstrating the universality of the observed delays.

### 4.1.1 Introduction

Free electrons cannot exchange photons with a light pulse. Unbound electrons, however, which are subject to an external potential, can absorb (inverse Bremsstrahlung) or emit (stimulated Bremsstrahlung) quanta of the radiation field. In the presence of an attractive Coulomb potential of a nearby ion the absorption and emission of a single photon promote dipole transitions that change the quantum state. These transitions involve bound as well as continuum states, giving rise to various types of radiative processes such as excitation (bound to bound), ionization (bound to continuum, bc), recombination (continuum to bound), and continuum-continuum (cc) transitions.

Recent progress in attosecond science has given direct access to timing information in photon-atom interaction on the attosecond scale. In particular, single-photon ionization and the corresponding Eisenbud-Wigner-Smith (EWS) delay [29, 31, 32, 56, 57] attracted lots of attention. Briefly, due to the propagation across the potential-energy landscape the excited photoelectron wave packet acquires an energy-dependent phase which results in a measurable group delay, referred to as a photoionization time delay. Relative delays between wave packets from different species [34–36], ionization channels [5, 6, 37–39, 58, 59], and emission angles [51, 52], have been measured to very high accuracy and serve as benchmarks for time-dependent quantum mechanical simulations in atoms [6, 34, 35, 37, 51, 52], molecules [36, 38, 39, 58], and solids [5, 40]. To date, these attosecond measurement techniques are based on the delay between two coherent laser pulses, which are typically in the extreme ultraviolet (XUV) and the infrared (IR). Thus the time delays could only be measured between ionization pathways involving at least two photons. In particular, if the first photoabsorption event is a bound-continuum (bc) transition, a second transition in the continuum is required to access temporal information in state-of-the-art experiments. Thus, in addition to the EWS delay [31, 32], the experimentally observed delays contain two more contributions. The first one originates from the spectral phase of the ionizing attosecond pulse train (APT) [18, 60] and cancels out when comparing different species or channels. The second contribution originates from the cc-transitions mediated by the probing IR laser pulse [56, 57, 61]. Al-



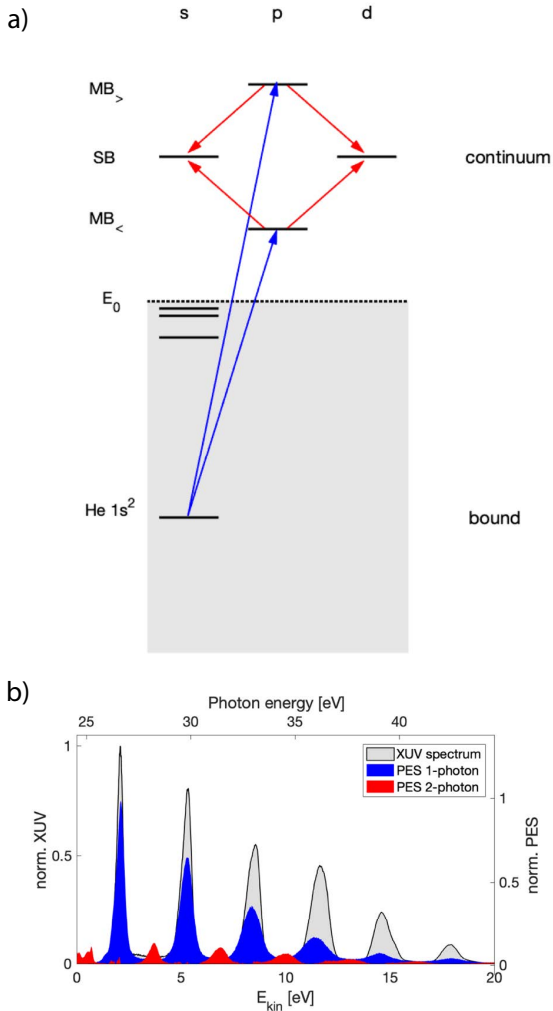


**Figure 4.1:** a) Quantum pathways leading to the same sideband. The XUV (blue) mediates bound to continuum transitions (ionization), the IR (red) mediates transitions within the continuum. All quantum pathways interfere. b) Experimental XUV and photoelectron energy spectra (PES). The one-photon PES is obtained by an XUV only measurement. The two-photon PES is obtained by subtracting the one-photon spectrum from the time-integrated RABBITT spectrum.

though it is well known [29, 30, 62] that the cc-contribution to the photoionization time delay can be comparable or even larger than the EWS delay for single-photon ionization, it has not drawn much attention until recently. Moreover, since experimentally disentangling the contributions has not been possible so far, time delays of one-photon ionization were only accessible when referencing to theoretical calculations [30, 56, 59].

Recently, experimental evidence of a strong effect of the IR-induced cc-transitions on the angular dependence of the total photoemission delays has been reported [51, 52] stimulating several independent investigations on the origin of this effect [53, 54, 62–66]. In this work, we present a new method that allows us to unravel the delay between electron wave packets from different one-photon transitions in the continuum, purely from experimental data and independently of the Wigner and XUV contributions. We obtain for first time access to the angular momentum dependence of the EWS delay for cc-transitions. The method is based on an algorithm developed to analyze angularly resolved RABBITT (Reconstruction of Attosecond Beating By Interference of Two-photon Transitions [4]) spectra. We find an ubiquitous positive and energy-dependent time delay, as large as 12 as, between *s*- and *d*-wave photoelectrons produced by the additional IR-photon exchange that follows photoionization of atomic helium by an XUV attosecond pulse train. This result is the first demonstration of a direct measurement of the EWS delay arising from one-photon transitions within the continuum. Using two independent computational methods to solve the time-dependent Schrödinger equation (TDSE), one based on the single-active-electron approximation and the other being a first-principles *ab initio* approach, we obtain excellent agreement with the experimentally retrieved ionization time delays. These findings confirm that, in helium, at energies close to the first ionization threshold, the delay associated with radiative transitions in the continuum is dominated by the electron angular momentum and radial momentum distribution, whereas electronic correlation plays no significant role.

The following section develops the theoretical framework needed to interpret the experiment and the simulations. The experimental and theoretical analyses are described in Sections 4.1.3 and 4.1.4, respectively. The main results will be examined in Section 4.1.5, and in the last section, we

offer our conclusions.

### 4.1.2 Theoretical framework

In the photoionization of helium from its  $1s^2$  ground state by absorption of a single XUV photon, the total angular momentum of the combined atom-photon system has to be conserved. In the energy range examined in this work, the residual  $\text{He}^+$  ion remains in its lowest  $^2S$  ( $1s$ ) state. The photon angular momentum, therefore, is entirely transferred to the ejected electron, which is emitted as a p-wave (angular momentum  $\ell = 1$ ). This liberated electron can subsequently absorb (or emit) an additional IR photon through a cc-transition, which transfers to the photoelectron additional angular momentum resulting in either an  $s$ -wave ( $\ell = 0$ ) or  $d$ -wave ( $\ell = 2$ ). For collinear parallel polarized XUV and IR pulses, as those employed in this study, the magnetic quantum number remains zero.

In the RABBITT technique [4, 13], an XUV pulse train consisting of odd harmonics of the fundamental IR laser frequency  $\omega$  is used to ionize the target, leading to single-photon peaks (mainbands) in the photoelectron spectrum separated by twice the laser photon energy  $2\hbar\omega$ . A weak replica of the fundamental IR with frequency  $\omega$  then triggers cc-transitions from the mainband to sidebands with kinetic energies lying between the mainbands. For ionization from an  $s$ -shell, four main quantum pathways contribute to each sideband, namely, the transitions  $s \rightarrow p \rightarrow s$  and  $s \rightarrow p \rightarrow d$ , for both the absorption and stimulated emission of the IR photon, as illustrated schematically in Figure 4.1a. At low IR intensities (less than few  $\text{GW}/\text{cm}^2$  at 800 nm), pathways to the sidebands that involve the exchange of more than one IR photon give a negligible contribution, and hence, states with angular momentum higher than two are not populated. Due to the interference of absorption and emission pathways, the sideband signal oscillates as a function of the delay  $\tau$  between the IR pulse and the XUV pulse train. In Fig. 4.1b, we show the spectrum of the XUV pulse train and the corresponding photoelectron energy spectrum (PES) of one-photon and two-photon pathways.

In the weak-field regime, the  $s$  ( $\ell = 0$ ) and  $d$  ( $\ell = 2$ ) photoionization amplitudes at the sideband with energy  $E_f$  can be expressed, within low-

est order of perturbation theory, by the well-known two-photon-transition formula [67]

$$\begin{aligned} \mathcal{A}_l^{(2)}(E_f) &= -i \int d\Omega M_{E_f,l}^{(2)}(\Omega) E_{XUV}(\Omega) E_{IR}([E_f - I_p]/\hbar - \Omega) \\ &= \mathcal{A}_l^{(2+)} + \mathcal{A}_l^{(2-)} \end{aligned} \quad (4.1)$$

where  $M_{E_f,l}^{(2)}$  is the two-photon matrix element,  $I_p$  is the ionization potential and  $E_{XUV}$  and  $E_{IR}$  are the Fourier transforms of the XUV and IR electric field, respectively.

The frequency (energy) integral in Eq. (4.1) can be split into an interval with  $0 < \Omega < (E_f - I_p)/\hbar$ ,  $\mathcal{A}_l^{(2+)}$ , which corresponds to pathways with absorption of an IR photon and an integral with  $\Omega \geq (E_f - I_p)/\hbar$ ,  $\mathcal{A}_l^{(2-)}$ , for the pathways with stimulated emission of an IR photon. Following [30, 61], for a narrow-band IR spectrum with frequency  $\omega$  far from resonances, the phase of the two-photon matrix element (Eq. (4.1)) can be decomposed into three additive contributions

$$\mathcal{A}_l^{(2\pm)} = |\mathcal{A}_l^{(2\pm)}| e^{i(\varphi_l^{cc\pm} + \varphi_{\lesseqgtr}^{bc} \pm \omega\tau)} \quad (4.2)$$

with  $\varphi_l^{cc\pm}$  the phase of the cc-transition with final angular momentum  $l$ ,  $\varphi_{\lesseqgtr}^{bc}$  the phase of the one-photon bc-transition to the lower (<) or upper (>) main band and the phase  $\pm\omega\tau$  due to the pump-probe delay  $\tau$ , which leads to oscillations in the interference pattern. The resulting ionization probability at the sideband is

$$\begin{aligned} I(\vartheta, \varphi, \tau) &= |(\mathcal{A}_s^{(2+)} + \mathcal{A}_s^{(2-)})Y_0^0(\vartheta, \varphi) \\ &\quad + (\mathcal{A}_d^{(2+)} + \mathcal{A}_d^{(2-)})Y_2^0(\vartheta, \varphi)|^2 \\ &= \sum_{n=0}^4 \beta_n(\tau) P_n[\cos(\vartheta)] \end{aligned} \quad (4.3)$$

where  $\vartheta$  is the angle between the common laser polarisation axis of the XUV and IR electric field, and the direction of the outgoing electron. The series expansion in Legendre polynomials  $P_n$  extends up to fourth-order [68]. The coefficients  $\beta_n(\tau)$ , which quantify the photoemission anisotropy,

have the following expressions

$$\begin{aligned}\beta_0 = & |\mathcal{A}_s^{(2+)}|^2 + |\mathcal{A}_s^{(2-)}|^2 + |\mathcal{A}_d^{(2+)}|^2 + |\mathcal{A}_d^{(2-)}|^2 \\ & + 2|\mathcal{A}_s^{(2+)}||\mathcal{A}_s^{(2-)}| \cos(2\omega\tau + \varphi_s^{(2+)} - \varphi_s^{(2-)}) \\ & + 2|\mathcal{A}_d^{(2+)}||\mathcal{A}_d^{(2-)}| \cos(2\omega\tau + \varphi_d^{(2+)} - \varphi_d^{(2-)}),\end{aligned}\quad (4.4)$$

$$\begin{aligned}\beta_2 = & \frac{10}{7} [|\mathcal{A}_d^{(2+)}|^2 + |\mathcal{A}_d^{(2-)}|^2 \\ & + 2|\mathcal{A}_d^{(2+)}||\mathcal{A}_d^{(2-)}| \cos(2\omega\tau + \varphi_d^{(2+)} - \varphi_d^{(2-)})] \\ & + 2\sqrt{5} [|\mathcal{A}_s^{(2+)}||\mathcal{A}_d^{(2+)}| \cos(\varphi_s^{(2+)} - \varphi_d^{(2+)}) \\ & + |\mathcal{A}_s^{(2-)}||\mathcal{A}_d^{(2-)}| \cos(\varphi_s^{(2-)} - \varphi_d^{(2-)}) \\ & + |\mathcal{A}_s^{(2+)}||\mathcal{A}_d^{(2-)}| \cos(2\omega\tau + \varphi_s^{(2+)} - \varphi_d^{(2-)}) \\ & + |\mathcal{A}_s^{(2-)}||\mathcal{A}_d^{(2+)}| \cos(2\omega\tau + \varphi_d^{(2+)} - \varphi_s^{(2-)})],\end{aligned}\quad (4.5)$$

$$\begin{aligned}\beta_4 = & \frac{18}{7} [|\mathcal{A}_d^{(2+)}|^2 + |\mathcal{A}_d^{(2-)}|^2 \\ & + 2|\mathcal{A}_d^{(2+)}||\mathcal{A}_d^{(2-)}| \cos(2\omega\tau + \varphi_d^{(2+)} - \varphi_d^{(2-)})].\end{aligned}\quad (4.6)$$

Since s- and d-waves have the same (even) parity, the odd anisotropy parameters  $\beta_1$  and  $\beta_3$  are identically zero. Here

$$\varphi_{s,d}^{(2\pm)} = \varphi_{s,d}^{cc\pm} + \varphi_{\leq}^{bc} \quad (4.7)$$

contains both the phase  $\varphi_{s,d}^{cc\pm}$  of the cc-transition and the phase  $\varphi_{\leq}^{bc}$  associated with the preceding ionization. The latter one contains the phase of the ionizing XUV pulse and the atomic phase  $\delta_l^{bc}$  for the half-scattering process of the outgoing electron wavepacket at the atomic potential. Its spectral derivative  $d\delta_l^{bc}(E)/dE$  gives the EWS delay for single photon ionization. The phase of the cc-transition  $\varphi_{s,d}^{cc\pm}$  then leads to an additional delay often referred to as cc-delay [61] or Coulomb laser coupling (CLC) delay [57]. However, since the IR-driven cc-transition occurs primarily at large distances from the atomic core [30], the accumulated phase, unlike for one-photon ionization does not account for the full half-scattering phase but only for the propagation in the long-range tail of the atomic potential. Therefore, the influence of the centrifugal potential  $L^2/2r^2$  on

the cc-phase was previously neglected in the analytical approximation to  $\varphi^{cc}$  [30].

### 4.1.3 Experimental results

In order to measure the time- and angle-dependent ionization probability (Eq. (4.3)), we use a COLTRIMS detector [50] in combination with an XUV-IR pump-probe setup. An amplified Ti:Sapphire laser, with a repetition rate of 10 kHz, generates a 790 nm IR pulse of 29 fs FWHM duration and 0.7 mJ total energy. The pulse is split into an intense (80%) and a weaker (20%) component. The stronger IR beam is focused into an argon gas cell where the XUV harmonics 13 to 25, corresponding to an energy range from 20 to 40 eV, are created by high harmonic generation [16] (see Figure 4.7b). The remaining IR pulse passes through a delay stage and is recombined with the XUV beam, before being focused into a cold helium jet. With the COLTRIMS detector, we measure the three-dimensional momentum of both photoelectrons and ions with a  $4\pi$  solid angle detection capability. With coincidence-selection (time-of-flight filtering of the helium ion and momentum conservation condition), we can discriminate against electrons from other reactions. The delay between the two pulses is controlled via a piezo-driven delay stage in combination with an active interferometric stabilization. For details on the experimental setup, the reader is referred to [48].

To guarantee a uniform detection capability over all emission angles and energies, we calibrate the detector efficiency using a helium XUV-only measurement, where the differential cross section is known accurately. For the time-resolved measurements, an IR intensity of  $3 \cdot 10^{11} \text{ W/cm}^2$  is used at the interaction region. The angle and time-dependent photoelectron spectra are recorded for 40 delay steps. The resulting angular distributions are then projected on the Legendre polynomials, Eq.(4.3), to retrieve the anisotropy parameters of the distribution, which are shown in Figure 4.2. The sideband signal is integrated over 0.5 eV, as indicated for sideband 18 by the yellow lines.

Figure 4.3 shows the anisotropy parameters for sideband 18 as a function of the time delay. Each of the three beta parameters oscillates at twice

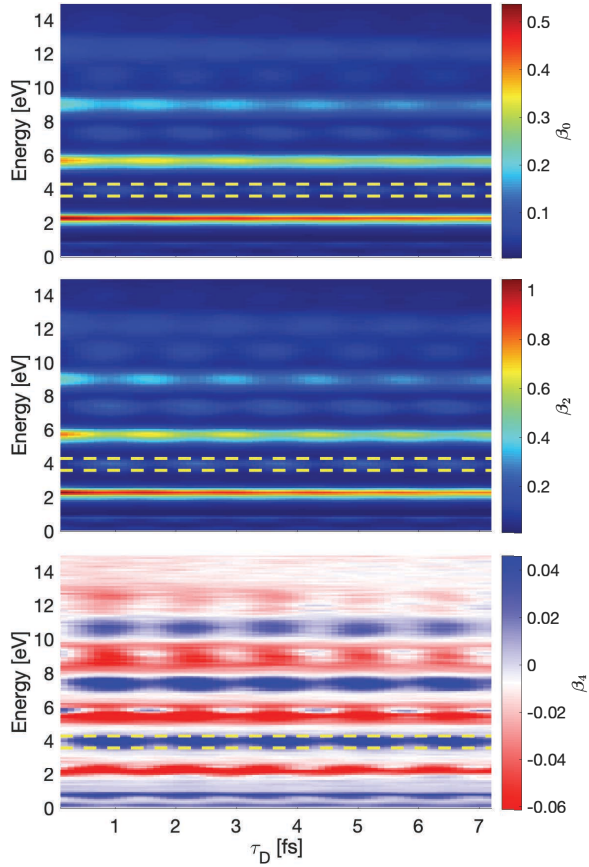


**Figure 4.2:** Experimental anisotropy parameters of the time-resolved photoelectron angular distribution,  $\beta_0$  (top),  $\beta_2$  (centre) and  $\beta_4$  (bottom). The yellow lines indicate the integration range of sideband 18. A positive delay indicates that the IR pulse is delayed with respect to the XUV; the zero delay is chosen arbitrarily.

the IR frequency,  $\beta_n = a + b \cos(2\omega\tau - \varphi)$ , with offset  $a$ , amplitude  $b$ , and phase  $\varphi$ , which are directly related to the parameters in equations (4.4) – (4.6).

The system of equations (4.4) – (4.6) has in total four unknown amplitudes and four unknown phases. The phases appear in differences only and are thus only determined up to an overall constant, allowing us to set one of the phases to zero without loss of generality. The remaining seven variables can then be simultaneously fitted to the system of equations using a least square minimization routine based on the Levenberg-Marquardt-algorithm [69]. The convergence of the fit to the correct set of parameters has been tested by performing the same fitting procedure on sets of artificial data, directly generated from equations (4.4) – (4.6), both with and without typical measurement noise (up to 5% relative noise of each anisotropy parameters). For the experimental sampling frequency and number of points the error of the retrieved phases stays below 0.01 rad. Figure 4.3 shows the fit to the experimental data for sideband 18. Making use of both the angle-dependent phase and amplitude of the RABBITT interference pattern we can thus determine the amplitudes and relative phases of all four quantum paths contributing to any given sideband. In particular, the relative phase between the two pathways which lead to different angular momenta, is for the absorption

$$\begin{aligned} \varphi_s^{(2+)} - \varphi_d^{(2+)} &= \varphi_s^{cc+} + \varphi_{(<)}^{bc} - \varphi_d^{cc+} - \varphi_{(<)}^{bc} \\ &= \varphi_s^{cc+} - \varphi_d^{cc+}, \end{aligned} \quad (4.8)$$

and for stimulated emission of an IR photon

$$\begin{aligned} \varphi_s^{(2-)} - \varphi_d^{(2-)} &= \varphi_s^{cc-} + \varphi_{(>)}^{bc} - \varphi_d^{cc-} - \varphi_{(>)}^{bc} \\ &= \varphi_s^{cc-} - \varphi_d^{cc-}. \end{aligned} \quad (4.9)$$

This enables to directly measure the influence of the final-state angular momentum on the cc-phase independent of the preceding one-photon bound-free transition.

Indeed, in each case, we retrieve the phase difference between pathways involving the same intermediate state, i.e., cc-transitions following the absorption of XUV photons of the same energy. Consequently, the



phase of the bc-transition, which includes both XUV chirp and the  $p$ -wave scattering phase, cancels out, such that the remaining phase difference is purely due to the one-photon transition in the continuum.

In contrast to the traditional RABBITT analysis [18, 60], where phase differences  $\varphi(E + \omega) - \varphi(E - \omega)$  are extracted in order to approximate the phase derivative, our method yields an (absolute) phase difference at a fixed energy. In detail, in RABBITT, the total angle-integrated sideband phase contains the phase difference between pathways originating from neighboring harmonics, i.e., an approximated phase derivative across two harmonics. Therefore, even when comparing different species, the measured delays correspond to differences of derivatives, or respectively, differences in group delay. As a consequence, absolute phase differences remain hidden. In contrast, by comparing pathways following the absorption of the same harmonic, the present procedure allows us to extract an absolute phase difference between two pathways.

Figure 4.4 and 4.5 show the mean of the experimentally retrieved phases for sidebands 18, 20, and 22, averaging over four independent measurements. The error bars represent the uncertainty of the mean, indicating an estimate for the total uncertainty of the combined measurement and fitting procedure.

#### 4.1.4 Theoretical results

In order to prove the validity of the present extraction method, we apply the same fitting procedure to computed RABBITT traces, for which the total phase of the two-photon electron wave packet and thus the cc-phase can be directly accessed. We performed SAE calculations [70, 71], where the TDSE for helium is solved using the potential of Ref. [72] and a finite-difference scheme based on the Crank-Nicolson method. The sideband signal is analyzed in the same way as the experimental data and illustrated with the corresponding fit in Figure 4.3 (center). The retrieved values for the phase difference between the  $s$ - and  $d$ -final-state partial waves are shown in Figures 4.4 and 4.5 for sidebands 18 to 24. In addition, by using a single harmonic in the TDSE calculations, we directly retrieve the phase of the outgoing  $s$ - and  $d$ -waves at the neighboring sidebands with-

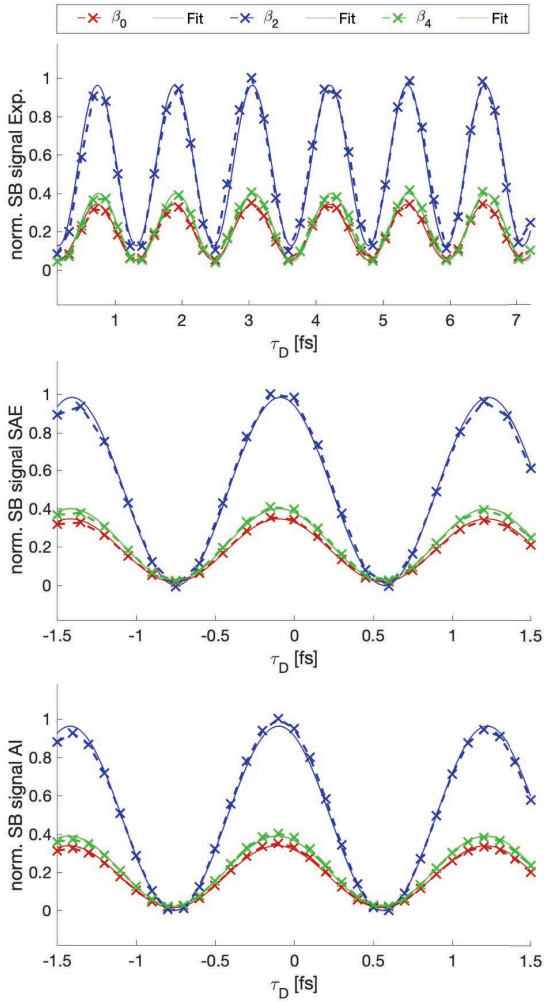


**Figure 4.3:** Simultaneous fit of the sideband anisotropy parameters. The time resolved sideband signal and the simultaneous fit of the anisotropy parameters  $\beta_0$ ,  $\beta_2$  and  $\beta_4$  are shown for sideband 18 for the experimental data (top), the SAE calculations (middle) and the full ab initio (bottom), respectively.

out the need to invoke interferences of different pathways. Using the latter procedure, we find excellent agreement (below 0.015 rad absolute difference) with the fitted phases, thereby confirming the validity of the present extraction method.

To probe for the possible influence of electron correlation and exclude possible shortcomings of the SAE approximation, we additionally perform full *ab initio* simulations using the time-dependent close-coupling method [73] on a spatial FEDVR grid [74] thereby solving the full two-electron TDSE for atomic helium from first principles [75, 76]. The electric fields are treated in the dipole approximation. Both, the *ab initio* and the SAE simulation employ an IR pulse with central wavelength of 790 nm and a Gaussian envelope with 8 fs FWHM. The spectral amplitude and phase of each harmonic were chosen to match the experimental spectrum. We have checked for the potential influence of the IR pulse duration on the extracted phases. The excellent agreement of the results from SAE simulations for two different IR pulse durations of 8 fs and 20 fs FWHM allows one to rule out any significant pulse duration effects on the resulting phases.

Comparing the results of the two independent simulation methods with the experiment in Figs. 4.4 and 4.5, we observe excellent agreement between all three data sets. We therefore can conclude that the effect of electron correlation on the cc-transition is negligible or identical for the contributing pathways in the investigated energy range.

In addition, we report calculations for the hydrogen atom, for which harmonics from the 9<sup>th</sup> to the 17<sup>th</sup> order are used to generate the XUV spectrum, such that the electron kinetic energy remains in the same range as for helium. It can be observed in Figs. 4.4 and 4.5 that the retrieved phase delays exactly follow the helium trend, thus supporting the argument of negligible influence from both electron correlation effects and the short-range helium potential on the investigated cc-transition time delays.

#### 4.1.5 Discussion

We observe a remarkable quantitative agreement between the experiment and theoretical values for the phase difference  $\varphi_s^{cc\pm} - \varphi_d^{cc\pm}$  for electron en-

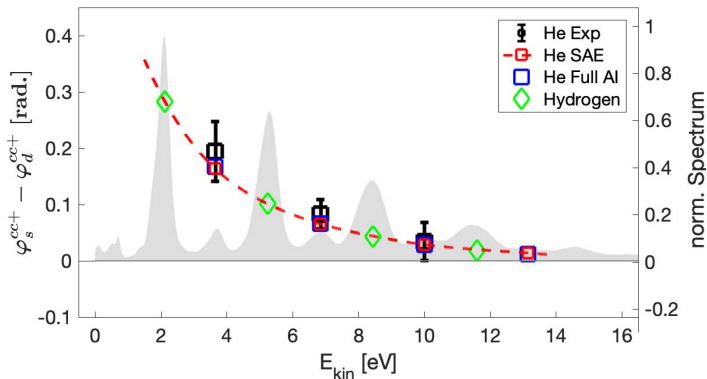


**Figure 4.4:** Difference  $\varphi_s^{cc+} - \varphi_d^{cc+}$  in radians for the cc-transition involving absorption. The experimental values represent the mean values of four measurements and the error bars correspond to the uncertainty of the mean. The discrepancy between the two simulations lies below 2% of their absolute value. The shaded area represents the PES given in Fig. 4.1.

ergies  $2 \text{ eV} \leq E \leq 14 \text{ eV}$  obtained from two independent computational methods for both hydrogen and helium. We have found a significant phase difference with a maximum value of 0.21 rad between *s*- and *d*-partial waves at harmonic 18 corresponding to a final-state with energy of 3.7 eV. Our data reveals three main features:

- i. The relative phase between the *s*- and *d*-partial-wave is ubiquitous positive and decreases with energy, both for cc-transitions involving absorption and stimulated emission at all kinetic energies.
- ii. At all sidebands, the absolute values of the phase difference between *s*- and *d*-wave are almost equal for absorption and stimulated emission. The discrepancy lies far below the experimentally accessible precision. The theoretical values indicate slightly larger delays for absorption.
- iii. The cc-phase difference converges to zero with increasing kinetic energy.

Although the observed phase difference has not been experimentally identified in the past, the above observations are visible already in earlier numerical simulations [62], and they have been predicted by Dahlström

and co-workers [53, 61, 64, 77], see also supplemental material in [52].

Qualitatively the trend mirrors the observation of partial-wave interferences resulting in electron-spin polarization in one-photon bc-transitions [78–80]. The observations (i)-(iii) are fully consistent with the influence of the final-state centrifugal potential on the continuum scattering phase and on the EWS time delay, in the present case for continuum-continuum transitions. Observation (iii) is the obvious consequence of the decreasing effect of the underlying potential energy landscape on the escaping electron. For increasing energies, the wave function tends towards the behavior of a free spherical wave for which all delays vanish. Moreover, with increasing momentum of the outgoing wave packet, the cc-transition is effectively shifted to larger distances from the ionic core at which the centrifugal potential  $\propto 1/r^2$  becomes negligible compared to the Coulomb potential. The latter was the underpinning of the previous analytic estimates of the cc-phase and time delay in which the angular momentum dependence was neglected [30].

Observation (i) clearly shows that the cc-phase is in fact related directly to the EWS phase for cc-scattering. This is supported by the observation that the phase and corresponding delay qualitatively resembles the EWS delay for bound-continuum transitions to different angular momentum states [57, 78–80]. The fact that the retrieved phases are significantly smaller (by factors 3 to 4) relative to the scattering phase is due to the fact that, unlike for the bc-transition, the cc-transition in the two-photon scenario probes the potential landscape not for the full half-scattering but only at large distances where the centrifugal potential is weaker, yet still leads to clearly resolvable effects at low energies.

Observation (ii) then confirms the fact that the relevant phase is accumulated at distances where the Coulomb potential ( $1/r$ ) dominates, the centrifugal potential provides a (small) correction, and short-ranged contributions are entirely negligible. Therefore, the observed phases are universal for a given angular momentum, i.e., independent of the atomic species, and slightly larger for absorption than for emission. The latter is in line with the fact that the outgoing wave packet after the bc-transition propagates initially slower before absorption, thereby enhancing the in-

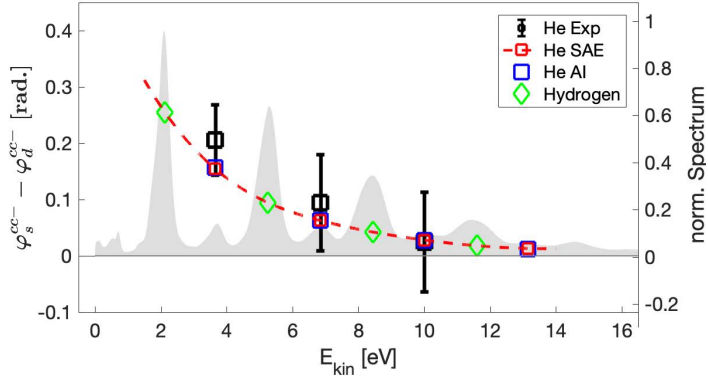


**Figure 4.5:** Difference  $\varphi_s^{cc-} - \varphi_d^{cc-}$  for the cc-transition involving stimulated emission, otherwise same as Figure 4.4.

fluence of the centrifugal potential on the subsequent cc-transition. For the same reason, we thus expect the measured phases to depend on the wavelength of the laser field that drives the cc-transitions.

The resulting EWS delay between the  $s$ - and  $d$ -partial wave, observed experimentally for the first time in a cc-transition, allows for a simple, quasi-classical interpretation: Due to the different angular momentum, the rotational and radial energy distribution of the  $s$ - and  $d$ -wave packet components are different, and, since the rotational energy fraction is larger for the  $d$ -wave components, the radial expansion is slower. This implies a positive EWS delay  $\frac{d}{dE}(\delta_{l=2}(E) - \delta_{l=0}(E))$  of the  $d$ -wave relative to the  $s$ -wave, consistent with well-known trends for EWS delays in bound-continuum transitions. More generally, one expects larger delays for wave packet components with higher angular momentum quantum numbers. The experimental confirmation of this effect for cc-transitions and the quantification of its energy dependence are the main findings of this work. In the present experiment, in which the electron wave packet's center energy is 6.1 eV and the IR wavelength is 790 nm, the  $d$ -wave is retarded by 12 as relative to the  $s$ -wave. Higher order derivatives of the measured phase difference affect the shape of the envelope and lead to differences in chirp between the  $s$ - and  $d$ -partial waves. The implication for the wave packet

in time can be inferred from the Fourier integral over the spectral components of absorption and emission pathways of the two partial wave packets. As the phase difference between  $s$ - and  $d$ -waves are almost equal for absorption and stimulated emission, using  $\Delta\varphi_{sd} = \varphi_s^{cc} - \varphi_d^{cc}$ , the partial wave functions can be written in time domain as

$$\varphi_s(t) = \int A_s^{(2)}(\omega) e^{-i\omega t} d\omega \quad (4.10)$$

and

$$\varphi_d(t) = \int c_{d/s}(\omega) A_s^{(2)}(\omega) e^{-i\Delta\varphi_{sd}(\omega)} e^{-i\omega t} d\omega \quad (4.11)$$

where  $\omega = E_{kin}/\hbar$  and  $c_{d/s}(\omega) = |A_d^{(2)}(\omega)|/|A_s^{(2)}(\omega)|$  is the absolute amplitude ratio. Approximating the phase difference with a first order Taylor expansion  $\Delta\varphi_{sd}(\omega) = \Delta\varphi_{sd}(\omega_0) + \Delta\varphi'_{sd}|_{\omega_0}(\omega - \omega_0)$  around the center (mean) frequency  $\omega_0$  of the wave packet and assuming a weakly energy dependent amplitude ratio  $c_{d/s}(\omega) \approx c_{d/s}(\omega_0)$  it follows immediately that

$$\begin{aligned} \varphi_d(t) &= c_{d/s}(\omega_0) e^{i[\Delta\varphi'_{sd}|_{\omega_0}\omega_0 - \Delta\varphi_{sd}(\omega_0)]} \\ &\quad \int A_s^{(2)}(\omega) e^{-i\omega(t + \Delta\varphi'_{sd}|_{\omega_0})} d\omega \\ &= \varphi_s(t + \Delta\varphi'_{sd}|_{\omega_0}) c_{d/s}(\omega_0) e^{-i\Delta\varphi_0} \end{aligned} \quad (4.12)$$

where  $\Delta\varphi_0 = \Delta\varphi_{sd}(\omega_0) - \Delta\varphi'_{sd}|_{\omega_0}\omega_0$ . The assumption of a flat amplitude ratio is only valid for a narrow energy spectrum. An explicit study of the amplitude ratio for various species is given in [53, 81].

Hence, from Eq. (4.12) it follows that, additionally to the group delay  $\tau_{sd} = -\Delta\varphi'_{sd}|_{\omega_0}$ , an additional absolute phase offset  $\Delta\varphi_0$  is imparted to the  $d$ - relative to the  $s$ -partial wave. Both quantities, delay and absolute phase offset, strongly depend on the wave packet's center energy. The additional phase shift corresponds to an advance of the wave packets absolute phase with respect to the wave packet envelope. This phase lag between the  $s$ - and the  $d$ -wave in the outgoing wave packet implies an interesting analog to the carrier-envelope phase (CEP) slip. Although the absolute phase has no impact on the "classical" observables of the electron, i.e., spatial localization and momentum, it determines the interference. We hereby report an effect of the carrier-envelope phase imprinted in the photoelectron wave packet by the multiphoton ionization process.

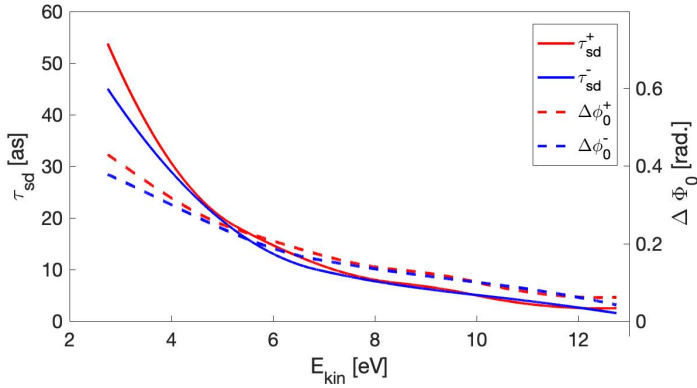


**Figure 4.6:** Delay  $\tau_{sd}$  and absolute phase offset  $\Delta\phi_0$  between the outgoing  $s$ - and  $d$ -partial waves as a function of the wave packets center energy for the phase difference retrieved from the SAE simulations.

It is illustrated together with the group delay  $\tau_{sd}$  as a function of the wave packet's center energy for the phases retrieved from the SAE simulations in Figure 4.6. As can be inferred from Figures 4.4 and 4.5, the theoretically calculated cc-phase difference in hydrogen follows the same trend as in helium. This finding further supports the notion that, in systems with small polarizability, such as helium, the relative phase between wave packet components with different angular momenta is a universal feature of laser-assisted Coulomb scattering when the Coulomb and the centrifugal potential dominate over any short-ranged admixtures [64, 77]. For larger atoms or molecules, where electron correlation effects are more prominent, however, deviations from the observed trend cannot be excluded.

At lower kinetic energies, even larger delays are to be expected. These were not measured in this work due to the limited tunability of the XUV spectrum in the present experiment. Sideband 16, in principle, would lie just above the helium ionization threshold and could be analyzed along those lines. However, higher excited states of the neutral helium atom come into play here [82] noticeable in Figure 4.2 (bottom). Including the latter sideband would then involve more complex transitions beyond cc-transitions and is beyond the scope of this work.



#### 4.1.6 Conclusion and outlook

In conclusion, we have established an experimental protocol exploiting a novel fitting procedure of angle-resolved RABBITT spectra, which allows us to determine the amplitudes and the relative phases of all quantum pathways that contribute to the same final energy in atomic helium. Comparing pathways following the absorption of the same XUV photon, we find a time delay between  $s$ - and  $d$ -waves arising from one-photon transitions in the continuum as large as 12 attoseconds. This represents the first measurement of the EWS time delay for (inverse) Bremsstrahlung. Moreover, we find excellent quantitative agreement between the experiment and two independent theoretical simulations. The observed trend reveals ubiquitous positive phase delays between  $s$ - and  $d$ -waves for both absorption and stimulated emission. The measured relative phase, which vanishes for high kinetic energies, is determined by the final state of the continuum wave packet components with different angular momentum populated by the two-photon transition. The radiative transition in the continuum occurs at large distances where the Coulomb potential of the nearby ion and the centrifugal potential dominate over the target-dependent short-range potential. As a consequence, the relative phases are expected to be a universal property of radiative transitions in the continuum that is relevant to characterize the photoemission dynamics for different atomic species. The same absolute phase difference affects the sideband anisotropy even in the stationary regime, as for example, in the laser-assisted ionization of helium with monochromatic synchrotron radiation.

This work not only serves as a proof-of-principle demonstration for accurately disentangling multiple interfering quantum pathways but also gives new physical insight into the time properties of the fundamental inverse and stimulated Bremsstrahlungs processes. The proposed method can be easily generalized to other systems and cc-transitions. The work opens up new experimental opportunities for analyzing and selecting quantum pathways in larger systems such as heavier atoms and molecules, where different quantum pathways can lead to distinct molecular breakup reactions or final states. Additionally, we hope that our study will motivate further experimental and theoretical studies of cc-transitions not only

in various atomic species, but more generally in small molecules, aiming for a general understanding of intermediate to long-range interactions on the photoemission time delay.

**Funding.** J.F., L.C., and U.K. acknowledge the support of the NCCR MUST, funded by the Swiss National Science Foundation. L.A. and N.D. acknowledge the support of the United States National Science Foundation under NSF Grant No. PHY-1607588 and by the UCF in-house OR Grant Acc. No. 24089045.

Parts of the calculations were performed on the Vienna Scientific Cluster (VSC3). S.D. and J.B. acknowledge the support by the WWTF through Project No. MA14-002, and the FWF through Projects No. FWF-SFB041-VICOM, and No. FWF-W1243-Solids4Fun, as well as the IMPRS-APS.

F.M. acknowledges the MINECO projects FIS2016-77889-R, the 'Severo Ochoa' Programme for Centres of Excellence in R&D (SEV-2016-0686) and the 'María de Maeztu' Programme for Units of Excellence in R&D (MDM-2014-0377).

**Disclosures.** The authors declare no conflicts of interest.

### Author contributions

J.F. led the study, U.K. supervised the study. J.F. and L.C. conducted the experiments. J.F. analyzed the experiments and developed the fitting procedure. N.D. and L.A. performed the SAE calculations. S.D. and J.B. performed the *ab-initio* calculations. All authors were involved in the interpretation and contributed to the final manuscript.

## 4.2 Derivation of the anisotropy parameters

In Section 4.1 analytic expressions for the anisotropy parameters (Equations (4.4) - (4.6)) are used to retrieve the amplitudes and phases of the contributing quantum pathways via a simultaneous fit. As their derivation is only briefly sketched, this section shall provide a step-by-step derivation.

The ionization probability (Equation (4.3)) follows as

$$\begin{aligned}
 I(\vartheta, \varphi, \tau) &= |(A_s^{(2+)} + A_s^{(2-)})Y_0^0(\vartheta) + (A_d^{(2+)} + A_d^{(2-)})Y_2^0(\vartheta)|^2 \\
 &= \underbrace{\left[ (A_s^{(2+)} + A_s^{(2-)}) (A_s^{(2+)} + A_s^{(2-)})^* \right]}_{f_{ss}(\tau)} Y_0^0(\vartheta) Y_0^0(\vartheta) \\
 &\quad + \underbrace{\left[ (A_s^{(2+)} + A_s^{(2-)}) (A_d^{(2+)} + A_d^{(2-)})^* + c.c. \right]}_{f_{sd}(\tau)} Y_0^0(\vartheta) Y_2^0(\vartheta) \quad (4.13) \\
 &\quad + \underbrace{\left[ (A_d^{(2+)} + A_d^{(2-)}) (A_d^{(2+)} + A_d^{(2-)})^* \right]}_{f_{dd}(\tau)} Y_2^0(\vartheta) Y_2^0(\vartheta),
 \end{aligned}$$

where the spherical harmonics  $Y_l^m(\vartheta)$  are independent of  $\varphi$  since  $m = 0$ , due to the common polarization axis of the XUV and IR light fields. One can separate the interference terms of  $s$ - with  $s$ -partial waves,  $s$ - with  $d$ -partial waves, and  $d$ - with  $d$ -partial waves, indicated by  $f_{ss}(\tau)$ ,  $f_{sd}(\tau)$  and  $f_{dd}(\tau)$ , respectively. The contributions of these interference terms vary with the electron emission angle due to the involved partial waves and corresponding spherical harmonics. Using Equation (4.2) one can explicitly write out these interference terms, which yields

$$\begin{aligned}
 f_{ss}(\tau) &= |\mathcal{A}_s^{(2+)}|^2 + |\mathcal{A}_s^{(2-)}|^2 \\
 &\quad + 2|\mathcal{A}_s^{(2+)}||\mathcal{A}_s^{(2-)}| \cos(2\omega\tau + \varphi_s^{(2+)} - \varphi_s^{(2-)}). \quad (4.14)
 \end{aligned}$$

$$\begin{aligned}
 f_{sd}(\tau) &= [|\mathcal{A}_s^{(2+)}||\mathcal{A}_d^{(2+)}| \cos(\varphi_s^{(2+)} - \varphi_d^{(2+)}) \\
 &\quad + |\mathcal{A}_s^{(2-)}||\mathcal{A}_d^{(2-)}| \cos(\varphi_s^{(2-)} - \varphi_d^{(2-)}) \\
 &\quad + |\mathcal{A}_s^{(2+)}||\mathcal{A}_d^{(2-)}| \cos(2\omega\tau + \varphi_s^{(2+)} - \varphi_d^{(2-)}) \\
 &\quad + |\mathcal{A}_d^{(2+)}||\mathcal{A}_s^{(2-)}| \cos(2\omega\tau + \varphi_d^{(2+)} - \varphi_s^{(2-)})] \quad (4.15)
 \end{aligned}$$

$$\begin{aligned}
 f_{dd}(\tau) &= |\mathcal{A}_d^{(2+)}|^2 + |\mathcal{A}_d^{(2-)}|^2 \\
 &\quad + 2|\mathcal{A}_d^{(2+)}||\mathcal{A}_d^{(2-)}| \cos(2\omega\tau + \varphi_d^{(2+)} - \varphi_d^{(2-)}). \quad (4.16)
 \end{aligned}$$

The ionization probability can then be written in a series of Legendre polynomials, for which the expansion coefficients are the anisotropy-parameters, see Equation (4.3). The Legendre polynomials  $P_n[x]$  form a complete, orthogonal system of polynomials with respect to the scalar

product  $\langle f, g \rangle = \int_{-1}^1 f(x)g(x)dx$ . In detail,  $\int_{-1}^1 P_n[x]P_m[x]dx = \frac{2}{2n+1}\delta_{nm}$ , where  $\delta_{mn}$  is unity if  $n = m$  and zero otherwise. The argument of the Legendre Polynomials is substituted by  $\cos(\vartheta)$  in order to adapt for the integration from 0 to  $\pi$ . The orthogonality of the Legendre polynomials allows for a determination of the anisotropy parameters via a projection of the ionization probability onto the corresponding polynomial,

$$\beta_n(\tau) = \frac{2n+1}{2} \int_0^\pi I(\vartheta, \tau) P_n[\cos(\vartheta)] \sin(\vartheta) d\vartheta \quad (4.17)$$

$$= f_{ss}(\tau) \underbrace{\frac{2n+1}{2} \int_0^\pi Y_0^0(\vartheta) Y_0^0(\vartheta) P_n[\cos(\vartheta)] \sin(\vartheta) d\vartheta}_{c_{ss}^n} \\ + f_{sd}(\tau) \underbrace{\frac{2n+1}{2} \int_0^\pi Y_0^0(\vartheta) Y_2^0(\vartheta) P_n[\cos(\vartheta)] \sin(\vartheta) d\vartheta}_{c_{sd}^n} \quad (4.18)$$

$$+ f_{dd}(\tau) \underbrace{\frac{2n+1}{2} \int_0^\pi Y_2^0(\vartheta) Y_2^0(\vartheta) P_n[\cos(\vartheta)] \sin(\vartheta) d\vartheta}_{c_{ss}^n} \\ = \sum_{l,l' \in s,d} c_{ll'}^n f_{ll'}(\tau) \quad (4.19)$$

Equation (4.17) is also used to obtain the anisotropy parameters from the experimentally measured photoelectron distribution. The integrals in Equation (4.18) can be determined explicitly. The corresponding algebraic values of the corresponding coefficients  $c_{ll'}^n$  are listed in Table 4.1. The odd anisotropy parameters vanish as for those the integrands are antisymmetric with respect to  $\pi/2$ . In detail, besides the odd Legendre polynomial  $P_n[\cos(\vartheta)]$ , which is antisymmetric with respect to  $\pi/2$ , only symmetric functions contribute to the integrands. Hence, the total integrands are antisymmetric and the integrals become zero. Further, all anisotropy parameters with  $n \geq 4$  vanish, since no higher order spherical harmonics contribute. Using the values from Table (4.1) and the interference terms from Equations (4.14)-(4.16) one obtains the expressions for the anisotropy parameters used for the simultaneous fit in Section 4.1, i.e. Equations (4.4)-(4.6). The expressions are multiplied by  $4\pi$  for normalization purposes.

	$n = 0$	$n = 1$	$n = 2$	$n = 3$	$n = 4$	$n \geq 5$
$c_{ss}^n$	$\frac{1}{4\pi}$	0	0	0	0	0
$c_{sd}^n$	0	0	$\frac{1}{4\pi}\sqrt{5}$	0	0	0
$c_{dd}^n$	$\frac{1}{4\pi}$	0	$\frac{1}{4\pi}\frac{10}{7}$	0	$\frac{1}{4\pi}\frac{18}{7}$	0

**Table 4.1:** Algebraic values of the coefficients  $c_{ll'}^n = \frac{2n+1}{2} \int_0^\pi Y_l^0(\theta)Y_{l'}^0(\theta)P_n[\cos(\theta)]\sin(\theta)d\theta$ , which determine the weights for the separate interference terms of the different partial waves to the anisotropy parameters, see Equation (4.19).

### 4.3 Analytic solution for the phase differences

In Section 4.1 experimentally measured values of the phase differences  $\Delta\varphi_{sd}^\pm = \varphi_s^{cc\pm} - \varphi_d^{cc\pm}$  between  $s$ - and  $d$ -partial waves induced by the cc-transitions are presented. Additionally, the corresponding values retrieved from SAE as well as ab-initio calculations are discussed. In this section an analytic solution for the phase difference between the two partial waves is derived. To this end, the Wentzel-Kramer-Brillouin (WKB) solution [83, 84] to the stationary Schrödinger equation (SE) of the hydrogen (H) atom is employed.

Due to the radial symmetry of the Coulomb potential the solution of the SE for the H-atom (or H-like atoms) can be written as a product of a radial function  $R_\ell(r)$  and spherical harmonics  $Y_{\ell,m}(\theta, \varphi)$  with angular momentum quantum numbers  $\ell = 0, 1, 2, \dots$  and magnetic  $m = -\ell, -\ell + 1, \dots, \ell - 1, \ell$ . The reduced SE for the radial part reads

$$-\frac{\hbar^2}{2\mu} \left[ \frac{1}{r^2} \frac{\partial}{\partial r} \left( r^2 \frac{\partial R_\ell(r)}{\partial r} \right) - \frac{\hbar^2 \ell(\ell+1)R_\ell(r)}{2\mu r^2} \right] + V_C(r)R_\ell(r) = ER_\ell(r), \quad (4.20)$$

where  $\mu$  is the effective mass of the electron-ion pair,  $E$  is the energy eigenvalue and  $V_C(r) = -e^2/(4\pi\epsilon_0 r)$  is the Coulomb potential with the elementary charge  $e$  and the vacuum permittivity  $\epsilon_0$ . The solution for bound states,  $E < 0$ , is textbook knowledge and leads to the well known discrete energy levels and our understanding of the periodic system of elements. Unbound solutions,  $E > 0$ , are less typical. They become problematic as normalization is only possible for wave packets, but not for single partial waves. Using the effective radial function  $u_\ell(r) = \frac{R_\ell(r)}{r}$ , Equation (4.20)

can be rewritten as

$$\left[ -\frac{\hbar^2}{2\mu} \frac{\partial^2 R(r)}{\partial r^2} + V_\ell^{eff}(r) \right] u_\ell(r) = E u_\ell(r) \quad (4.21)$$

with  $V_\ell^{eff}(r) = V_C(r) - \frac{\hbar^2 \ell(\ell+1)}{2\mu r^2}$ . Using the WKB approximation [83, 84] the solution follows as

$$u_\ell(E, r) = A \exp \left( \pm \frac{i}{\hbar} \int_{r_0}^r \sqrt{2\mu[E - V_\ell^{eff}(r')]} dr' \right), \quad (4.22)$$

where  $\pm$  corresponds to incoming or outgoing waves and  $r_0$  is considered a 'starting point' [61] (not to be confused with the Bohr radius). The solution directly allows to determine the phase difference between  $s$  ( $\ell = 0$ ) and  $d$  ( $\ell = 2$ ) partial waves after propagation out of the Coulomb potential,

$$\Delta\varphi_{sd}(E) = \varphi_s(E) - \varphi_d(E) \quad (4.23)$$

$$= \arg(u_0(E, \infty)) - \arg(u_2(E, \infty)) \quad (4.24)$$

$$= \frac{1}{\hbar} \int_{r_0}^{\infty} \sqrt{2\mu[E - V_{l=0}^{eff}(r')]} dr' - \frac{1}{\hbar} \int_{r_0}^{\infty} \sqrt{2\mu[E - V_{l=2}^{eff}(r')]} dr' \quad (4.25)$$

$$= \frac{1}{\hbar} \int_{r_0}^{\infty} \sqrt{2\mu\left[E + \frac{e^2}{4\pi\epsilon_0 r'}\right]} dr' - \frac{1}{\hbar} \int_{r_0}^{\infty} \sqrt{2\mu\left[E + \frac{e^2}{4\pi\epsilon_0 r'} - \frac{\hbar^2 2(2+1)}{2\mu r'^2}\right]} dr' > 0, \quad (4.26)$$

which is larger than zero for all  $r_0$  and  $E$ , in line with the experimentally retrieved values. Furthermore, for regions of  $r$  where the Coulomb potential dominates over the effective potential, and for sufficiently high energies, it holds that  $E + \frac{e^2}{4\pi\epsilon_0 r'} \gg \frac{\hbar^2 2(2+1)}{r^2}$ . Using the approximation  $\sqrt{1+x} \approx 1 + x/2$  for small  $x$  it then follows

$$\Delta\varphi_{sd}(E) = \frac{\sqrt{2\mu}}{\hbar} \int_{r_0}^{\infty} \sqrt{E + \frac{e^2}{4\pi\epsilon_0 r'}} \left( 1 - \sqrt{1 - \frac{6\hbar^2}{2\mu r'^2} \frac{1}{E + \frac{e^2}{4\pi\epsilon_0 r'}}} \right) dr' \quad (4.27)$$

$$\approx \frac{\sqrt{2\mu}}{2\hbar} \int_{r_0}^{\infty} \frac{6\hbar^2}{2\mu r'^2} \frac{1}{\sqrt{E + \frac{e^2}{4\pi\epsilon_0 r'}}} dr'. \quad (4.28)$$

The integral can then be solved exactly leading to

$$\Delta\varphi_{sd}(E) = \frac{6\hbar}{2\sqrt{2\mu}} \sqrt{\frac{4\pi\epsilon_0}{e^2}} \int_{r_0}^{\infty} \frac{1}{r'^2} \frac{1}{\sqrt{\frac{1}{r'} + \frac{4\pi\epsilon_0}{e^2}E}} dr' \quad (4.29)$$

$$= \frac{6\hbar}{2\sqrt{2\mu}} \sqrt{\frac{4\pi\epsilon_0}{e^2}} \left( -2\sqrt{\frac{1}{r'} + \frac{4\pi\epsilon_0}{e^2}E} \right) \Big|_{r_0}^{\infty} \quad (4.30)$$

$$= \frac{6\hbar}{\sqrt{2\mu}} \frac{4\pi\epsilon_0}{e^2} \left[ \sqrt{E + \frac{e^2}{4\pi\epsilon_0 r_0}} - \sqrt{E} \right]. \quad (4.31)$$

Two cases of the behaviour of  $\Delta\varphi_{sd}(E)$  can be distinguished.

(1) For large values of  $E$ , where  $E \gg \frac{e^2}{4\pi\epsilon_0 r_0}$ , one can use the same approximation as above ( $\sqrt{1+x} \approx 1 + x/2$  for small  $x$ ) to obtain

$$\Delta\varphi_{sd}(E) \approx \frac{3\hbar}{\sqrt{2\mu}r_0} \frac{1}{\sqrt{E}}. \quad (4.32)$$

This behaviour of  $\Delta\varphi_{sd}(E)$  being proportional to  $1/\sqrt{E}$  is also observed in the experiment.

(2) For small values of  $E$ , a deviation from the  $1/\sqrt{E}$  behavior occurs. Specifically, for  $E \rightarrow 0$ , the phase difference does not diverge but approaches a finite maximal value, depending on the starting point  $r_0$ .

The analytic estimate (4.31) can be fitted to the experimental data with  $r_0$  being the only fit parameter. Here, 5.7 nm is obtained for  $r_0$  when fitting to either of the phase differences  $\Delta\varphi_{sd}^+(E)$  or  $\Delta\varphi_{sd}^-(E)$ , respectively. These values are significantly larger than the Bohr radius. This can be interpreted as the initial expansion of the wave packet after single-photon photoionization, before the cc-transition splits into partial waves with different angular momenta.

It has to be noted that the nature of the two-photon process itself and the underlying cc-transitions are omitted entirely. The expression (4.31) only accounts for the phase difference which is acquired during the propagation through the Coulomb potential of the residual ion, starting at a well defined  $r_0$ . Nevertheless, it demonstrates that the phase difference for different angular momenta, which is purely accumulated during the propagation through the long-range tail of the Coulomb potential and is

inherently present in any photoionization process, can significantly affect the measured photoionization phase of different partial waves.

#### 4.4 Investigation of larger atoms

In Section 4.1 the phase differences  $\varphi_s^{cc\pm} - \varphi_d^{cc\pm}$  between  $s$ - and  $d$ -partial waves induced by the  $cc$ -transitions in a two-color photoionization experiment in helium have been quantified. The excellent agreement between experimental and theoretical values demonstrates an angular momentum contribution to the photoionization time delay. Furthermore, simulations in atomic hydrogen suggest that this angular momentum contribution to the photoionization time delay has a universal character across different chemical species. The analytic estimate in Section 4.3 supports this argument as it indicates that the major contribution to the phase differences originates from the propagation of the photoionized wave packets across the long-range part of the Coulomb potential, whereas the short-range potential plays a minor role. The question arises if indeed  $cc$ -phase differences can be observed in larger species as well, and whether they follow the same trend. This section presents an overview of the study of larger noble gases and details a measurement of the  $cc$ -phase difference in argon.

In order to retrieve the phase differences  $\varphi_s^{cc+} - \varphi_d^{cc+}$  a simultaneous fit of the amplitudes and relative phases of the contributing quantum pathways to the anisotropy parameters of a single SB has to be carried out. In principle, phase differences with other angular momentum quantum numbers such as  $\varphi_p^{cc+} - \varphi_f^{cc+}$  could be retrieved in a similar way. For species with a  $p$ -ground state such as argon or neon, the single-photon ionization by an XUV photon leads to  $s$ - and  $d$ -partial waves in the continuum. The subsequent interaction with an IR photon then leads to  $p$ - and  $f$ -waves for the two-photon case. However, significantly more quantum pathways contribute to the same SB in this case, such that the complexity of the simultaneous fit drastically increases. In detail, the  $p$ -ground state comprises electrons with magnetic-quantum numbers other than zero,  $m = -1, 0, 1$ , which also results in final partial waves with different  $m$ -quantum numbers. In principle, these can have different amplitudes and phases and thus increase the number of fitting parameters. Additionally, for the  $p$ -



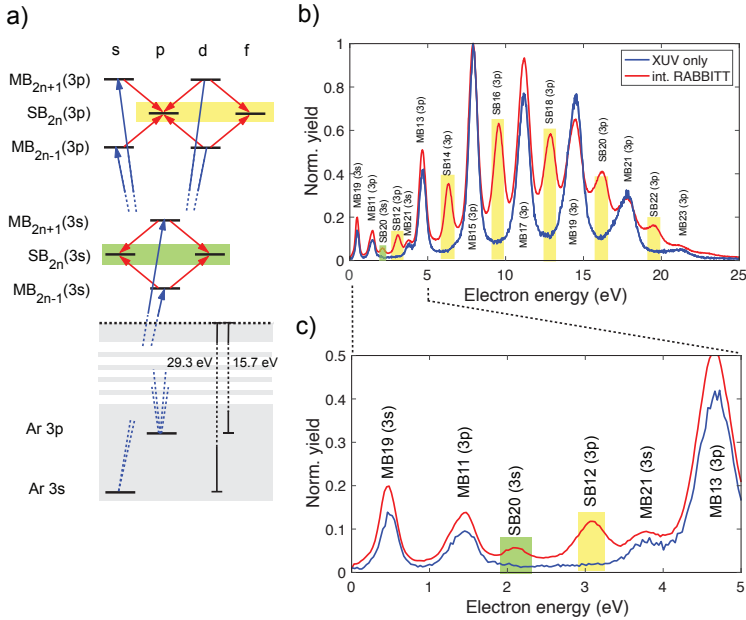


**Figure 4.7:** a) Quantum pathways leading to the same sideband for ionization from Ar 3s and Ar 3p. The XUV (blue) mediates bound to continuum transitions (ionization), the IR (red) mediates transitions within the continuum. All quantum pathways interfere. The sidebands are highlighted in yellow for the 3p-channel and in green for the 3s-channel. b) Experimental XUV-only and integrated RABBITT spectrum. c) Zoom into the spectra of b) in the range from 0 eV - 5 eV.

ground states, the quantum pathways  $p \rightarrow s \rightarrow p$  and  $p \rightarrow d \rightarrow p$  would need to be distinguished and may have different amplitudes and phases, too, further increasing the number of free parameters. For the sum of interference terms of  $p$ - with  $p$ -,  $p$ - with  $f$ -, and  $f$ - with  $f$ -partial waves, the sideband anisotropy parameters  $n = 0, 2, 4, 6$  would be non-zero. Not all fit parameters could be unambiguously retrieved unless an *a priori* assumption is made, e.g., that pathways with different  $m$ -quantum numbers have the same amplitudes and photoionization phases.

Alternatively, the same phase difference as above,  $\varphi_s^{cc+} - \varphi_d^{cc+}$ , can also be retrieved for larger noble gases. The photoionization from  $p$ -ground states is the dominant photoionization channel for the larger noble gases in the here investigated energy regime, however, electrons ionized from

*s*-ground states can be energetically well separated in the photoelectron spectrum. The only constrain is that the energy difference between the ionization thresholds from *p/d* and *s*-ground states does not coincide with a multiple of the employed laser photon energy, as otherwise the SBs (or MBs) from the different channels overlap. Figure 4.7 a shows a schematic of the accessible two-photon quantum pathways in argon. The threshold for ionization from Ar *3p* is 15.7 eV ( $3p_{3/2}$ : 15.7 eV,  $3p_{1/2}$ : 15.9 eV) and the threshold for ionization from Ar *3s* is 29.3 eV, i.e. a difference of 13.6 eV. With the laser wavelength of 785 nm (1.58 eV photon energy), as used in this thesis, the ionization channels can be well separated. Figure 4.7 b and c show the experimental photoelectron spectra for an XUV-only experiment in comparison to a delay integrated RABBITT experiment. The MBs and SBs from the *3p*-channel are slightly broader due to the spin-orbit coupling. The SB positions are highlighted for both channels. For the *3s*-channel, only one SB can be resolved as no higher harmonics are available. The other noble gases are less suited as either the ionization energy of the *s*-ground state is too high (neon) or the bands of the different ionization channels overlap (krypton, xenon) for the here employed laser wavelength.

Figure 4.8 shows the anisotropy parameters of an argon RABBITT. The yellow lines indicate the integration range for SB 20 for the *3s*-channel. Figure 4.9 shows the corresponding simultaneous fit. It can be seen that, in comparison to helium (see Figure 4.3), the integrated SB anisotropy parameters have a significantly different modulation depth. The resulting phase differences  $\varphi_s^{cc\pm} - \varphi_d^{cc\pm}$  are presented in Table 4.2. The phase differences clearly differ from the helium trend (compare to Figures 4.4 and 4.5). In particular, it is remarkable that, in contrast to the helium case, the *cc*-phase differences between the two partial waves are tremendously different for absorption and stimulated emission. This suggests that for argon, the observed phase difference is indeed influenced by other effects, e.g., electron correlation effects and screening, or simply the deviation from the helium short-range potential. However, for a conclusion, further investigations have to be carried out.

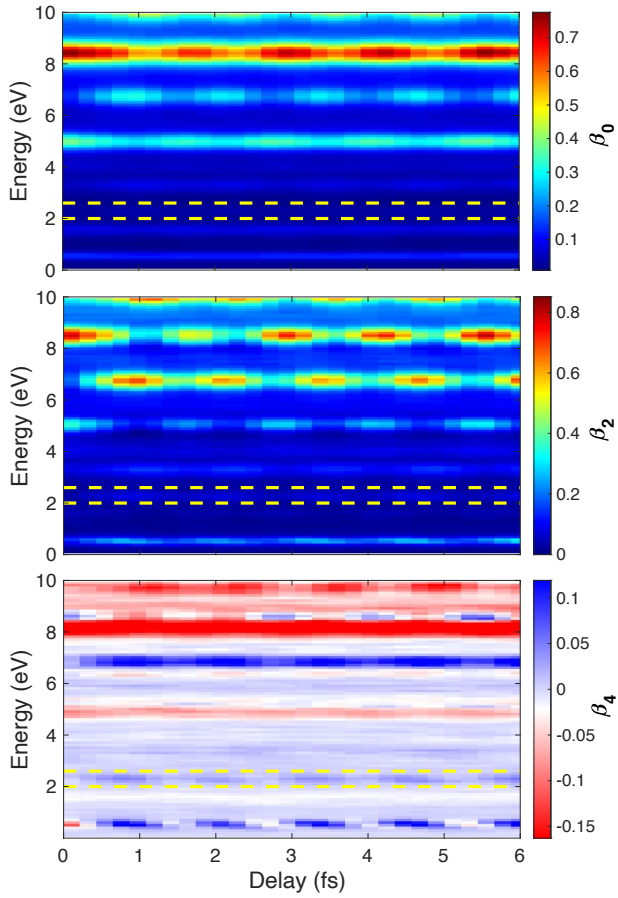


**Figure 4.8:** Experimental anisotropy parameters of the time resolved photoelectron angular distribution in helium,  $\beta_0$  (top),  $\beta_2$  (centre) and  $\beta_4$  (bottom). The yellow lines indicate the integration range of sideband 24, ionized from the  $3s$ -state. A positive delay indicates that the IR pulse is delayed with respect to the XUV.

$E_{Kin}$	2.1 eV
$\varphi_s^{cc+} - \varphi_d^{cc+}$	2.02 rad.
$\varphi_s^{cc-} - \varphi_d^{cc-}$	0.04 rad.

**Table 4.2:** Phase differences between  $s$ - and  $d$ -partial waves induced by the  $cc$ -transitions for SB 20 for ionization from argon  $3s$ .

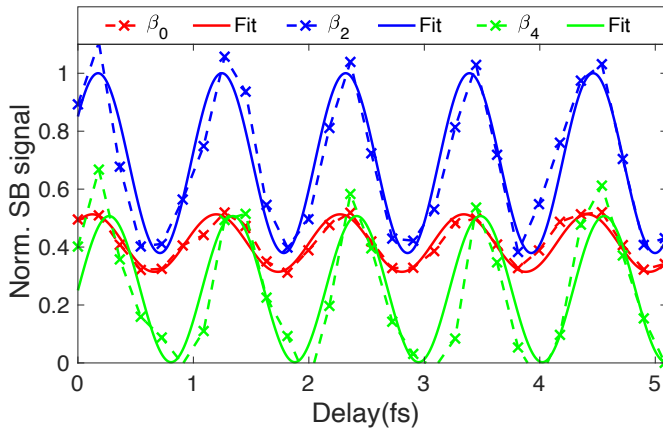


**Figure 4.9:** Simultaneous fit of the anisotropy parameters of argon for SB 20, for ionization from the 3s-state. The time resolved SB anisotropy parameter signals as well as the corresponding simultaneous fit is shown:  $\beta_0$  (red),  $\beta_2$  (blue) and  $\beta_4$  (green).

## 4.5 Outlook

Since its introduction in 2001 [4, 13], the RABBITT scheme experienced great success. However, typically only the SB phases are analyzed. Other information such as the SBs amplitudes, modulation depth, or angular distributions is only seldomly discussed. In this sense, the procedure presented in this chapter completes the RABBITT picture. By combining the amplitude and phase information of the full angular distribution in a unifying fitting procedure, the method, in turn, enables to retrieve the amplitudes and phases of all contributing quantum pathways. From a high-level perspective, making use of the full information about the interferometer also enables one to fully decode the interferometer. The added information grants access to transition ratios or phase differences between different cc-transitions. The ability to disentangle multiple interfering quantum pathways at the same kinetic energy further facilitates the study of more complex atoms or molecules. The presented procedure clearly advances the RABBITT technique. Requiring an angle-resolved detection of the photoelectrons, it, however, also sets higher experimental demands.

## Attosecond interferometry employing overlapping high harmonics

Due to its interferometric nature, the RABBITT-scheme enables precise measurements of photoionization phases. Employing sharp, narrowband high harmonics, corresponding to a long series of attosecond bursts in the underlying pulse train, a sharp and temporally long interferogram is generated, from which the desired phases can be retrieved. However, using narrow high harmonics, only small energy ranges of the target species are probed.

The question arises if such long interferograms are at all needed, and, if also broader high harmonics, which would lead to shorter interferograms, could be used? For technical reasons, in many experiments only short delay ranges are scanned such that shorter interferograms would not even lower the achieved resolution. A few very successful studies employing the so-called *Rainbow* RABBITT technique [85, 86] and broad high harmonics demonstrated the measurements of phase variations within single sidebands. In the publication in this chapter, a novel attosecond interferometric technique employing even broader, overlapping high harmonics is introduced, which makes also use of 1-photon-2-photon-interferences. This technique enables the retrieval of phase differences continuously as a function of energy and across the full energy spectrum of an attosecond pulse train. It does not anymore distinguish between mainbands and sidebands.

The technique is introduced within the publication presented in Section 5.1. Section 5.2 provides a step-by-step derivation of the used analytical expressions. Section 5.3 details the concept of the femtochirp in attosecond pulse trains. Finally, Section 5.4 sketches a method to recover *absolute* phases, before an outlook is presented.

Details about the publication printed in this chapter are listed below. The text and figures are as in the publication. Only the style of the text, figures and equations has been adapted to the style of the thesis. The arrangement of subfigures has been adapted. Further, the numbering of the figures and references has been adjusted. The reference list of the publication has been included in the reference list of the thesis. The mathematical notation is kept as in the original publication and slightly varies from other parts of this thesis.

**Title:** "Towards the complete phase profiling of attosecond wave packets"  
**Journal:** *ArXiv* (in review at Physical Review Research)  
**URL:** <http://arxiv.org/abs/2012.07426>  
**Published:** 14<sup>th</sup> December 2020  
**License:** Non-exclusive distribution License

## 5.1 Towards the complete phase profiling of attosecond wave packets

*Jaco Fuchs*<sup>1,\*</sup>, *Nicolas Douguet*<sup>2,3</sup>, *Stefan Donsa*<sup>4</sup>, *Fernando Martin*<sup>5,6,7</sup>,  
*Joachim Burgdörfer*<sup>4</sup>, *Luca Argenti*<sup>2,8</sup>, *Laura Cattaneo*<sup>1</sup>, *Ursula Keller*<sup>1</sup>

<sup>1</sup> Department of Physics, Eidgenössische Technische Hochschule Zürich, Zürich, Switzerland <sup>2</sup> Department of Physics, University of Central Florida, Orlando, Florida, USA <sup>3</sup> Department of Physics, Kennesaw State University, Marietta, Georgia, USA <sup>4</sup> Institute of Theoretical Physics, Vienna University of Technology, Vienna, Austria, EU <sup>5</sup> Departamento de Química Modulo 13, Universidad Autónoma de Madrid, 28049 Madrid, Spain, EU <sup>6</sup> Condensed Matter Physics Center (IFIMAC), Universidad Autónoma de Madrid, 28049 Madrid, Spain, EU <sup>7</sup> Instituto Madrileño de Estudios Avanzados en Nanociencia (IMDEA-Nano), 28049 Madrid, Spain, EU <sup>8</sup> CREOL, University of Central Florida, Orlando, Florida 32186, USA

\* [jafuchs@phys.ethz.ch](mailto:jafuchs@phys.ethz.ch)

**Realistic attosecond wave packets have complex profiles that, in dispersive conditions, rapidly broaden or split into multiple components. Such behaviors are encoded in sharp features of the wave packet spectral phase. Here, we exploit the quantum beating between one- and two-photon transitions in an attosecond photoionization experiment to measure the photoelectron spectral phase continuously across a broad energy range. Supported by numerical simulations, we demonstrate that this experimental technique is able to reconstruct sharp fine-scale features of the spectral phase, continuously as a function of energy and across the full spectral range of the pulse train, thus beyond the capabilities of existing attosecond spectroscopies. In a proof-of-principle experiment, we retrieve the periodic modulations of the spectral phase of an attosecond pulse train due to the individual chirp of each harmonic.**

Attosecond photoionization time delays provide a precise timing of electronic motion in atoms [6, 52, 59], molecules [38, 58] and solids [5, 41, 42, 87]. Defined as group delay difference between two electron wave packets, they set benchmarks for the most advanced quantum simulations [67, 88, 89]. However, as group delays are given by the first-order expansion of

the spectral phase  $\varphi(E)$ , they cannot characterize the full wave packet evolution. Indeed, dynamical aspects more complex than a simple delay, such as changes in the wavepacket envelope shape, can only be reconstructed if the energy-dependent spectral phase is measured in full. In particular, strong and sharp variations of  $\varphi(E)$  are key to the most intricate wave packet dynamics [52, 85, 90–92].

Most experimental techniques currently used to characterize photoionization phases can only retrieve the average value of the group delay across a broad energy range, e.g., the whole attosecond pulse bandwidth in streaking measurements [6, 28, 37], or at discrete energies spaced by twice the probe frequency, in the RABBITT (reconstruction of attosecond beatings by interference of two-photon transitions) scheme [4, 13]. In these techniques, therefore, rapid phase variations with energy are typically lost. A few interferometric schemes have been proposed to resolve sharp spectral features: by dispersing broad RABBITT sidebands [52, 85, 86], by scanning the probe frequency across the feature [90, 93], or by employing bi-circular attosecond pulse trains [94]. Even these more advanced schemes, however, are sensitive only to the difference of the spectral phase between two isolated harmonics, and hence they can characterize the wave packet profile in more detail only under the ad-hoc assumption that the harmonics are Fourier limited. The question arises, therefore, whether sharp phase variations associated with either the impinging light or the electronic structure of the target can be directly observed.

In this work, we demonstrate that the quantum beat between one- and two-photon transitions, formerly referred to as 1-2 quantum beat [68, 95–97], together with angle-resolved electron spectroscopy, provides direct access to complex structures in the spectral phase of the photoionized electron wave packets, which, to the best of our knowledge, are inaccessible to any other attosecond spectroscopy method. In contrast to the previous methods [68, 95–97], we enable the 1-2 quantum beat by performing a RABBITT-inspired experiment using an extreme ultraviolet (XUV) attosecond pulse train (APT) with only odd, but spectrally broad, high harmonics. The combination of the 1-2 quantum beat with spectrally broad high harmonics allows us to retrieve phase differences continuously as a function of energy and across the entire bandwidth of the XUV spectrum,



i.e., it allows for a complete phase profiling. In a proof-of-principle experiment, we observe periodic oscillations in the phase of electron wave packets generated by photoionization from helium. Supported by numerical solutions of the time-dependent Schrödinger equation (TDSE), we can attribute these phase oscillations to the harmonic chirp of the XUV pulse train inherent to the underlying high harmonic generation (HHG) process. Whereas the harmonic chirp has been successfully quantified for single harmonics [98–103], the direct observation of the underlying phase modulations across the full spectrum, originally predicted more than 15 years ago [104, 105], has not been possible so far.

The spectral phase of a photoelectron wave packet created by absorption of one XUV photon comprises two contributions, the Eisenbud-Wigner-Smith (EWS) scattering phase due to half-scattering at the ionic potential [31, 32] and the spectral phase of the ionizing light pulse. The spectral phase of photo-emitted electrons, therefore, can either be used to study the EWS scattering phase [30, 106] or to characterize XUV light pulses [18, 107]. Fig. 5.1a illustrates the comparison between the RABBITT and the 1-2-quantum beat method described in this letter. Upon XUV photoionization (pump) an IR pulse (probe) promotes continuum-continuum (cc) transitions [29, 55]. As the pump-probe delay is varied, the photoelectron signal beats as a result of the interference between quantum pathways with the same final energy. The phase of this beating is directly linked to the spectral phase difference between the two interfering quantum paths. Whereas RABBITT is based on the interference between two different two-photon pathways, i.e., a 2-2-quantum beat, the 1-2 quantum beat method exploits the interference between one-photon and two-photon pathways.

To illustrate the different sensitivity of the two approaches to sharp features in the spectral phase, we first consider an idealized ionization experiment for which we assume that in the energy regime of interest, the atomic ionization cross-section is constant and the EWS and cc-phases are negligible. Under these assumptions, the phase of the ionized electron wave packet directly reflects the phase of the XUV spectrum. The XUV spectrum (Fig. 5.1b) used in the calculation features a strong and well-localized spectral phase variation at its center that may mimic the effect of a complex high-harmonic generation process or the resonant ionization

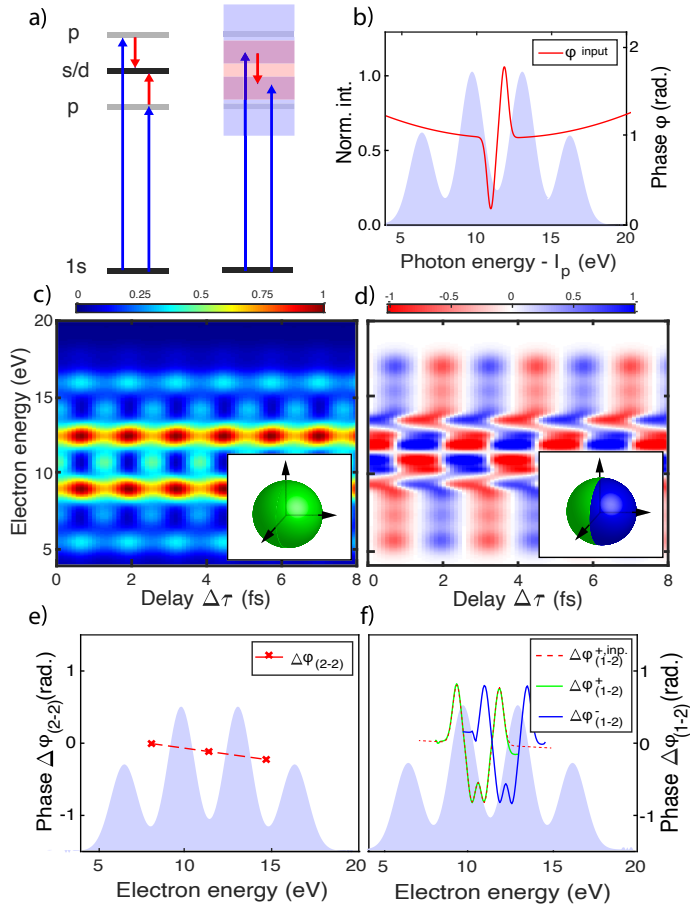


**Figure 5.1:** a) RABBITT (2-2 quantum beat) and the 1-2-quantum beat protocol, schematically. Blue arrows indicate photoionization induced by the XUV and red arrows indicate c-transitions induced by the IR. b) Amplitude and phase of the input XUV pulse. c) RABBITT trace (total yield). The inset indicates the integration over all emission angles. d) Asymmetry trace extracted from the 1-2 quantum beat. The inset indicates the asymmetry of the angular distribution (difference left-right). e) Phase difference  $\Delta\varphi_{(2-2)}(E)$  extracted from the RABBITT sidebands. f) Phase differences  $\Delta\varphi_{(1-2)}^{+}(E)$  and  $\Delta\varphi_{(1-2)}^{-}(E)$  extracted from the 1-2 quantum beat method and comparison with  $\Delta\varphi_{(1-2)}^{+,imp.}(E)$  from the input phase.

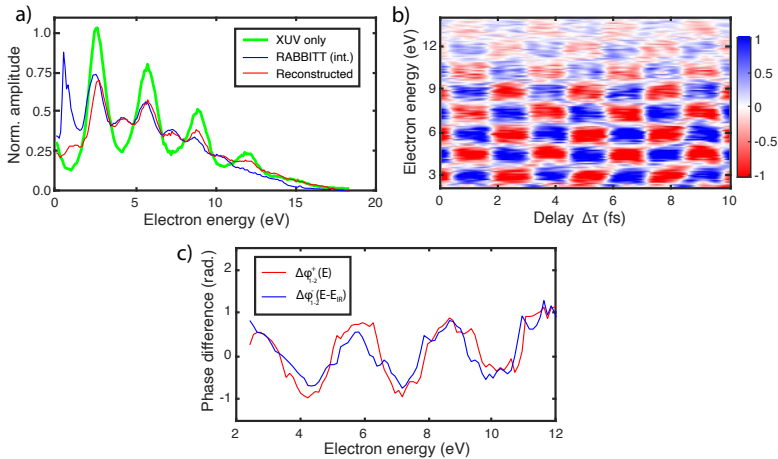


**Figure 5.2:** a) XUV-only (green) and delay-integrated RABBITT spectrum (blue) from the experiment. The red curve results from the fit of the transition rates (Eq. 5.7) to the integrated RABBITT spectrum in the range from 3 eV to 12 eV. b) Measured asymmetry signal, defined as in Eq. (5.3), as a function of pump-probe delay. c). Retrieved phases  $\Delta\varphi_{1-2}^+(E)$  and  $\Delta\varphi_{1-2}^-(E - \hbar\omega_{IR})$  from the experiment.

phase of the target. As can be seen in Fig. 5.1c,e, RABBITT is blind to the sharp phase variation, while the 1-2 quantum beat is particularly sensitive to it (Fig. 5.1d,f). The retrieved phase differences provide detailed information on the spectral phase  $\varphi(E)$  well beyond its first derivative at the center, as we will show below.

The XUV-APT spectrum is composed of odd high harmonics of an IR laser field, which result in mainbands (MBs) (one-photon-transitions) in the photoelectron spectrum, separated by twice the IR photon energy  $\hbar\omega_{IR}$ . Interaction with the IR probe leads to the appearance of sidebands (SB) between the mainbands, whose intensities oscillate as a function of the pump-probe delay  $\tau$  at twice the IR laser frequency  $2\omega_{IR}$  (Fig. 5.1c). The beating is symmetric along the common light polarization axis as only partial waves with the same parity interfere. The phase offset of each sideband corresponds to the phase difference between the neighboring harmonics extracted by RABBITT  $\Delta\varphi_{2-2} = \varphi(E + \hbar\omega_{IR}) - \varphi(E - \hbar\omega_{IR})$ . Since this phase difference can only be sampled at the sideband positions, the sharply structured phase profile remains undetected (Fig. 5.1e), even

through the XUV spectrum spans the entire energy region.

In the 1-2 quantum beat method, by contrast, the interference of partial waves with opposite parity ( $s - p$  or  $p - d$ ) gives rise to an asymmetry of the electron angular distribution that beats at the angular frequency  $\omega_{\text{IR}}$  as a function of  $\tau$  (Fig. 5.1 d) [68, 95]. This asymmetry, determined here by the difference of electron yield emitted to opposite sides of the plane perpendicular to the light polarization, is shown in Fig. 5.1 d. For the ultrashort APT employed here, both two-photon pathways (absorption and stimulated emission of an IR photon) can interfere with the one-photon amplitude across the whole spectral width of the APT. As long as the harmonics are spectrally sufficiently broad, therefore, the two phase differences  $\Delta\varphi_{1-2}^+(E) = \varphi(E - \hbar\omega_{\text{IR}}) - \varphi(E)$  and  $\Delta\varphi_{1-2}^-(E) = \varphi(E) - \varphi(E + \hbar\omega_{\text{IR}})$  can both be retrieved continuously as a function of energy and the sharp phase profile is detected. As we will show below, the two phase differences can be retrieved fully analytically from the asymmetry trace. Furthermore, as the one-photon pathway is itself part of the interference, the retrieved phases are unaffected by the finite spectral bandwidth of the IR [86]. For sharp resonances (see, e.g., Fig. 5.1), the 2-photon pathways serve as flat reference, such that the retrieved phases remain sharp.

The angle-dependent ionization probability is [52]

$$I(E, \vartheta, \tau) = \left| \sum_{\ell} (A_{\ell}^+ + A_{\ell}^-) Y_{\ell}^0(\vartheta) + i A_1^1 Y_1^0(\vartheta) \right|^2, \quad (5.1)$$

where  $A_1^{\pm}$  and  $A_{\ell}^{\pm}$  are the one-photon and two-photon amplitudes (+/- designates IR absorption / emission, and  $\ell = 0, 2$  is the photoelectron orbital angular momentum),  $Y_{\ell}^m$  are spherical harmonics with  $m = 0$  due to the collinear alignment of the employed light fields, and  $\vartheta$  is the angle between the electron photoemission direction and the common light polarization axis. The one- and two-photon amplitudes of the quantum pathways are functions of the kinetic energy  $E$  and of the pump-probe delay  $\tau$  [29],

$$A_1^{\pm} = |A_1^{\pm}| e^{i\varphi(E)}, \quad A_{\ell}^{\pm} = |A_{\ell}^{\pm}| e^{i(\varphi_{\ell}^{\pm}(E) \pm \omega\tau)}. \quad (5.2)$$

The spectral phase of the one-photon XUV ionization  $\varphi(E) = \varphi_{\ell=1}^1(E)$  contains the EWS scattering phase and the XUV phase. The photoelectron

asymmetry signal

$$f_a(E, \tau) = I(E, \tau)_{\theta \leq 90^\circ} - I(E, \tau)_{\theta \geq 90^\circ}, \quad (5.3)$$

given by the difference between emission into the forward and backward hemispheres, then follows as

$$f_a(E, \tau) = \sum_{\sigma, \ell} \sigma c_\ell \left| A_1^1 \right| \left| A_\ell^\sigma \right| \sin \left[ \omega\tau + \sigma \left( \varphi_\ell^\sigma(E) - \varphi_1^1(E) \right) \right], \quad (5.4)$$

where  $\sigma = \pm$ ,  $c_0 = \sqrt{3}$  and  $c_2 = \sqrt{15}/4$ . For a simplified analytic estimate, the two-photon pathways can be approximated by the one-photon phase as  $\varphi_\ell^\sigma(E) \simeq \varphi_1^1(E - \sigma\hbar\omega_{\text{IR}})$  since the method is sensitive only to phase variations but not to absolute phases. The cc-phase for different angular momenta [55] can be neglected since its variation is small within the present energy range. Likewise, the cc-transition probabilities to different  $\ell$  are only weakly energy and  $\ell$  dependent, such that  $|A_\ell^\sigma| \approx |A^\pm|$  [53]. Consequently,

$$f_a(E, \tau) \simeq A(E) \sin[\omega\tau + \delta(E)], \quad (5.5)$$

where  $A(E)$  and  $\delta(E)$  are the modulus and phase of  $a^+ e^{i\Delta\varphi_{1-2}^+} - a^- e^{i\Delta\varphi_{1-2}^-}$ , with  $a^\sigma(E) = |A_1^1| |A^\sigma| (c_0 + c_2)$  and  $\Delta\varphi_{1-2}^\sigma(E) = \sigma(\varphi(E - \sigma\hbar\omega_{\text{IR}}) - \varphi(E))$ . This approximate relationship (Eq. (5.5)) illustrates the sensitivity of the 1-2 quantum beat method to rapid variations of the spectral phase. For energy-independent phases,  $A(E)$  vanishes, as  $a^+(E) \approx a^-(E)$ . By contrast, phase differences  $\Delta\varphi^\pm$  that vary rapidly within  $\hbar\omega_{\text{IR}}$  result in strong oscillations of the photoemission asymmetry.

Fig. 5.2 shows the results of a proof-of-principle experiment performed with atomic helium. The experiment is carried out resembling the RABBITT protocol and using an XUV-APT with spectrally broad high harmonics. The XUV-APT is generated via HHG using a 10 fs FWHM IR laser pulse centered around 785 nm from a carrier-envelope-phase (CEP) stabilized Ti:sapphire laser system. The CEP stabilization is essential for the observation of the asymmetry signal. Otherwise, an asymmetry would not be observable at all. The XUV-APT is focused together with a collinear time-delayed replica of the generating IR pulse on a cold helium gas jet. The resulting photoelectrons are collected with a cold target recoil ion

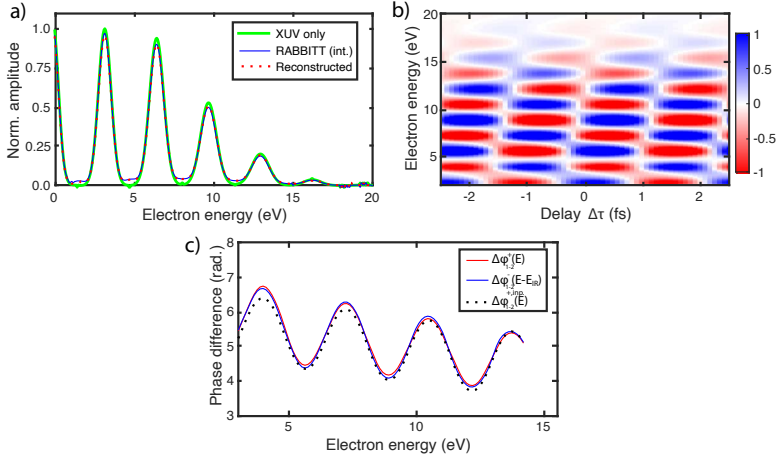


**Figure 5.3:** a) XUV-only (green) and delay-integrated RABBITT spectrum (blue) from the quantum simulation employing a single-active electron (SAE) approximation and a model potential from [72]. The red curve results from a fit of the transition rates (Eq. (5.7)) to the integrated RABBITT spectrum in the range from 2 eV to 14 eV. b) Calculated asymmetry signal, defined as in Eq. (5.3), as a function of pump-probe delay. c) Retrieved phases  $\Delta\varphi_{1-2}^+(E)$  (red) and  $\Delta\varphi_{1-2}^-(E - \hbar\omega_{IR})$  (blue) in comparison to  $\Delta\varphi_{1-2}^{+inp.}(E)$  from the input phase.

momentum spectrometer (COLTRIMS) [50], which allows for an angular resolved detection [51]. The setup is described in details in [48]. In the delay-integrated RABBITT spectrum, the MBs are depleted as compared to the XUV-only spectrum due to the IR induced cc-transitions to the SBs (Fig. 5.2a). The asymmetry shows a checkerboard pattern (Fig. 5.2b), which implies a characteristic energy dependence of the spectral phase. If the phase were spectrally flat, only a weak and constant asymmetry signal comparable to the upper (or lower) part in Fig. 5.1d would be expected. A similar checkerboard has been observed in recent experiments exploiting the 1-2-quantum beat, where both even and odd harmonics [68, 95] have been employed, revealing a non-flat phase behavior, as well.

The retrieval of the phase differences  $\Delta\varphi_{1-2}^\pm$  from the asymmetry comprises three steps. First, we determine the modulus of the one-photon amplitude  $|A_1^1(E)| = \sqrt{f_{tot}^{XUV}(E)}$  from an XUV-only spectrum. Second, the modulus of the two-photon amplitudes for absorption and emission  $|A^\pm|$  are determined by fitting the IR-transitions rates to the delay-integrated

RABBITT spectrum (Fig. 5.2a). The amplitudes of the two-photon pathways are replicas of the one-photon amplitudes, shifted by the IR photon energy:

$$A^+(E) = r^+(E)A_1^1(E - \hbar\omega_{\text{IR}}) \quad (5.6)$$

$$A^-(E) = r^-(E)A_1^1(E + \hbar\omega_{\text{IR}}), \quad (5.7)$$

with  $r^\pm(E) = c^\pm + d^\pm E$ . The parameters  $c^\pm$  and  $d^\pm$  account for a smooth energy dependence of the cc-transition rates and are fitted to the delay-integrated RABBITT spectrum (see SM),

$$\langle f_{\text{tot}}(E, \tau) \rangle_\tau = |A^1(E)|^2 + 2|A^+(E)|^2 + 2|A^-(E)|^2. \quad (5.8)$$

Finally, using  $a^+(E)$  and  $a^-(E)$ , we can analytically determine  $\Delta\varphi_{1-2}^\pm(E)$  from the measured amplitude  $A(E)$  and phase  $\delta(E)$  of the asymmetry signal as continuous function of the energy via Eq. (5.5) (see SM). We note that for ionization from other than  $s$ -ground states, the parametrization of the angular dependent ionization amplitude must be extended to account for partial waves with different  $l$ - and  $m$ -quantum numbers. For the procedure to be consistent, the retrieved phase differences must satisfy the identity  $\Delta\varphi_{1-2}^+(E) = \Delta\varphi_{1-2}^-(E - \hbar\omega_{\text{IR}})$ . Figure 5.2c shows that  $\Delta\varphi_{1-2}^+(E)$  and  $\Delta\varphi_{1-2}^-(E - \hbar\omega_{\text{IR}})$  are indeed in close agreement with each other across a wide energy range, demonstrating the applicability of the phase retrieval. The deviation of the two phases for energies slightly above 6 eV and 9 eV indicates a larger uncertainty for these energies.

The retrieved phase differences from the 1-2 quantum beat method exhibit periodic oscillations with the same periodicity as the XUV harmonics. Since in this energy region neither the EWS scattering phase nor the cc-phase of atomic helium oscillates, the phase oscillations can be attributed to the ionizing APT. To support this hypothesis, we simulate the experiment by solving the TDSE in the single-active-electron (SAE) approximation [71]. We have checked for several delay steps that a full 2-electron calculation [75, 108] yields indistinguishable results. As input we use an XUV pulse featuring spectral phase oscillations. As expected, we obtain an asymmetry signal exhibiting a qualitatively similar checkerboard pattern (Fig. 5.3b). The tilt observed in the pattern is due to the attochirp of the pulse. We further verify the retrieval method by applying it to

the simulated data and comparing the result to the original XUV phase. Figure 5.3c shows the excellent agreement between the phase difference  $\Delta\varphi_{1-2}^{+,inp.}$  from the input phase and the retrieved phase differences  $\Delta\varphi_{1-2}^+$  and  $\Delta\varphi_{1-2}^-$ . The small deviation of the latter two across the full energy range indicates the accurate phase retrieval for all energies. The slight deviation with respect to the input phase at low kinetic energies is due to the EWS and IR-induced cc-phase (see approximations in Eq. (5.5)), which are no longer negligible at these energies and cannot be separated from the XUV phase by the retrieval method.

The 1-2 quantum beat method enables the measurement of phase variations across an individual harmonic. This is fundamentally different from measuring phase differences between the same spectral region of different harmonics. Therefore, this method gives us the unprecedented ability to simultaneously measure the atto- and the femtochirp of the APT inherent to the HHG process [104]. The attochirp, which corresponds to a linear increase (or decrease) of the group delay across the full spectrum, is encoded in the slope of the mean of  $\Delta\varphi_{1-2}^{\pm}(E)$ . In the time domain, the attochirp translates into different harmonics being emitted at different times during the IR cycle, stretching each attosecond burst.

The femtochirp corresponds to the observed oscillations of  $\Delta\varphi_{1-2}^{\pm}(E)$ . Such a rapidly varying phase within a given harmonic in the plateau region was originally predicted more than 15 years ago [104]. The femtochirp results from the interplay of two microscopic effects. First, the phase of each harmonic depends on the IR intensity at the time of tunnel ionization [109]. The use of ultrashort pulsed light sources to drive HHG implies a rapidly varying intensity envelope, which results in fine-scale phase structures within each harmonic. Second, several quantum paths contribute, in general, to the generation of the harmonics in the plateau region. Even though the intensity dependence of the phase for each path is approximately linear, the superposition of multiple paths with different phase drifts leads to a complex phase structure within each harmonic [110]. Both effects, therefore, can give rise to a femtochirp, which, in the time domain, results in an unequal spacing of the attosecond bursts [104] and stretches the envelope of the pulse train, see Fig. 5.4. As the multi-quantum-path interference is sensitive to and easily suppressed by



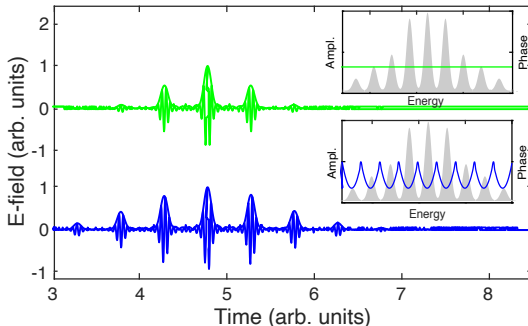


**Figure 5.4:** Comparison of an APT with periodic oscillations of the spectral phase (blue) and an APT with a flat phase (green). The spectrum is identical for both APTs. The insets show the spectrum and the corresponding phase for both APTs.

macroscopic propagation effects, we expect the intensity envelope effect to be the dominant contribution under realistic experimental conditions.

In conclusion, we have shown that the 1-2 quantum beat method can be used to retrieve phase variations of a photoelectron wave packet as a continuous function of energy, with a finer energy resolution than the probe frequency spectral width. In particular, we demonstrate with a proof-of-principle experiment that the 1-2-quantum beat method allows us to observe the strong periodic modulations of the spectral phase due to the harmonic chirp and caused by the HHG process itself. Despite the harmonic chirp being an already well-established concept [98–103], such phase modulations could not have been observed so far, since they are inherently inaccessible to any pump-probe scheme that relies on the comparison of the phase of consecutive harmonics such as RABBITT or related techniques [68, 94, 96, 111]. As the retrieval method returns phase differences as a continuous function of energy and is given in closed form, it constitutes a valuable tool to investigate even more complex photoionization dynamics and provides unprecedented access to the spectral phase of wave packets resulting from the break-up of quantum systems.

**Acknowledgements.** All authors acknowledge the COST Action CA18222 (Attosecond Chemistry). J.F., L.C. and U.K. acknowledge the support of the NCCR MUST, funded by the Swiss National Science Foundation. L.A. and N.D. acknowledge the support of the United States National Science

Foundation under NSF Grant No. PHY-1607588 and by the UCF in-house OR Grant Acc. No. 24089045. Parts of the calculations were performed on the Vienna Scientific Cluster (VSC3). S.D. and J.B. acknowledge the support by the WWTF through Project No. MA14-002, and the FWF through Projects No. FWF-SFB041-VICOM, and No. FWF-W1243-Solids4Fun, as well as the IMPRS-APS. F.M. acknowledges the MICINN projects PID2019-105458RB-I00, the 'Severo Ochoa' Programme for Centres of Excellence in R&D (SEV-2016-0686) and the 'María de Maeztu' Programme for Units of Excellence in R&D (CEX2018-000805-M).

### 5.1.1 Supplemental material

#### A. Characterization of the cc-transition rates

To characterize the cc-transition rates, we compare the results of numerically calculated photoelectron spectra (PES) in helium for three different cases: (1) one narrow XUV harmonic in the absence of the IR. (2) The same XUV harmonic plus an IR field with intensity  $1 \cdot 10^{11} \text{W/cm}^2$ . (3) The same XUV harmonic plus an IR field with intensity  $2 \cdot 10^{11} \text{W/cm}^2$ . The calculations are performed using the single-active electron (SAE) approximation and the model potential from [72]. We have verified that full 2-electron simulations give nearly identical results. Since the amplitude of the IR field is constant across a time interval wider than the APT duration, and the target does not exhibit any resonance in the spectral region of interest, the results are the same as for a purely monochromatic IR light. In particular, to the lowest perturbative order, there is no quantum path interference and the resulting PES does not depend on the XUV-IR delay. We integrate the resulting total yield for the XUV-only simulation and the two-photon peaks for the two-color simulations. Fig. 5.5 shows the two-color PES for an XUV energy of 35 eV and IR intensity of  $2 \cdot 10^{11} \text{W/cm}^2$ . The two-photon peaks are well separated from the one-photon peak.

The modulus of the one-photon and two-photon-amplitudes can be obtained by taking the square root of the corresponding one-photon and two-photon yields, respectively. The cc-transition rates for absorption (emission) are then calculated by dividing the higher (lower) two-photon probability by the one-photon probability. The calculation is repeated for

all XUV energies from 24.5 eV to 40 eV in steps of 0.5 eV. Fig. 5.6 shows the transition rates as a function of the energy, justifying the assumption of linear transition rates (Eq. (5.6) and (5.7)).

As can be seen from the comparison between the transitions rates from different IR-intensities, the transition rates for both absorption and emission scale with the square root of the IR intensity, in line with the fact that the two-photon amplitude is proportional to the electric field strength.

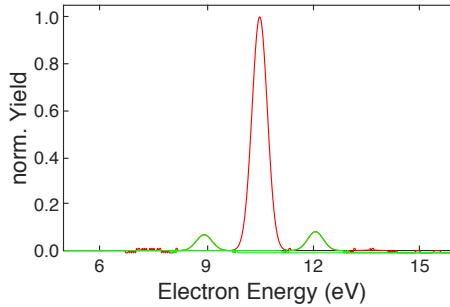


**Figure 5.5:** Photoelectron yield from the SAE simulation for helium for the two-color case with an XUV energy of 35 eV and IR intensity of  $2 \cdot 10^{11} \text{ W/cm}^2$ . The side peaks (green) correspond to the two-photon transitions for additional absorption or emission of one IR photon.

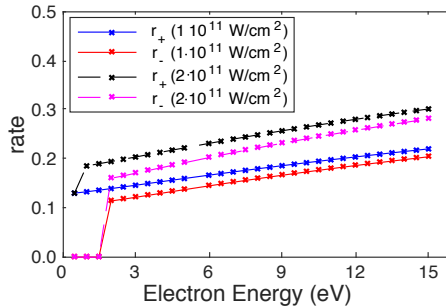


**Figure 5.6:** Transition rates for the IR induced cc-transitions as a function of energy for additional absorption and emission of an IR photon and for different intensities of the IR field ( $10^{11} \text{ W/cm}^2$  and  $2 \cdot 10^{11} \text{ W/cm}^2$ ). The transitions rates for the higher intensity case are  $\sqrt{2}$  higher compared to the weak intensity case as they scale with the strength of the electric field.

## B. Total photoelectron yield

The total photoelectron signal is determined by integration of Eq. (5.1) over all emission angles and thus reads

$$\begin{aligned}
 f_{tot}(E, \tau) &= \int_0^{2\pi} \int_0^\pi I(E, \vartheta, \tau) \sin(\vartheta) d\vartheta d\varphi \\
 &= |A^1(E)|^2 + \sum_{\ell=s,d} [|A_\ell^+(E)|^2 + |A_\ell^-(E)|^2 \\
 &\quad + 2|A_\ell^+(E)||A_\ell^-(E)| \cos(2\omega\tau + \varphi_\ell^+ - \varphi_\ell^-)] \\
 &\approx |A^1(E)|^2 + 2|A^+(E)|^2 + 2|A^-(E)|^2 \\
 &\quad + 4|A^+(E)||A^-(E)| \cos(2\omega\tau + \varphi^+ - \varphi^-).
 \end{aligned}$$

The photoelectron spectrum corresponds to the  $2\omega_{\text{IR}}$ -RABBITT signal. [29]. When the delay is integrated over a full IR cycle, the cosine term vanishes.

## C. Solution for the ionization phase

The modulus  $A(E)$  and the phase  $\delta(E)$  of the  $\omega_{\text{IR}}$  oscillation amplitude are obtained via Fourier-transform of the experimental asymmetry signal. The quantities  $a^+(E)$  and  $a^-(E)$  (compare with Eq. (5.5) in the main text) are obtained by fitting the transition rates to the integrated PES. From the two equations

$$\begin{aligned}
 A(E) &= |a^+ e^{i\Delta\varphi_{1-2}^+} - a^- e^{i\Delta\varphi_{1-2}^-}|, \\
 \delta(E) &= \arg(a^+ e^{i\Delta\varphi_{1-2}^+} - a^- e^{i\Delta\varphi_{1-2}^-}),
 \end{aligned}$$

it is possible to retrieve  $\Delta\varphi_{1-2}^\pm(E)$  analytically. Let  $\chi = \Delta\varphi_{1-2}^- - \Delta\varphi_{1-2}^+$ , then

$$A^2(E) = a^{+2} + a^{-2} - 2a^+ a^- \cos \chi,$$

which can be solved for  $\chi$  as

$$\chi = \pm \arccos \left( \frac{A^2 - a^{+2} - a^{-2}}{2a^+ a^-} \right).$$

The correct sign determination for  $\chi$  is ascertained *a posteriori* by requiring the constraint  $\Delta\varphi_{1-2}^+(E) = \Delta\varphi_{1-2}^-(E - E_0)$  to be satisfied for consistency.

From the value of  $\chi$  and the expression for  $\delta(E)$ , it is straightforward to retrieve the two phases  $\Delta\varphi_{1-2}^{\pm}$  as

$$\begin{aligned}\Delta\varphi_{1-2}^+ &= \delta(E) - \arg(a^+ - a^- e^{i\chi}), \\ \Delta\varphi_{1-2}^- &= \chi + \Delta\varphi_{1-2}^+.\end{aligned}$$

This solution holds for all energies, so that the phase differences  $\Delta\varphi_{1-2}^{\pm}$  can be retrieved across the full spectrum.

### Author contributions

J.F led the study, U.K. supervised the study. J.F and L.C conducted the experiments. J.F. analyzed the experiments and developed the retrieval procedure. N.D. and L.A. performed the SAE calculations. S.D. and J.B. performed the *ab-initio* calculations. All authors were involved in the interpretation and contributed to the final manuscript.

## 5.2 Detailed derivation of the angle-resolved spectra

In Section 5.1 the derivation of the  $1\omega$ -oscillation of the photoelectron asymmetry (Eq. (5.5)) is sketched only briefly. This section shall provide a step-by-step derivation.

The angle dependent ionization probability (Eq. (5.1)) reads explicitly

$$\begin{aligned}I(E, \vartheta, \tau) &= \left| \sum_{\ell} (A_{\ell}^+ + A_{\ell}^-) Y_{\ell}^0(\vartheta) + iA_1^1 Y_1^0(\vartheta) \right|^2 \\ &= [|A_0^+|^2 + |A_0^-|^2 + A_0^+ A_0^{-*} + c.c.] Y_0^0(\vartheta)^2 \\ &\quad + |A_1^1|^2 Y_1^0(\vartheta)^2 \\ &\quad + [|A_2^+|^2 + |A_2^-|^2 + A_2^+ A_2^{-*} + c.c.] Y_2^0(\vartheta)^2 \\ &\quad + [A_0^+ A_2^{1*} + c.c. + A_0^- A_2^{1*} + c.c. \\ &\quad\quad + A_0^+ A_2^{-*} + c.c. + A_2^+ A_0^{-*} + c.c.] Y_0^0(\vartheta) Y_2^0(\vartheta) \\ &\quad + [(A_0^+ + A_0^-) A_1^{1*} + c.c.] Y_0^0(\vartheta) Y_1^0(\vartheta) \\ &\quad + [(A_2^+ + A_2^-) A_1^{1*} + c.c.] Y_2^0(\vartheta) Y_1^0(\vartheta).\end{aligned}\tag{5.9}$$

It can be seen easily that only the last two lines lead to an asymmetry in the angular distribution, as here products of spherical harmonics with

different parity appear. The other terms, instead, manifest in a symmetric alternation of the photoelectron yield, or respectively, in an alternation of the total photoelectron yield. The photoelectron asymmetry follows as

$$\begin{aligned}
 f_a(E, \tau) &= I(E, \tau)_{\vartheta \leq 90^\circ} - I(E, \tau)_{\vartheta \geq 90^\circ} \\
 &= \int_0^{2\pi} \int_0^\pi I(E, \vartheta, \tau) \operatorname{sgn}(\vartheta - \pi/2) \sin(\vartheta) d\vartheta d\varphi \\
 &= [-i(A_0^+ + A_0^-)A_1^{1*} + c.c.] \\
 &\quad \int_0^{2\pi} \int_0^\pi Y_0^0(\vartheta)Y_1^0(\vartheta) \operatorname{sgn}(\vartheta - \pi/2) \sin(\vartheta) d\vartheta d\varphi \quad (5.10) \\
 &\quad + [-i(A_2^+ + A_2^-)A_1^{1*} + c.c.] \\
 &\quad \int_0^{2\pi} \int_0^\pi Y_1^0(\vartheta)Y_2^0(\vartheta) \operatorname{sgn}(\vartheta - \pi/2) \sin(\vartheta) d\vartheta d\varphi.
 \end{aligned}$$

Here,  $\operatorname{sgn}(x) = x/|x|$  is the sign-function. The other, symmetric terms vanish. For those the integrand becomes antisymmetric with respect to  $\pi/2$  due to the sign-function and, hence, the integral becomes zero. The two remaining integrals can be determined analytically. Using Equation (5.2) it follows

$$\begin{aligned}
 f_a(E, \tau) &= \sqrt{3}[-i|A_0^+||A_1^1|e^{i(\varphi_0^+ - \varphi_1^1 + \omega\tau)} + c.c. + |A_0^-||A_1^1|e^{i(\varphi_0^- - \varphi_1^1 - \omega\tau)}] \\
 &\quad + \frac{\sqrt{15}}{4}[-i|A_2^+||A_1^1|e^{i(\varphi_2^+ - \varphi_1^1 + \omega\tau)} + c.c. + |A_2^-||A_1^1|e^{i(\varphi_2^- - \varphi_1^1 - \omega\tau)}] \\
 &= 2\sqrt{3}[|A_0^+||A_1^1| \sin(\varphi_0^+ - \varphi_1^1 + \omega\tau) + |A_0^-||A_1^1| \sin(\varphi_0^- - \varphi_1^1 - \omega\tau)] \\
 &\quad + 2\frac{\sqrt{15}}{4}[|A_2^+||A_1^1| \sin(\varphi_2^+ - \varphi_1^1 + \omega\tau) + |A_2^-||A_1^1| \sin(\varphi_2^- - \varphi_1^1 - \omega\tau)]. \quad (5.11)
 \end{aligned}$$

Using  $\sin(x) = -\sin(-x)$  one obtains Equation (5.4). In the last step one can now use the approximation described after Eq. (5.4), i.e.  $\varphi_\ell^\pm(E) \simeq \varphi(E \mp \hbar\omega)$  and  $|A_\ell^\sigma| \approx |A^\pm|$ . Using

$$a_+ = |A_1^1| |A^+| (c_0 + c_2), \quad (5.12)$$

$$a_- = |A_1^1| |A^-| (c_0 + c_2), \quad (5.13)$$

with  $c_0 = 2\sqrt{3}$  and  $c_2 = 2\sqrt{15}/4$  one can then write

$$\begin{aligned} f_a(E, \tau) &= a_+ \sin(\omega\tau + \varphi(E - \hbar\omega) - \varphi(E)) \\ &\quad - a_- \sin(\omega\tau - \varphi(E + \hbar\omega) + \varphi(E)) \\ &= A(E) \sin(\omega\tau + \delta(E)), \end{aligned} \quad (5.14)$$

where  $A(E)$  and  $\delta(E)$  are the modulus and phase of  $a_+ e^{i\Delta\varphi(E - \hbar\omega)} - a_- e^{i\Delta\varphi(E + \hbar\omega)}$ , giving Equation (5.5).

### 5.3 Atto- and femtochirp in attosecond pulse trains

The time-domain representation of an APT can be analytically determined from the high-harmonic spectrum if both the spectral envelope as well as the harmonics are considered Gaussian functions. Particularly, if each harmonic is considered to have the same spectral width  $\Delta f_{har}$  (half-width at  $1/e^{0.5}$ ) the spectrum can be analytically described by the convolution of a narrow Gaussian  $g_{har}(f)$  (harmonics) with a delta comb  $\delta\delta_{f_{rep}}(f)$ , multiplied by a broader Gaussian  $g_{env}$  (spectral envelope) with a half  $1/e$ -width of  $\Delta f_{env}$ .

$$\delta\delta_{f_{rep}}(f) = \sum_k \delta(f - f_{rep} \cdot k), \quad (5.15)$$

$$g_{har}(f) = e^{-\frac{1}{2} \left( \frac{f}{\Delta f_{har}} \right)^2} \cdot e^{i \cdot c_{har} f^2}, \quad (5.16)$$

$$g_{env}(f) = e^{-\frac{1}{2} \left( \frac{f}{\Delta f_{env}} \right)^2} \cdot e^{i \cdot c_{atto} f^2}, \quad (5.17)$$

$$A_{APT}(f) = (\delta\delta_{f_{rep}}(f) \circ g_{har}(f)) \cdot g_{env}(f). \quad (5.18)$$

Here  $\circ$  describes the convolution and  $f_{rep}$  is the frequency separation between two consecutive harmonics, also corresponding to the repetition rate of the pulse train in the time domain. We further allow the harmonics to have a quadratic phase term corresponding to a harmonic chirp, depending on the second-order chirp coefficient  $c_{har}$ . Due to the convolution of the harmonic with the delta-comb, the quadratic phase leads to an oscillating spectral phase across the entire APT spectrum. Similarly, we allow the Gaussian envelope to have a quadratic phase with a second-order chirp parameter  $c_{atto}$  which corresponds to an attochirp. We note

that the bandwidth of the envelope is much broader than the bandwidth of a single harmonic, i.e.  $\Delta f_{env} > \Delta f_{harm}$ .

One can now inspect the effect of the harmonic chirp and the attochirp on the APT in the time domain via Fourier transform.

$$\begin{aligned}
 A_{APT}(t) &= \mathcal{F}[A_{APT}(f)] \\
 &= \mathcal{F}[(\delta\delta_{f_{rep}}(f) \circ g_{har}(f)) \cdot g_{env}(f)] \\
 &= \mathcal{F}[\delta\delta_{f_{rep}}(f) \circ g_{har}(f)] \circ \mathcal{F}[g_{env}(f)] \\
 &= (\mathcal{F}[\delta\delta_{f_{rep}}(f)] \cdot \mathcal{F}[g_{har}(f)]) \circ \mathcal{F}[g_{env}(f)]
 \end{aligned} \tag{5.19}$$

The Fourier transform of the delta-comb remains a delta comb with a new comb spacing of  $t_{rep} = 1/f_{rep}$ . The Fourier transform of the two Gaussians remain Gaussian, whereas the new half-widths are determined by the bandwidth and the chirp.

$$\mathcal{F}[\delta\delta_{f_{rep}}(f)] = \sum_k \delta(t - t_{rep} \cdot k) = \delta\delta_{t_{rep}}(t) \tag{5.20}$$

$$\mathcal{F}[g_{har}(f)] = e^{-\frac{1}{2} \left( \frac{\Delta f_{har}^2}{1+4c_{har}^2 \Delta f_{har}^4} \right) t^2} e^{i \cdot \left( \frac{\Delta f_{har}^3}{1+4c_{har}^2 \Delta f_{har}^4} \right) t^2} = g_{APT}(t) \tag{5.21}$$

$$\mathcal{F}[g_{env}(f)] = e^{-\frac{1}{2} \left( \frac{\Delta f_{env}^2}{1+4c_{atto}^2 \Delta f_{env}^4} \right) t^2} e^{i \cdot \left( \frac{\Delta f_{env}^3}{1+4c_{atto}^2 \Delta f_{env}^4} \right) t^2} = g_{burst}(t) \tag{5.22}$$

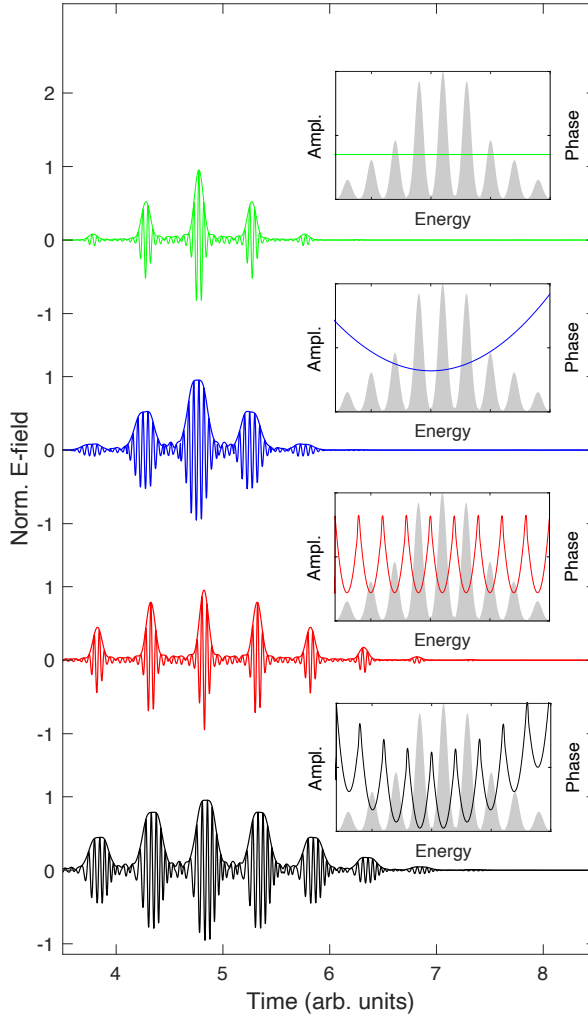
Hence, following Equation (5.19), we obtain repeating Gaussian bursts  $g_{burst}(t)$  within a longer temporal envelope  $g_{APT}(t)$ . The Gaussian which describes the spectral envelope now determines the duration of the single bursts in the time domain and vice versa. The Gaussian describing the harmonics determines the temporal envelope of the APT. Thus the harmonic chirp directly translates into a stretching of the envelope. In detail, the  $1/e$ -duration of the APT envelope  $\Delta t_{APT}$  and the duration of each burst  $\Delta t_{burst}$  depend on the chirp parameters as

$$\Delta t_{APT} = \frac{1}{\Delta f_{har}} \sqrt{1 + \Delta f_{har}^4 c_{har}^2} \tag{5.23}$$

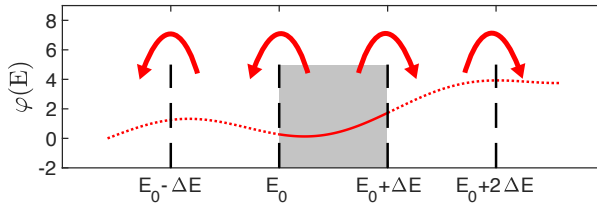
$$\Delta t_{burst} = \frac{1}{\Delta f_{env}} \sqrt{1 + \Delta f_{env}^4 c_{atto}^2}. \tag{5.24}$$

Figure 5.7 illustrates this behaviour for a typical APT-spectrum and for four different cases: (i) A flat phase. (ii) Only attochirp. (iii) Only harmonic chirp. (iv) Both atto- and harmonic chirp. The temporal broadening





**Figure 5.7:** Atto- and femtochirp in attosecond pulse trains. Four APTs, which have the same harmonic spectrum, but different spectral phase, are illustrated: (i) A flat phase (green). (ii) Only attochirp (blue). (iii) Only harmonic chirp (red). (iv) Both atto- and harmonic chirp (black). The insets show the corresponding spectra and, respectively, spectral phases.



**Figure 5.8:** Scheme to retrieve the phase  $\varphi(E)$  from the phases differences  $\Delta\varphi_{1-2}^{\pm}(E)$ . First,  $\varphi(E)$  is reconstructed in the interval  $[E_0, E_0 + E_{\text{IR}}]$  via a steadiness condition of  $\varphi(E)$  and its derivatives. Then  $\varphi(E)$  can be retrieved for all other  $E$  iteratively adding or subtracting  $\Delta\varphi_{1-2}^{\pm}(E)$ .

of the individual bursts is independent on the harmonic chirp, and respectively, also the broadening of the APT envelope is independent on the attochirp. In a real-world APTs typically both types of chirp are present.

#### 5.4 Reconstruction of absolute phases

In Section 5.1 the retrieval of the two phase differences  $\Delta\varphi_{1-2}^{+}(E) = \varphi(E - \hbar\omega_{\text{IR}}) - \varphi(E)$  and  $\Delta\varphi_{1-2}^{-}(E) = \varphi(E) - \varphi(E + \hbar\omega_{\text{IR}})$  from the experiment has been demonstrated. As these phase differences are retrieved continuously as function of energy across a broad energy range, they entail rich information about the spectral phase  $\varphi(E)$ . Naturally, the question remains, if also the exact form of  $\varphi(E)$  can be recovered. In this section a numerical reconstruction scheme is derived, which enables the recovery of  $\varphi(E)$  from  $\Delta\varphi(E)$ . In the following, we only focus on  $\Delta\varphi_{1-2}^{+}$  and drop the (+) for visibility.

It can be easily seen that

$$\Delta\varphi(E) = \varphi(E - E_{\text{IR}}) - \varphi(E) \quad (5.25)$$

with  $E_{\text{IR}} = \hbar\omega_{\text{IR}}$  corresponds to an approximation of the negative first derivative. The straight forward integration though only leads to reasonable results of  $\varphi(E)$ , if the variations of  $\varphi(E)$  are slower than  $E_{\text{IR}}$ . In turn, particularly for variations of  $\varphi(E)$  faster than  $E_{\text{IR}}$ , the integration leads to tremendously incorrect results. Equation (5.25) corresponds to a non-local-integro-differential equation.

In the following, let us assume that one knows  $\varphi(E)$  in the interval  $[E_0, E_0 + E_{\text{IR}}]$ , where  $E_0$ , in principle, can be any point. This known part of  $\varphi(E)$  is indicated as  $\tilde{\varphi}(E)$ . Then, Equation (5.25) can be rearranged to get

$$\varphi(E - E_{\text{IR}}) = \Delta\varphi(E) + \tilde{\varphi}(E) \quad (5.26)$$

and

$$\varphi(E + E_{\text{IR}}) = -\Delta\varphi(E + E_{\text{IR}}) + \tilde{\varphi}(E). \quad (5.27)$$

Hence, starting from the known interval  $[E_0, E_0 + E_{\text{IR}}]$ , one can determine  $\varphi(E)$  in the interval  $[E_0 + E_{\text{IR}}, E_0 + 2E_{\text{IR}}]$  and  $[E_0 - E_{\text{IR}}, E_0]$  using Equations (5.26) and (5.27) and the given phase difference  $\Delta\varphi(E)$ . The procedure can be repeated to determine  $\varphi(E)$  in the intervals  $[E_0 + 2E_{\text{IR}}, E_0 + 3E_{\text{IR}}]$  and  $[E_0 - 2E_{\text{IR}}, E_0 - E_{\text{IR}}]$  and can be iterated further. Figure 5.8 illustrates this procedure schematically. The initial guess  $\tilde{\varphi}(E)$  in the interval  $[E_0, E_0 + E_{\text{IR}}]$  is paramount as its functional form will be imprinted on all other intervals.

For the initial guess, the steadiness of  $\varphi(E)$  can be exploited. If the measured  $\Delta\varphi(E)$  is steady and differentiable, also  $\varphi(E)$  has to be steady and differentiable (the only exception would be that  $\varphi(E)$  features the same type of discontinuity repeating periodically with  $E_{\text{IR}}$ ). The same holds for all higher-order derivatives of  $\Delta\varphi(E)$  and  $\varphi(E)$ . Hence, Equation (5.27) can be used to determine a set of conditions for the initial guess  $\tilde{\varphi}(E)$ , which guarantees the steadiness of  $\varphi(E)$  and its derivatives at the interval boundaries.

$$\tilde{\varphi}(E_0 + E_{\text{IR}}) \stackrel{!}{=} \varphi(E_0 + E_{\text{IR}}) = -\Delta\varphi(E_0 + E_{\text{IR}}) + \tilde{\varphi}(E_0), \quad (5.28)$$

$$\tilde{\varphi}'(E_0 + E_{\text{IR}}) \stackrel{!}{=} \varphi'(E_0 + E_{\text{IR}}) = -\Delta\varphi'(E_0 + E_{\text{IR}}) + \tilde{\varphi}'(E_0), \quad (5.29)$$

$$\tilde{\varphi}''(E_0 + E_{\text{IR}}) \stackrel{!}{=} \varphi''(E_0 + E_{\text{IR}}) = -\Delta\varphi''(E_0 + E_{\text{IR}}) + \tilde{\varphi}''(E_0), \quad (5.30)$$

or generally,

$$\tilde{\varphi}^{(n)}(E_0 + E_{\text{IR}}) \stackrel{!}{=} \varphi^{(n)}(E_0 + E_{\text{IR}}) = -\Delta\varphi^{(n)}(E_0 + E_{\text{IR}}) + \tilde{\varphi}^{(n)}(E_0). \quad (5.31)$$

Hence, we obtain a set of equations, which relates the absolute values and all higher derivatives of the initial guess  $\tilde{\varphi}(E)$  at the initial interval

boundaries with the given  $\Delta\varphi(E)$ . In order to satisfy these conditions, we can write  $\tilde{\varphi}(E)$  as Taylor expansion around  $E_0$ ,

$$\tilde{\varphi}(E) = c_0 + c_1(E - E_0) + \frac{c_2}{2!}(E - E_0)^2 + \dots + \frac{c_n}{n!}(E - E_0)^n \quad (5.32)$$

We can then evaluate Equations (5.28) to (5.30) to get a linear system of equations for the Taylor coefficients  $c_n$ . E.g. when truncating the expansion at the third order, they read

$$c_0 + c_1 E_{\text{IR}} + \frac{c_2}{2!} E_{\text{IR}}^2 + \frac{c_3}{3!} E_{\text{IR}}^3 = -\Delta\varphi(E_0 + E_{\text{IR}}) + c_0, \quad (5.33)$$

$$c_1 + c_2 E_{\text{IR}} + \frac{c_3}{2!} E_{\text{IR}}^2 = -\Delta\varphi'(E_0 + E_{\text{IR}}) + c_1, \quad (5.34)$$

$$c_2 + c_3 E_{\text{IR}} = -\Delta\varphi''(E_0 + E_{\text{IR}}) + c_2. \quad (5.35)$$

and the coefficients become

$$c_1 = \frac{1}{E_{\text{IR}}} [-\Delta\varphi(E_0 + E_{\text{IR}}) - \frac{c_2}{2!} E_{\text{IR}}^2 - \frac{c_3}{3!} E_{\text{IR}}^3], \quad (5.36)$$

$$c_2 = \frac{1}{E_{\text{IR}}} [-\Delta\varphi'(E_0 + E_{\text{IR}}) - \frac{c_3}{2!} E_{\text{IR}}^2], \quad (5.37)$$

$$c_3 = \frac{-\Delta\varphi''(E_0 + E_{\text{IR}})}{E_{\text{IR}}}. \quad (5.38)$$

The offset coefficient  $c_0$  remains undetermined, analogue to an integration constant.

With the expansion in the interval  $[E_0, E_0 + E_{\text{IR}}]$ , one can then determine  $\varphi(E)$  on the full energy range via the iterative procedure described above. The starting point  $E_0$  can, in principle, be chosen arbitrarily and the final solution should be independent of it. However, as not all higher derivatives of  $\Delta\varphi(E)$  can be taken into account, slightly different solutions are obtained for different starting points. For "too" high orders of the derivatives, numerical instabilities even lead to larger variations for different starting points, which implies an optimal order. In order to account for such instabilities and to average out the starting point dependence, different starting points can be chosen and the retrieved solutions averaged. In the following, the expansion is truncated at the third order.

Figure 5.9 shows  $\varphi(E)$ , retrieved from  $\Delta\varphi_{1-2}^+(E)$  from the SAE simulation from Section 5.1. The shown  $\varphi(E)$  represents the average of solutions

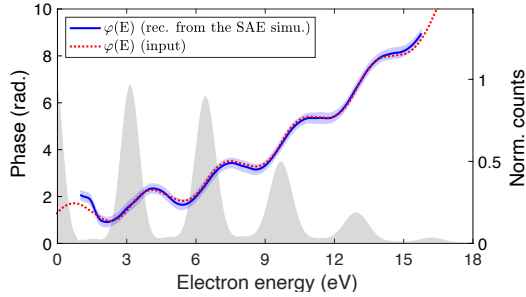


**Figure 5.9:** Reconstructed  $\varphi(E)$  from  $\Delta\varphi_{1-2}^+(E)$  from the SAE simulation (Figure 5.3). The blue line represents the average of  $\varphi(E)$  obtained from 100 reconstructions with different starting values  $E_0$ . The shaded area indicates the variance of the different reconstructions. The red line shows the input  $\varphi(E)$  of the SAE simulation. A linear phase is added to the input phase, to account for the unknown absolute offset of  $\Delta\varphi_{1-2}^+(E)$  and the undetermined coefficient  $c_0$  in the reconstruction.

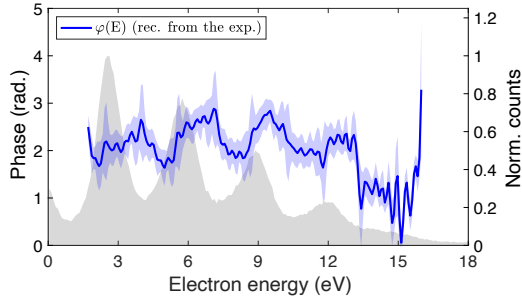


**Figure 5.10:** Reconstructed  $\varphi(E)$  from  $\Delta\varphi_{1-2}^+(E)$  from the experiment (Figure 5.2). The blue line represents the average of  $\varphi(E)$  obtained from 100 reconstructions with different starting values  $E_0$ . The shaded area indicates the variance of the different reconstructions.

for 100 possible starting values  $E_0$ , equidistantly spaced across the full energy range of  $\Delta\varphi_{1-2}^+(E)$ . The shaded area shows the variance of the obtained solutions for the different starting values. The retrieved  $\varphi(E)$  is in excellent agreement with the simulation input phase, which finally confirms the reconstruction method. It has to be noted that a linear phase is added to the retrieved  $\varphi(E)$  to see the overlap with the input phase. This linear phase relates to the undetermined coefficient  $c_0$  in Equation (5.32) and the unknown absolute offset of  $\Delta\varphi_{1-2}^+(E)$ , retrieved from the simulation or experiment.

Finally, Figure 5.10 presents  $\varphi(E)$  retrieved from the experimentally measured  $\Delta\varphi_{1-2}^+(E)$  from Section 5.1. Likewise, the shown  $\varphi(E)$  corresponds to the average of 100 starting points in the reconstruction. Despite a larger variance, clear oscillations of  $\varphi(E)$  are visible, representing the harmonic chirp.

## 5.5 Outlook

The 1-2-quantum beat method presented in this chapter provides a novel technique to characterize the photoelectron spectral phase. Conceptionally similar to the RABBITT method, it does, however, not distinguish between mainbands and sidebands. In contrast to the latter, it also allows one to retrieve phase information continuously as a function of energy and across the full energy spectrum of an attosecond pulse train.

However, providing superior phase information, the technique also comes with stronger conceptual limitations. The retrieval procedure relies on the photoionization from a single state. For ionization from other than *s*-ground states, adaptations of the technique have to be carried out. Further, for complex targets involving multiple ionization channels, assumptions on their coherence properties would have to be made. The required angle-resolved detection and CEP-stabilisation increase the technical demands.

For future experiments, a trade-off between the benefits and drawbacks of the different attosecond spectroscopies has to be made. In principle, not only RABBITT and the here introduced 1-2-quantum beat method, but also other methods [95, 96, 111–114] cover different areas of applications. The method of choice is ultimately determined by the target under investigation.

# Free-running quantum interferometry

In RABBITT and related techniques, attosecond photoionization time delays are retrieved via phase differences from different quantum beatings. In fact, photoionization time delays represent derived quantities from actual phase measurements. Hence, as long as the combination of the employed light fields enables the quantum interferometer, the pulse duration of the light fields does not influence the achieved temporal resolution. Indeed, in typical attosecond photoionization experiments, the pulse durations of the employed light pulses are much longer than the retrieved photoionization time delays. Naturally, one may ask the question: If attosecond precision can be achieved in pump-probe experiments without attosecond pulses, does the pump-probe delay need to be scanned with attosecond precision?

In the publication presented in this chapter, a novel analysis method of RABBITT-type experiments is introduced, demonstrating that neither attosecond light pulses nor attosecond delay scans are needed for the observation of attosecond photoionization time delays. The technique relaxes experimental demands and opens the possibility to study attosecond photoionization time delays at Free electron lasers, where an attosecond delay synchronization between pump and probe pulses cannot be achieved.

The publication is presented in Section 6.1. In Section 6.2 the technique is applied in a cutting-edge experiment within the AttoCOLTRIMS setup. In Section 6.3 an outlook is presented.

Details about the publication printed in this chapter are listed below. The text and figures are as in the publication. Only the style of the text, figures and equations has been adapted to the style of the thesis. Further, the numbering of the figures and references has been adjusted. The reference list of the publication has been included in the reference list of the thesis. The mathematical notation is kept as in the original publication and slightly varies from other parts of this thesis.

**Title:** "Attosecond resolution from free running interferometric measurements", [115]  
**Journal:** *Optics Express*  
**doi:** 10.1364/OE.391791  
**URL:** <https://doi.org/10.1364/OE.391791>  
**Published:** 27<sup>th</sup> April 2020  
**License:** OSA Open Access Publishing Agreement

©2020 Optical Society of America. Users may use, reuse, and build upon the article, or use the article for text or data mining, so long as such uses are for non-commercial purposes and appropriate attribution is maintained. All other rights are reserved.



## 6.1 Attosecond resolution from free running interferometric measurements

*Constantin Krüger<sup>1,\*</sup>, Jaco Fuchs<sup>1,\*,\*\*</sup>, Laura Cattaneo<sup>1</sup> and Ursula Keller<sup>1</sup>*

<sup>1</sup> Department of Physics, ETH Zurich, 8093 Zurich, Switzerland

\* These authors contributed equally to this work.

\*\* [jafuchs@phys.ethz.ch](mailto:jafuchs@phys.ethz.ch)

Attosecond measurements reveal new physical insights in photoionization dynamics from atoms, molecules and condensed matter. However, on such time scales, even small timing jitter can significantly reduce the time resolution in pump-probe measurements. Here, we propose a novel technique to retrieve attosecond delays from a well-established attosecond interferometric technique, referred to as Reconstruction of Attosecond Beating By Interference of Two-photon Transition (RABBITT), which is unaffected by timing jitter and significantly improves the precision of state-of-the-art experiments. We refer to this new technique as the Timing-jitter Unaffected Rabbitt Time deLay Extraction method, in short TURTLE. Using this TURTLE technique, we could measure the attosecond ionization time delay between argon and neon in full agreement with prior measurements. The TURTLE technique allows for attosecond time resolution without pump-probe time delay stabilization and without attosecond pulses because only a stable XUV frequency comb is required as a pump. This will more easily enable attosecond measurements at FELs, for example, and thus provide a valuable tool for attosecond science. Here we also make a MATLAB code available for the TURTLE fit with appropriate citation in return.

### 6.1.1 Introduction

The discovery of high harmonic generation (HHG) [116] and the better understanding of phase matching [20] offered access to ultrabroad pulses in the extreme ultraviolet (XUV) range. Given that HHG is a coherent non-linear process, attosecond pulse generation was predicted [117], however,

the pulse duration measurement became the new challenge. This was resolved with the RABBITT technique (Reconstruction of Attosecond Beating By Interference of Two-photon Transitions) [4, 13], which was used to measure the first attosecond pulses within an attosecond pulse train (APT) repeating every half infrared (IR) laser cycle used for the HHG. Single attosecond pulses (SAPs) then were first measured with the attosecond streak camera technique [28]. Both the RABBITT and the attosecond streaking techniques are based on a pump-probe scheme, where an XUV attosecond pump pulse ionizes electrons and an IR probe pulse interacts with the released electrons, leading to an alternation of the photoelectron spectrum when the time delay between pump and probe is varied. The RABBITT technique uses an APT in combination with a weak ( $< 10^{11}$  W/cm<sup>2</sup>) and typically long IR ( $\approx 30$  fs) pulse. For attosecond streaking, a linear polarized few-cycle IR probe pulse is used together with a SAP. These two techniques not only have been used to characterize attosecond pulses but also to resolve electron ionization dynamics in atoms [6, 30, 55, 59–61, 118–120], small molecules [36, 38, 121], up to biomolecules [122] and solids [5, 123]. Streaking traces have to be analyzed in the time-domain and rely on reconstruction algorithms with different approximations [100, 112, 124, 125], whereas the interference nature of the RABBITT-method allows for a more direct retrieval of the spectral phases [60, 126].

However, both methods require an attosecond pump-probe delay control, which remains challenging and any XUV-IR pulse timing jitter with uncontrolled fluctuations of the pump-probe delay can reduce the temporal resolution. Here we show that, for the RABBITT technique, we do not need any pump-probe delay control and attosecond time resolution can be achieved with a novel retrieval method, which is unaffected by jitter. This method, which we call Timing-jitter Unaffected Rabbitt Time deLay Extraction, in short TURTLE, proves that neither attosecond pulses nor attosecond delay precision is needed to retrieve attosecond delays. In detail, we show that the sidebands (SBs) forming a RABBITT trace can be represented through an ellipse parametrization, which removes the pump-probe delay dependence in their analysis. An analogous method has previously been proposed for gravimeter measurements [127] and is here adapted for attosecond science.

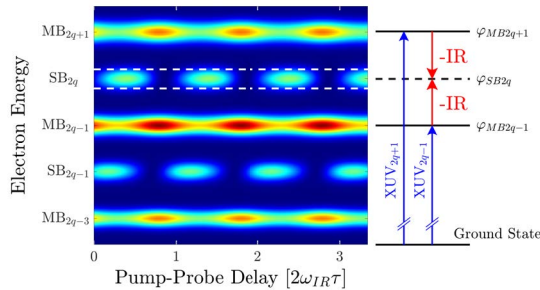


**Figure 6.1:** Example RABBITT spectrum, simulated within the strong-field approximation [82]. The IR probe transfers electron population from the mainbands (MBs) to the sidebands (SBs), which oscillates with the delay between XUV pump and IR probe. The quantum pathways leading to the corresponding SB are illustrated schematically.

Figure 6.1 shows an example RABBITT spectrum, where the photoelectron spectrum varies as a function of pump-probe delay  $\tau$  between the XUV pump and the IR probe pulse. Upon absorption of an XUV photon, the photoemitted electron presents a kinetic energy which equals the difference between the XUV photon energy minus the ionization potential of the target. Hence, the photoelectron spectrum represents a replica of the XUV spectrum, shifted by the ionization potential and multiplied by the target specific ionization cross section. Due to the formation of an attosecond pulse train (APT) via HHG, the XUV spectrum consists of odd harmonics of the generating laser frequency, which results in discrete mainbands (MB) indexed  $2q+1$  ( $q \in \mathbb{N}$ ) in the photoelectron spectrum. Due to the simultaneous presence of the IR probe, the absorption or stimulated emission of a further IR photon transfers electron population from the MBs to the SBs. These SBs oscillate as a function of the pump-probe delay as

$$I_{2q}(\tau) \approx A_{2q} + B_{2q} \cdot \sin(2\omega_{IR}\tau + \varphi_{2q}), \quad (6.1)$$

where  $A_{2q}$  and  $B_{2q}$  are offset and amplitude of the oscillation and  $\omega_{IR}$  corresponds to the IR frequency. The SB phase, in turn, contains different terms as follows:

$$\varphi_{2q} = \Delta\varphi_{2q}^{XUV} + \Delta\varphi_{2q}^{at} + 2\omega_{IR}\tau_0, \quad (6.2)$$

where  $\Delta\varphi_{2q}^{XUV}$  is the XUV contribution, corresponding to the phase dif-

ference between the XUV harmonics  $2q-1$  and  $2q+1$  (Fig. 6.1),  $\Delta\varphi_{2q}^{at}$  is an atomic phase, which depends on the ionized target species, and the last term is an overall offset phase due to the unknown time zero  $\tau_0$ . In detail, the atomic phase corresponds to the phase difference due to the half-scattering process at the residual ionic potential between the two quantum paths leading to the SB formation [31, 57, 61]. Typically [30, 38, 55, 59–61, 120], the SB phase is retrieved either via Fourier transform analysis or by performing a sinusoidal fit, which we further refer to as the sine-fit method. The retrieved phase can then be used twofold: (1) To estimate the attochirp,  $\Delta(\Delta\varphi^{XUV})$ , by using theoretical values for the atomic phase and comparing the phase difference of neighboring SBs [13, 61]; or (2) to extract the atomic phase by comparing the phase difference between SBs stemming from different ionization channels or species but using the same SB order. Thus  $\Delta\varphi^{XUV}$  cancels out and the difference of  $\Delta\varphi^{at}$  can be isolated. This gives access to the photoionization time delays  $\tau_{at}$  [30, 33, 38, 55, 59, 60, 120] via

$$\tau_{at} = \frac{\Delta\varphi_{SB1}^{at} - \Delta\varphi_{SB2}^{at}}{2\omega_{IR}}. \quad (6.3)$$

In both cases, a relative phase between two SBs, *i.e.* their phase difference  $\Delta\varphi = \varphi_{SB1} - \varphi_{SB2}$ , has to be determined such that the unknown time zero cancels out. Isinger et al. [126] investigated the precision of the RABBITT technique and found that the precision of the retrieved phase is predominantly limited by the temporal stability of the pump-probe delay, *i.e.*, the timing jitter or time-drift between the two pulses. Although the active interferometric stabilization loops are used to reduce such effects, the pump-probe delay control is still the limiting factor for the precision in state-of-the-art experiments.

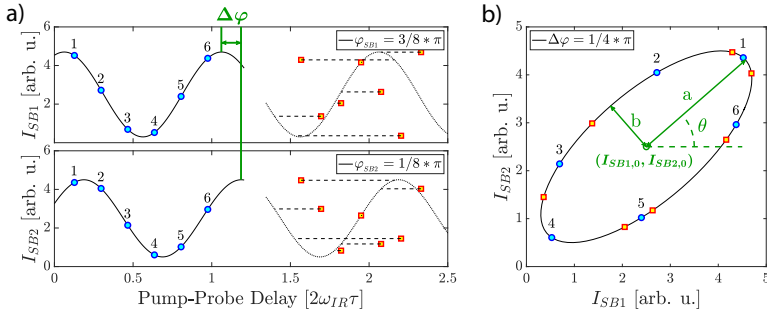
We will now present a new approach to overcome this issue, before comparing its precision with the sine-fit RABBITT extraction method in section 3. In section 4, we present a proof-of-principle experiment, where we measure RABBITT traces simultaneously in argon and neon gas targets [33, 60] without a delay scan and analyze the resulting SBs using TURTLE.

### 6.1.2 The method

To date attosecond time delays are calculated by fitting a sinusoidal function to the SB and extracting the calculated phase. Foster et. al [127] proposed a method to extract the relative phase between two sinusoidal functions from coupled gravimeter interferometers, based on ellipse-specific fitting. This method is not affected by timing jitter. By analogy with SB intensities representing sinusoidal functions, any pair of SBs parametrizes an ellipse in the intensity correlation domain, *i.e.*  $I_{SB1}$  vs.  $I_{SB2}$ . Moreover, the relative phase  $\Delta\varphi$  between the analysed SBs relates to the ellipse geometry as follows (Appendix A for the detailed derivation):

$$\Delta\varphi = \varphi_{SB1} - \varphi_{SB2} = \arctan\left(\frac{b}{a} \cdot \tan(\theta)\right) - \arctan\left(\frac{a}{b} \cdot \tan(\theta)\right) + \frac{\pi}{2} \quad (6.4)$$

where  $a$  and  $b$  are the major and minor half-axis, and  $\theta$  corresponds to the tilt angle of the major half axis with respect to the x-axis, or respectively  $I_{SB1}$ -axis (Fig. 6.2b).



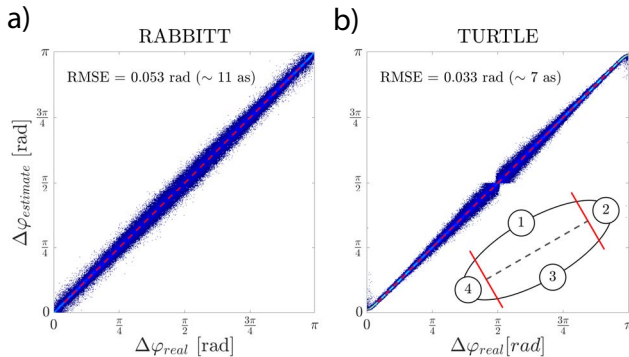
**Figure 6.2:** Illustration of the TURTLE method. a) Two example SB oscillations with  $\varphi_{SB1} = 3/8$  and  $\varphi_{SB2} = 1/8$ , where the blue circles correspond to jitter-free acquisition and the red squares correspond to jitter affected acquisition. b) The intensity correlation of SB 1 and 2 form the same ellipse for both acquisition types. The data points which are acquired jitter-free line up sequentially (counter-clockwise) on the ellipse, indicated by the numbering.

Figure 6.2 illustrates the extraction of the relative phase between two SBs using the ellipse parametrization for two cases: the left part (Fig. 6.2a) shows an equidistant sampling of two SBs, for which the phase difference can be retrieved by a sine-fit (blue samples enumerated from one to six). In the SB intensity correlation domain (Fig. 6.2b) the data-points line up

counter-clockwise on the ellipse, from which  $\Delta\varphi$  can be calculated using Eq. (6.4). The right part of Fig. 6.2a shows data points of the same SBs subjected to jitter (red squares). For these data points, seemingly randomly distributed, the phase difference cannot be extracted using the sine-fit method. However, its intensity correlation remains unchanged due to the fact that both SBs are subjected to the same delay fluctuations. Accordingly, they satisfy the same ellipse equation as in the jitter-free case, and, hence,  $\Delta\varphi$  can be determined. Algebraically, this is given by the fact that in the ellipse parametrization,  $\Delta\varphi$  does not depend on the pump-probe delay  $\tau$  anymore. Nevertheless, there are two constraints, which have to be satisfied. First, during the acquisition of a single data point, the jitter must be negligible. This is typically satisfied for shot-to-shot acquisition in large-scale facilities and for table-top experiments where the integration time per delay step is small compared to thermal drift. Second,  $\Delta\varphi$  takes only values from 0 to  $\pi$ , *i.e.* it remains unknown which of the SBs is advanced. To overcome this ambiguity, the rotation direction has to be captured (clockwise rotation means SB1 is delayed vs. SB2 and vice versa), which can be determined as long as the jitter is not larger than a full oscillation period. Since the formation of SBs only requires that the XUV bandwidth is at least twice the IR photon energy but does not depend on the pulse duration, neither attosecond pulses nor an attosecond delay control is required for measuring attosecond photoionization delays with TURTLE. The applicability is thus the same as in the sine-fit RABBIT technique, but with less requirements. The two analyzed SBs can either come from (1) the same ionization channel and different SB orders in order to characterize the attosecond pulse train, or (2) from two different ionization channels but the same SB order to measure photoionization time delays. Subsequently, we will compare the precision of TURTLE with the sine-fitting RABBIT technique before demonstrating its validity in a proof-of-principle experiment for unstabilized pump-probe delays.

### 6.1.3 Comparison between TURTLE and the sine-fit analysis

In order to compare the TURTLE method with the traditional sine-fit method, we consider two regimes: a high-jitter regime and a low-jitter regime.



**Figure 6.3:** Comparison of the delay precision between a) the sine-fit method b) and the TURTLE method for 200'000 SB pair simulations. The phase shifts obtained by the two methods are plotted versus the input phase shift. TURTLE provides a higher average precision (Root mean square error, RMSE of 0.033 rad) than the sine-fit method (RMSE of 0.053 rad).

In the high-jitter regime, the pump-probe delay fluctuations are considered larger than half a laser cycle, as it is the case for current state-of-the-art (seeded) free-electron lasers (FELs). However, since shot-to-shot acquisition is possible in such facilities, the TURTLE technique can enable the extraction of attosecond photoionization delays. In contrast, the traditional RABBITT sine-fit is not possible at all. The retrieved delay precision is only restricted by the flux stability and the acquisition time. We note that the timing jitter has to be smaller than the IR pulse duration since otherwise, envelope effects become relevant. However, in this case, other shot-to-shot pump-probe cross-correlation techniques [128] can be used to obtain a first rough timing reference.

In the low-jitter regime, shot-to-shot pump-probe fluctuations are negligible and only small uncontrolled delay fluctuations (smaller than the tenth of a laser cycle) occur during the data acquisition at a fixed delay time. This is typically the case for table-top attosecond photoionization experiments. Accordingly, delay scans can be performed and both TURTLE and sine-fit can be used for the delay retrieval. In principle, the delay can also be extracted via Fourier transform and fitting a sinc-function to the peak of the Fourier spectrum, which is equivalent to the sine-fit method. The discrepancy between sine-fit and Fourier-method are hereby negli-

ble and we only compare to the sine-fit method in the following. Figure 6.3 shows a comparison of the TURTLE and the sine-fit method in a delay-scanned measurement under common experimental conditions. For this, we test both methods on sets of simulated SB pairs, generated via Equation 6.1 with different intensities, amplitudes, and phases, the latter uniformly ranging from 0 to  $\pi$ . Each SB does 5 oscillations covering a pump-probe scan of 7 fs for an 800 nm laser wavelength with 50 steps of 130 as, in accordance with recent experiments [30, 55, 59, 60, 120]. Furthermore, we add 5% of amplitude noise and 80 as timing jitter to mimic experimental conditions. For the sine-fit extraction method, two sinusoidal functions are fitted simultaneously using a least-square minimization in order to guarantee a common oscillation frequency. For the TURTLE method, a novel ellipse fitting routine is developed, which guarantees that successively acquired data points are fitted by the same section of the ellipse. Here we take advantage of the fact that in the delay-scanned acquisition, neighboring data points of the SB oscillation also correspond to neighboring data points on the ellipse or, respectively, lie on the same side of the ellipse when there is a small amount of timing jitter (Fig. 6.2). A detailed description of the fit implementation is given in Appendix B. As shown in Fig. 6.3 TURTLE generally provides a higher precision in the phase retrieval than the sine-fitting method. In particular, using TURTLE, the retrieved phases  $\Delta\varphi$  for the set of 200'000 simulated SB pairs show a 63% lower root mean square error (RMSE) compared to the sine-fit method. This can be explained by the fact that TURTLE is not affected by timing jitter. Indeed, when the same test is performed on simulations without jitter, both methods yield comparable precision. The shape of the error spread can be explained by inspecting equation 4. When  $\Delta\varphi$  approaches 0 or  $\pi$ , the ellipse becomes narrow and the determination of the tilt angle  $\theta$  improves. Additionally, the fraction  $a/b$  becomes large, which yields a large argument in the arctangent and thus TURTLE becomes less susceptible to errors. However, the estimation slightly diverges as TURTLE tries to fit an ellipse with zero opening on noisy data. We note that the bottleneck at  $\Delta\varphi = \pi/2$  does not correspond to zero error spread; in fact, the error is maximal here.

In summary, TURTLE does not only enable the delay extraction in the



high-jitter case, i.e., for FELs, but also provides a more accurate tool for table-top laser experiments which usually have lower timing jitter.

### 6.1.4 Proof-of-principle experiment

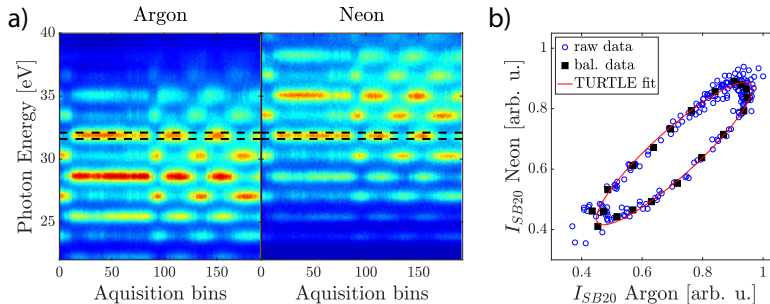


**Figure 6.4:** (a) Experimental RABBITT trace from argon 3p (left) and neon 2p (right) photoionization obtained by the thermal drift of the experimental setup. The black dotted lines indicate the energy range integrated to obtain the signal of SB 20. (b) Correlation of the SB intensities. The blue circles show the raw data, the black squares the balanced representation, and the red ellipse the TURTLE fit.

In a last step, we record a RABBITT trace using the same setup as described in [48], but without any stabilization of the pump-probe delay and without using any delay scan. The thermal drift of the optical components forming the two arms of the pump-probe setup is the main reason for an uncontrolled timing jitter between the two pulses. Figure 6.4 shows a 12-hours RABBITT trace measured in a gas mixture of argon and neon (1:1) without a delay scan. The coincidence detection of the cold target recoil ion momentum spectrometer [50] allows us to isolate RABBITT spectra for the two atomic species. The data are binned in time intervals of 4 min, which are short enough to resolve delay variations. Figure 6.4b shows the intensity correlation of SB 20 for both atoms and the corresponding TURTLE fit for the phase retrieval. Since the drift is random, the obtained data points do not sample the ellipse homogeneously as in a delay-scanned acquisition, thus a balancing of the raw data is required. The data points are averaged in 20 evenly spaced angular segments around the center of a primarily fitted ellipse and an average value is assigned for each angular segment. The final ellipse is then fitted on the balanced dataset. Although

the balancing is not needed in our specific experiment, it might become more crucial in other measurements. We obtain a delay of  $88 \pm 6$  as at a photon energy of 31.9 eV in excellent agreement with previous measurements ( $85 \pm 10$  as, at 32.1 eV [60]). For the error analysis, we first calculate the standard deviation within each segment as well as its mean distance to the fitted ellipse to estimate the error of the fit. Consecutively, we perform an error propagation on Eq. (6.4) where we use the same error for the major and minor half axis, and neglect the error on the tilt angle  $\theta$ . This experiment demonstrates that TURTLE is a viable method for retrieving attosecond time delays without the need for pump-probe delay scans with attosecond precision.

In particular, TURTLE enables the retrieval of attosecond delays in single-shot acquisition measurements with high XUV flux where shot-to-shot jitter can be as large as few femtoseconds, currently typically observed for FEL facilities [128–130]. Note that a multi-color (at least two-color) XUV spectrum is required in order to enable the interference of two-photon transitions. Such spectra have recently become available at different FEL facilities [17, 131, 132], enabling the application of TURTLE. Therefore the TURTLE technique enables photoionization experiments beyond the typical RABBITT application for which the SB generating laser field is from the same source as the generating laser field for the HHG [133], which reduces their relative timing jitter in the measurements.

### 6.1.5 Conclusion

We developed a novel analysis technique, TURTLE, which enables a jitter-free retrieval of attosecond photoionization delays from RABBITT measurements. Using a correlation representation of the SB intensities, the method not only allows for the retrieval of attosecond delays with higher precision than the sine-fit method but also opens up new experimental approaches. In particular, we demonstrate in a proof-of-principle experiment that TURTLE neither requires attosecond light pulses nor attosecond delay control in order to retrieve attosecond ionization delays. Solely by exploiting the unstabilized timing jitter in the experiment, we retrieve the Ar-Ne delay in excellent agreement with literature values. Our method not only supports state-of-the-art table-top laser experiments but also paves the

way for attosecond measurements at FEL facilities and thus provides a valuable tool to the field of attosecond science.

### Appendix A: Derivation of Equation (6.4)

The parametric equation of an ellipse in Cartesian coordinates with the major axis  $a > 0$  parallel to the x-axis and the minor axis  $b > 0$  parallel to the y axis is (Fig. 6.5, blue ellipse):

$$\begin{aligned} x(t) &= a \cdot \cos(t) \\ y(t) &= b \cdot \sin(t), \end{aligned} \tag{6.5}$$

where  $t$  ranges from 0 to  $2\pi$ . Applying a rotation by an angle  $\theta$  and a shift by  $x_c$  in x-direction and  $y_c$  in y-direction the ellipse becomes (Fig. 6.5, green ellipse)

$$\begin{aligned} x(t) &= x_c + a \cdot \cos(\theta) \cdot \cos(t) - b \cdot \sin(\theta) \cdot \sin(t) \\ y(t) &= y_c + a \cdot \sin(\theta) \cdot \cos(t) + b \cdot \cos(\theta) \cdot \sin(t). \end{aligned} \tag{6.6}$$

The ellipse rotation is illustrated in Fig. 6.5. The rotation angle  $\theta$  only ranges from  $-\pi/2$  to  $\pi/2$  in order to avoid ambiguities. Using trigonometric identities (linear combination of trigonometric functions) Eq. (6.6) can be rearranged to

$$\begin{aligned} x(t) &= x_c + x_0 \cdot \sin\left[t + \arctan\left(\frac{b}{a} \cdot \tan(\theta)\right) + \frac{\pi}{2}\right] \\ y(t) &= y_c + y_0 \cdot \sin\left[t + \arctan\left(\frac{a}{b} \cdot \tan(\theta)\right)\right], \end{aligned} \tag{6.7}$$

where  $x_0 = \sqrt{a^2 \cos^2(\theta) + b^2 \sin^2(\theta)}$  and  $y_0 = \sqrt{a^2 \sin^2(\theta) + b^2 \cos^2(\theta)}$ . The ellipse parametric equation has the same structure as two SB signals (Eq. (6.1)):

$$\begin{aligned} I_{SB1}(\tau) &= A_{SB1} + B_{SB1} \cdot \sin(2\omega\tau + \varphi_{SB1}) \\ I_{SB2}(\tau) &= A_{SB2} + B_{SB2} \cdot \sin(2\omega\tau + \varphi_{SB2}). \end{aligned} \tag{6.8}$$

Hence, the phase difference  $\Delta\varphi$  between two SBs can be identified as in Eq. (6.4).

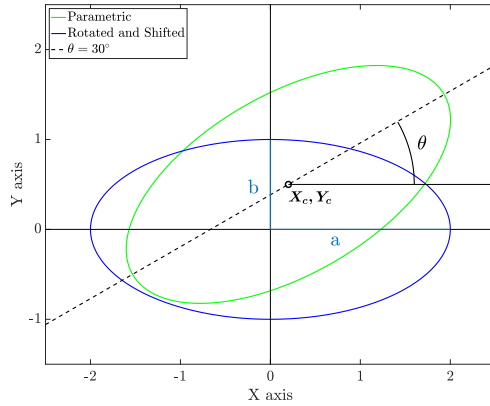


Figure 6.5: Illustration of the rotated and shifted ellipse.

## Appendix B: TURTLE ellipse fit for delay-scanned acquisition

We separate the data-points in four segments along the major axis of the ellipse. Two edge segments (2 and 4) as well as an upper (1) and lower (3) center segment, illustrated by the inset in Fig. 6.3. Afterwards, we group consecutive data-points in batches, until the following point crosses a segment boundary (solid red line in the inset of Fig. 6.3). For example, five SB oscillations will result in  $5 \times 4 = 20$  batches if there is no noise. Otherwise, there might be more batches, because amplitude fluctuations and jitter can cause multiple crossings. The data-points in the center batches (segments 1 and 3) are then fitted jointly either by the upper or the lower segment of the ellipse, depending on which minimizes the entire batch residual. This avoids that data-points in the center segments are not mistakenly fitted to the wrong side of the ellipse, which is especially important for noisy and narrow ellipses ( $\Delta\varphi$  close to 0 or  $\pi$ ). The data-points in the edge batches (segments 2 and 4) are fitted individually by the closer ellipse part (upper or lower), because here it is not known a priori to which side of the ellipse they belong. To make the distinction between upper and lower part, the ellipse is rotated onto the x-axis, where both parts can be expressed by

$$f_{up}(x) = -f_{down}(x) = b \cdot \sin(\arccos(\frac{x - x_0}{a})) \quad (6.9)$$

where  $a$  and  $b$  are the major and minor half-axis, and  $x_0$  is the center of the rotated ellipse. The segment boundaries are given by  $x = x_0 \pm 0.5a$ . Accordingly, the fit is conducted by minimising the least-square residual

$$\begin{aligned} \text{Res} = & \sum_i \min([-f(x_i) - y_i]^2, [f(x_i) - y_i]^2) \\ & + \sum_j \min\left(\sum_{k \in K_j} [-f(x_k) - y_k]^2, \sum_{k \in K_j} [f(x_k) - y_k]^2\right) \end{aligned} \quad (6.10)$$

where  $i$  runs over all data-points in the edge segments,  $j$  runs over the center batches and  $k$  runs over the  $K_j$  data-points in each center batch. A MATLAB code for the TURTLE ellipse fit is provided online (Ref. [115], note that the function `fminsearchbnd` is required for execution of the code [134]).

**Funding.** Schweizerischer Nationalfonds zur Förderung der Wissenschaftlichen Forschung (NCCR MUST).

**Disclosures.** The authors declare no conflicts of interest.

### Author contributions

J.F developed the method and led the study. U.K supervised the study. C.K., J.F and L.C conducted the experiments. C.K. and J.F. analyzed the experiments. C.K. implemented the code. All authors were involved in the interpretation and contributed the final manuscript.

## 6.2 Investigation of molecular photoionization time delays with TURTLE

This section presents the measurement of photoionization time delays in acetylene. The TURTLE method is applied to retrieve the photoionization time delays.

In molecular photoionization spectroscopy, generally, a great number of ionization channels as well as fragmentation channels are available. Hence, compared to atoms, typically much longer integration times are required. For this reason, the TURTLE method is employed, enabling RABBITT scans with  $> 24$  h acquisition time, unaffected by long-term drifts of the delay line and even without active stabilization.

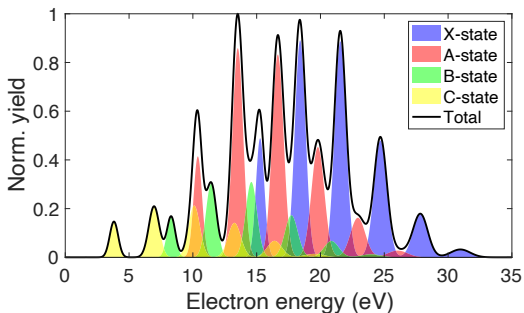


**Figure 6.6:** Theoretical acetylene photoelectron spectrum for an harmonic XUV spectrum, which is centred around 32 eV and with a fundamental wavelength of 785 nm. The contributions of the four states contributing states are highlighted.

The acetylene molecule ( $C_2H_2$ ) is a symmetric and linear molecule (see Table 6.1 for the molecular structure) and is therefore considered as one of the simplest organic molecules. Despite its simplicity, various effects such as triple bond-break, isomerization and hydrogen migration can be studied. For the here investigated energy regime, four ionization channels are available, for which the different ionization potentials are listed in Table 6.1. As the energy-dependent photoionization cross section of the four ionization channels is known, the resulting single-photon photoelectron spectrum can be theoretically modeled via

$$PES(E) = \sum_i I_{XUV}(E - I_{p,i}) f_i(E) \quad (6.11)$$

where  $I_{XUV}(E)$  is the XUV harmonic spectrum,  $I_{p,i}$  is the adiabatic ionization potential of state  $i$  with ionization cross section  $f_i(E)$ , and the sum runs over the four accessible states. Figure 6.6 shows the resulting theoretical photoelectron spectrum for a high-harmonic spectrum of a generating wavelength of 785 nm. The contributions of the different states are visualized. Given their difference in ionization potential, the bands of the X- and A-state, and respectively the bands of B- and C-state, fall in between each other, such that the full spectrum is occupied. Hence, in the case of a RABBITT experiment, the SBs of the specific states overlap with the MBs of the other states. Isolated SBs can only be found in the upper and lower tail of the spectrum.

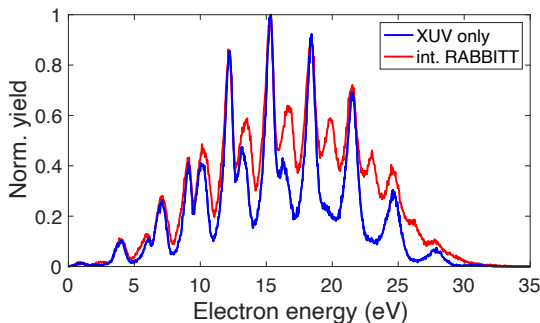


**Figure 6.7:** Comparison of the experimental photoelectron spectra for an XUV-only and for a delay integrated RABBITT measurement, filtered on non-dissociative events. The sideband positions, which are not (or only little) affected by other states can be identified.

Structure	Molecular State	AIP
H-C≡C-H	X-State	11.4 eV
	A-State	16.3 eV
	B-State	18.4 eV
	C-State	22.9 eV

**Table 6.1:** Adiabatic ionization potentials of the 4 energetically highest lying molecular states in neutral acetylene.

Figure 6.7 shows the comparison of an experimental XUV-only and a delay-integrated RABBITT spectrum. In both cases, the photoionization events are filtered on non-dissociative events via the coincidence detection of the COLTRIMS. Photoionization from states other than the X-state results in excited states of the molecular ion, which have a lower binding energy [135]. In turn, without being exclusive, when filtering on non-dissociative events, the share of photoelectrons stemming from the X-state is increased. As can be seen in Figure 6.7, the three energetically highest SBs can be well distinguished from other contributions in the photoelectron spectrum and are likely only to contain contributions from the X-state.

In order to determine molecular photoionization delays, a helium- and Acetylene RABBITT are acquired simultaneously by using a 50:50 gas mixture in the gas jet. The RABBITT spectrograms of the two species, shown in Figure 6.8, are separated posteriorly via ion time-of-flight filtering. The

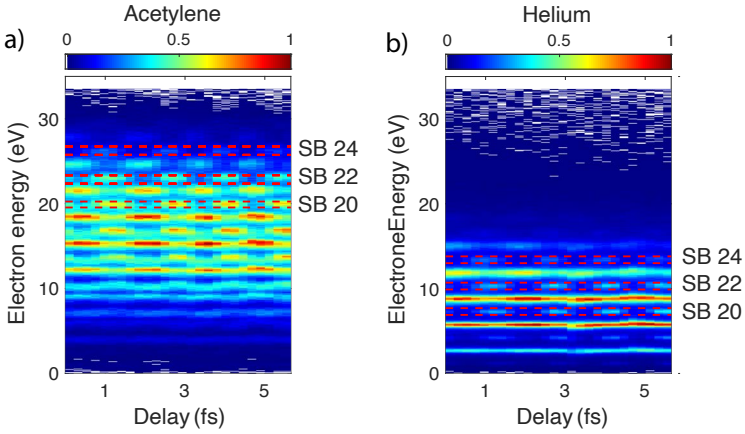


**Figure 6.8:** Simultaneously acquired RABBITT spectrograms for a) Acetylene and b) helium. The sidebands used for the TURTLE ellipse fitting are highlighted.

sideband orders and integration ranges are highlighted for both species. The simultaneous acquisition of the two species allows one to reference the retrieved SB phases with each other in order to cancel out the XUV chirp and to isolate photoionization time delays via Equation (2.8) (see Section 2 for a derivation),

$$\Delta\tau_{2n}^{\text{C}_2\text{H}_2-\text{He}} = \frac{\varphi_{\text{SB}2n}^{\text{C}_2\text{H}_2} - \varphi_{\text{SB}2n}^{\text{He}}}{2\omega_{\text{IR}}}. \quad (6.12)$$

Here,  $\Delta\tau_{2n}^{\text{C}_2\text{H}_2-\text{He}}$ , comprises both, the Wigner and the  $cc$ -contributions. The TURTLE ellipse fits for the retrieval of the phase differences  $\varphi_{\text{SB}2n}^{\text{C}_2\text{H}_2} - \varphi_{\text{SB}2n}^{\text{He}}$  from the He and  $\text{C}_2\text{H}_2$  SB pairs are presented in Figure 6.9 for SB orders 20, 22 and 24. The derived time delays are given in Table 6.2.

Sideband	Delay $\text{C}_2\text{H}_2 - \text{He}$
SB 20	63 as
SB 22	44 as
SB 24	42 as

**Table 6.2:** Photoionization time delays between Acetylene and helium for sidebands 20, 22 and 24, retrieved using Turtle.



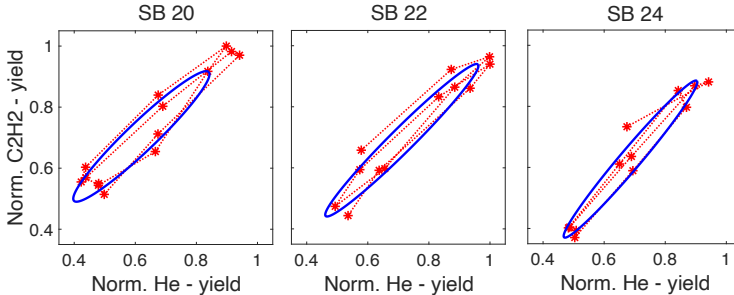


**Figure 6.9:** Turtle ellipse fits of the simultaneously acquired Acetylene-helium RABBITT spectrograms. The Acetylene and helium sideband yield correlations are shown for SB 20, SB 22, and SB 24, together with the corresponding Turtle ellipse fit.

Due to the simultaneous acquisition of the two species and the filtering on only non-dissociated photoionization events, the effective count rates are crucially lower compared to the other measurements carried out during the research work for this thesis. In turn, the integration time per delay step has to be chosen significantly higher, i.e., up to 1 h per step. The stability of the experimental setup, however, sets technical limits for the overall integration time such that only short delay scans can be acquired, e.g., as shown in Figure 6.8. The TURTLE method is excellently suited to retrieve the SB phase differences in such situations, where only few SB oscillation periods are captured. In the sine-fit method, the oscillation frequency has to be fitted, which, particularly for only few delay steps, leads to larger deviations for the retrieved phases. Similarly, in the Fourier method, the spectral phase has to be interpolated at the actual oscillation frequency<sup>1</sup>, as the frequency sampling is very coarse for the few delay steps. In contrast, as long as a full turn of the ellipse is captured, the TURTLE method is unaffected by the sampling and the delays can be reliably retrieved. For the interpretation of the retrieved delays, a collaboration with the institute IMDEA *nanociencia* in Madrid is carried out, however, without conclusive results at the time of writing this thesis.

<sup>1</sup>For short sampling windows in the time domain, the frequency sampling of the Fourier space is very coarse. The actual oscillation frequency ( $2\omega_{IR}$ ) and its phase is most likely not exactly sampled and has to be interpolated.

### 6.3 Outlook

The TURTLE method introduced in this chapter demonstrates that, in principle, neither attosecond light pulses nor an attosecond delay control is needed to retrieve attosecond photoionization time delays. It relaxes the experimental requirements for typical table-top experiments while increasing their accuracy. Section 6.2 presents a cutting-edge RABBIT-type experiment, where the technical limits of the AttoCOLTRIMS setup are reached. The TURTLE method demonstrates a reliable retrieval of the photoionization delays.

The primary playground of the TURTLE method is certainly a high-jitter regime, as in the case of FELs. The only requirement for the technique to work is a two-color XUV field, coarsely synchronized with an optical pulse. Such two-color XUV fields (two harmonics) can be generated by the use of the two slightly detuned undulators, as demonstrated, e.g., in [131]. The phase relation between the two XUV colors does not need to be fixed. The coarse synchronization of XUV and optical light pulses on a femtosecond time scale has already become state-of-the-art in many FEL facilities [128]. A recent study successfully demonstrated an attosecond pulse measurement and shaping using a very similar technique as TURTLE [17].

The investigation of attosecond dynamics at FELs is certainly considered the largest trend in the field of attosecond science. Therefore, the TURTLE constitutes a not only a timely and but also significant contribution towards future studies of photoionization time delays.

## Attosecond photoionization spectroscopy just above threshold

In the previous chapters, new schemes of attosecond interferometry have been presented. Fundamental physical discoveries which are exclusively accessible via these techniques have been discussed. In contrast, this chapter presents *regular* RABBITT measurements. The goal of this chapter is to push the frontiers of RABBITT to a regime where it is only weakly used until now (2020), that is just ionization above threshold. As shown throughout this chapter, the technique allows for detailed monitoring of the excited state dynamics of the target species under investigation.

Section 7.1 presents a RABBITT measurement in helium in the regime from 0 to 2 eV kinetic energy. In this energy regime, the quantum pathways which comprise the absorption of an additional IR photon are resonant with the helium bound excited states. The following sections refer to this measurement. Section 7.2 presents the evaluation of photoionization time delays arising from the helium excited states resonances. Section 7.3 presents an analysis of the femtosecond Stark shift of the helium  $1s4p$  state in the presence of the IR laser field. Section 7.4 applies the angular analysis and the simultaneous fitting procedure, introduced in Chapter 4, to SB 16, which enables the quantification of time delays arising from single-photon ionization.

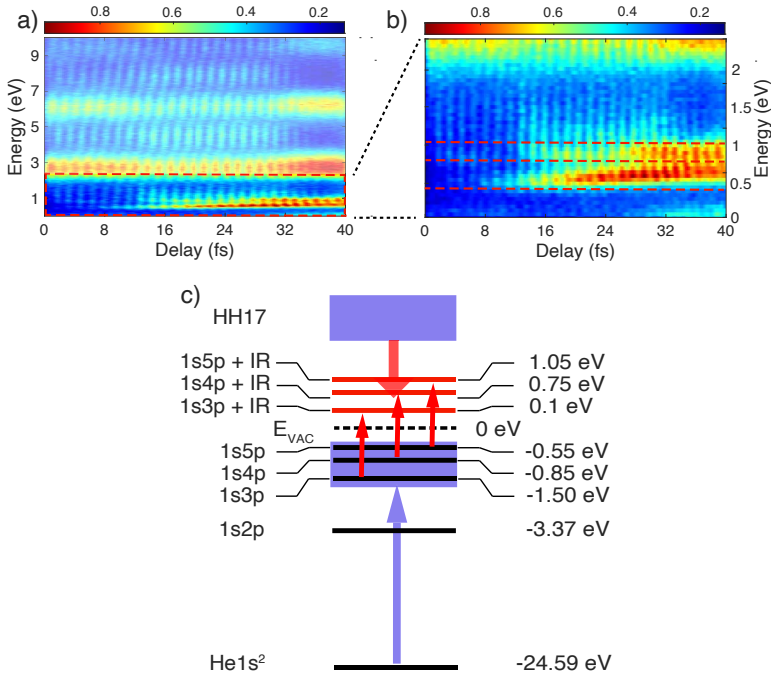


**Figure 7.1:** Signatures of the helium  $1snp$  excited states in the RABBITT experiment. a) RABBITT spectrogram. HH 15 excites the helium  $1s3p$ ,  $1s4p$  and  $1s5p$  states, from which the IR ionizes. b) Zoom into the spectrogram of a) in the highlighted region from 0 eV to 2 eV. Different sub-regions of SB 16 are distinguished. c) Schematic of the two-color photoionization channels via the helium excited states and corresponding energy levels.

## 7.1 Helium RABBITT measurement just above threshold

Figure 7.1 presents a RABBITT measurement in helium. The XUV harmonics are generated from a compressed IR driving pulse with a pulse duration of  $\sim 15$  fs (FWHM) and a center wavelength of 785 nm. A replica of the compressed pulse is also used as dressing field. The configuration of the COLTRIMS (Electric and magnetic field strengths) is adapted for an optimal resolution of photoelectrons with a kinetic energy  $< 5$  eV. Figure 7.1 b) shows a zoom into the highlighted region of Figure 7.1 a) from 0 to 2 eV, where multiple structures become apparent.

SB 16 would lie in the center of this region, at 1 eV. However, in contrast to a normal SB, for which the yield follows the overlap of the XUV and IR pulses, the yield of SB 16 instead follows the flux of the IR after the XUV. The yield continuously increases for larger delays, i.e., where the IR pulse arrives after the XUV. Even several femtoseconds after the overlap, the yield stays constant. For higher SB orders, normal behavior is observed.

For SBs far above threshold ( $E_{kin} > 2\hbar\omega_{IR}$  all contributing quantum pathways comprise an intermediate state in the electronic continuum. Hence, for these SBs, only the simultaneous (non-sequential) exchange of two photons enables the population of the sideband. The presence of both light fields at the same time is required. In contrast, for SB 16, the quantum pathways, which include the additional absorption of an IR photon, comprise a bound intermediate state. The XUV does not ionize but excites a higher-lying bound state. Then, the IR field promotes the bound-continuum transition (ionization). This process can be sequential and its probability depends on the IR flux after the excitation by the XUV. Hence, the later the IR pulse arrives, the more atoms have been excited until the arrival, and the higher the probability that the IR ionizes. On the other hand, if the IR pulse arrives before the XUV, the excited states are not populated at all and no ionization by the IR can take place. However, only in the overlap region yield oscillations are possible, as only here quantum pathways involving stimulated emission are present.

The quantum pathways which are resonant with the helium excited states dominate SB 16. Hence, it can be split into four sub-regions, indicated by the red lines in Figure 7.1 b). The lowest region from 0 to 0.4 eV corresponds to a signature of the  $1s3p$  state. The region from 0.4 to 0.9 eV corresponds to a signature of the  $1s4p$  state and the region from 0.9 to 1.2 eV corresponds to a signature of the  $1s5p$  state. Signatures of other excited states (e.g.,  $1s6p$ ) are not visible. Instead, the highest energetic region above 1.2 eV is dominated by non-resonant quantum pathways, which results in a regular sideband yield that decreases after the overlap. Figure 7.1c) shows a schematic of the different quantum pathways and details the exact energy levels of the helium excited states and the corresponding signatures in the RABBITT spectrogram.

For the driving wavelength of 785 nm, HH 15 has a center energy of 23.7 eV. It lies slightly below the absorption line of the  $1s4p$ -state (23.75 eV), which is populated the most. The  $1s5p$ -absorption line lies still close to the harmonic center, however, as the excitation probability decreases with  $1/n^2$  for the photoexcitation from a  $1s$  to a  $np$ -state, it is populated less. The population of even higher excited states is not observed. The absorption line of the  $1s3p$ -state lies at the lower edge of the harmonic such that it is also scarcely populated. Conceptually, the analysis of the different regions of SB16 is similar to the *Rainbow* RABBIT technique [85, 86], where the SB phase is analyzed continuously as a function of energy within single SBs.

In the following, three effects are analyzed in more detail. First, the photoionization time delays for the resonant photoionization from the different excited states are evaluated. Second, the Stark shift of the  $1s4p$  is analyzed. Third, the angular analysis and fitting procedure introduced in Chapter 4 is carried out, enabling the quantification of time delays arising from single-photon transitions.

## 7.2 Photoionization delays arising from the helium excited states resonances

In order to obtain time delays for the resonant two-photon ionization via the different excited states, the phases of the SB oscillation of the different subregions corresponding to the different excited state signatures have to be retrieved. Figure 7.2 a) shows the yields of the  $1s3p$ ,  $1s4p$  and  $1s5p$  subregions as well as of SB 18, which serves as reference. As the yield of the excited state signatures is increasing towards larger delays, a moving average (average window 9fs) is subtracted before the phase is retrieved via a sinusoidal fit. It has been checked later that the direct retrieval of the phase via Fourier transform of the raw yield gives the same results. Further, the oscillations are split into five windows of 7 fs, which are fitted separately. This split enables a cross-validation that the fitted phases do not depend on the delay them-self, i.e., to rule out any effect due to the overall increase of the yield towards larger delays and due to the removal of the moving average. Furthermore, the split allows for an uncertainty

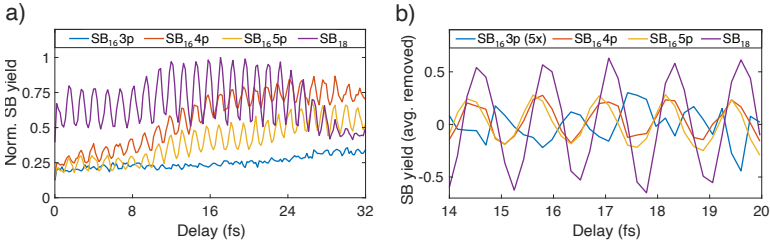


**Figure 7.2:** Sideband oscillations of the helium excited states signatures. a) Yield of SB 16, integrated over the different highlighted regions in Figure 7.1 b), corresponding to the signatures of the different excited states. The integrated yield of SB 18 is shown for comparison. b), Same as a) subtracted by the moving average over a 9 fs window and zoom into the center region of the overlap.

estimate of the retrieved phase via the standard deviation. The yields with removed moving average are illustrated in Figure 7.2 a) for the center window. It can be seen that there is an almost  $\pi$ -phase shift between the  $1s3p$ - and  $1s4p$ -oscillation, as well as only a minor phase shift between the  $1s4p$ - and the  $1s5p$ -yield. In order to obtain photoionization time delays, the phase shifts are divided by  $2\omega_{IR}$ . As the excited state signatures originate from the same SB order, the XUV contribution is considered negligible. The retrieved delays and corresponding standard deviations are shown in Table 7.1.

	$\Delta\tau_{np-n'p}$
$1s3p - 1s4p$	$687 \pm 77$ as
$1s4p - 1s5p$	$9 \pm 35$ as

**Table 7.1:** Time delays between photoionization from the different excited states.

### 7.3 Stark effect

In a detailed viewing of the RABBITT spectrogram, Figure 7.3 a), an energy shift of the different excited state signatures becomes apparent, which follows the overlap of the XUV and IR pulses. Particularly, the central energy of the  $1s4p$ -signature is decreased by 0.2 eV in the center of the envelope. Figure 7.3 b) shows this energy shift as a function of the delay. The

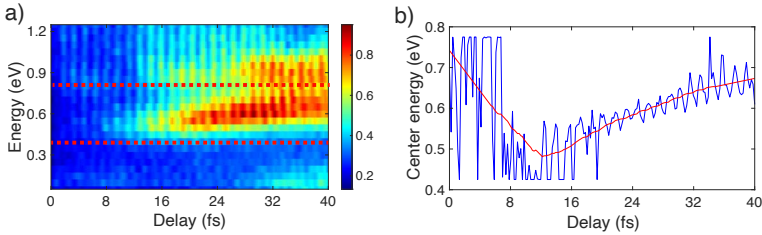


**Figure 7.3:** Energy shift of the helium  $1s4p$ -signature. a) Zoom into the RABBITT spectrogram of Figure 7.1 in the range from 0.2 to 1.2 eV kinetic energy. b) Fitted center energy of the  $1s4p$ -signature as a function of the pump-probe delay. The red line corresponds to a smooth function (Savitzky-Golay-filter) to guide the readers' eye.

center energy of the  $1s4p$ -signature is fitted in each delay step, within the energy range of the corresponding subregion. In detail, a Gaussian function with variable center and width is fitted to the energy spectrum of each delay step in the subregion. In the fit, the center energy is restricted to the boundaries of the subregion. As the overall yield increases towards larger delays, also the fit improves. In turn, the fit uncertainty is larger for small delays.

The energy shift can be explained by the interplay of two contributions: The AC-Stark shift and the ponderomotive energy. The first one corresponds to the energy shift of the bound atomic states and the latter one corresponds to the energy increase of the liberated electron when leaving the high-intensity focal region.

The ponderomotive energy (Equation (2.2)) is  $\sim 10$  meV for the laser wavelength of 785 nm and the estimated intensity of  $2 \cdot 10^{11}$  W/cm<sup>2</sup>. Due to the electrons not being fast enough to leave the laser focus within the pulse duration, only a fraction of the ponderomotive energy can be acquired by the electrons [136]. Hence, the major contribution to the observed energy shift is associated with the AC-Stark shift.

In a detailed study of the AC-Stark effect in helium using transient absorption spectroscopy and similar laser parameters [137], similar results were obtained, i.e., a Stark-shift of the  $1s4p$ -state of up to 0.2 eV, which follows the temporal envelope of the IR pulse. However, for transient absorption spectroscopy, only the energy difference between the excited



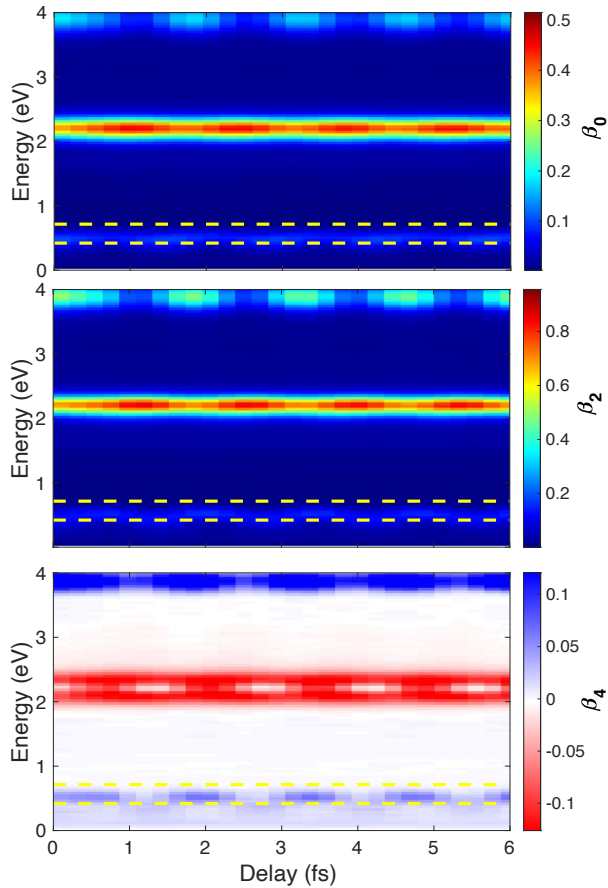


**Figure 7.4:** Experimental anisotropy parameters of the helium RABBITT just above threshold:  $\beta_0$  (top),  $\beta_2$  (centre) and  $\beta_4$  (bottom). The yellow lines indicate the integration range of SB 16. For the narrow harmonics, the two-photon transition of the absorption of HH 15 and additional absorption of an IR photon is non-resonant and non-sequential, as none of the excited state absorption lines overlap with the XUV photon energy.

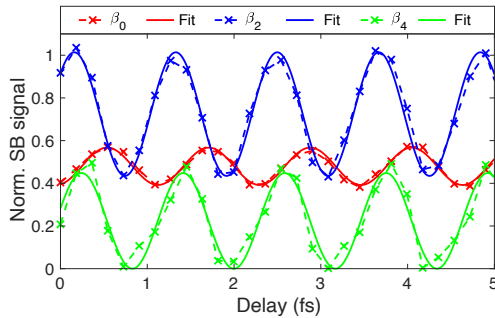


**Figure 7.5:** Simultaneous fit of the sideband anisotropy parameters of SB 16. The integrated sideband anisotropy parameters from Figure 7.4 and the corresponding simultaneous fit of the system of Equations (4.4) - (4.6) (see Section 4.1 for details) are shown.

states and the ground state can be accessed. As, naturally, both states are subjected to a Stark-shift, conclusive statements about the energy shift of a single excited state can not be made, or respectively, only under severe assumptions. In contrast, via photoelectron spectroscopy, the Stark-shift can be accessed assumption-free.

## 7.4 Delays from one-photon ionization

In contrast to the previous sections in this chapter, this section presents a RABBITT experiment in helium using narrow harmonics, generated by an IR driving field with a pulse duration of  $\sim 30$  fs FWHM. In this case, the helium excited states are not efficiently populated. Instead, the non-resonant two-photon ionization leads to a *regular* sideband 16. In detail, due to the slightly longer driving wavelength of 790 nm, HH 15 has a photon energy of 23.55 eV, i.e., it lies exactly in between the absorption lines of the  $1s3p$ - and  $1s4p$  excited states. In this section, the phase slip between  $s$ - and  $d$ -partial waves is determined via the analysis method and fitting procedure introduced in Chapter 4.

Figure 7.4 shows the time-resolved anisotropy parameters  $\beta_0$ ,  $\beta_2$  and  $\beta_4$  of the RABBITT spectrogram. Analog to the experiment in Section 4.1 four quantum pathways are contributing to SB16. In detail, these comprise the two-photon transitions with angular momentum quantum numbers

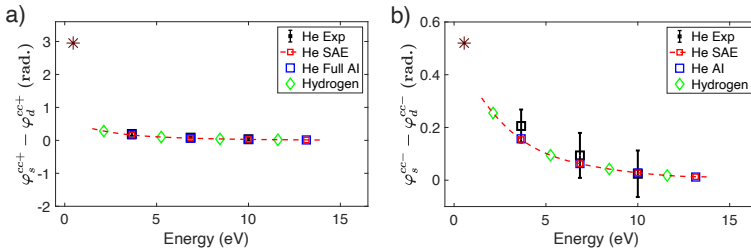


**Figure 7.6:** Phase difference  $\varphi_s^{\pm} - \varphi_d^{\pm}$  including the data points for SB 16, otherwise same as Figures 4.3 and 4.4. The additional data points for SB 16 are highlighted. a) For the absorption case, the IR induced transition corresponds to a *bc*-transition. The retrieved phase separates from the observed *cc*-phase behaviour from Chapter 4. b) For the stimulated emission case, the corresponding IR induced transition corresponds to a *cc*-transition and the data point for SB 16 follows the trend from Chapter 4.

$s \rightarrow p \rightarrow s$  and  $s \rightarrow p \rightarrow d$ , each for absorption of HH 15 and additional absorption of an IR photon as well as for absorption of HH 17 and stimulated emission of an IR photon. In contrast to Chapter 4, the absorption of an IR photon following the absorption of HH 15 can not be considered as a *cc*-transition. Instead, HH 15 rather excites a virtual, bound intermediate state, which is then ionized by the IR, i.e. a *bound-continuum* (*bc*) transition. On the other hand, the stimulated emission of an IR photon following the absorption of HH 17 corresponds to a *cc*-transition.

The analytical expressions for the SB anisotropy parameters, Equations (4.4) -(4.6), are independent of the nature of the contributing quantum pathways (*cc* or *bc*-transitions) and hold for SB 16 as well. Figure 7.5 shows the integrated SB anisotropy parameters and the corresponding simultaneous fit of the amplitudes and phases of the contributing pathways (see Section 4.1 for details). It has to be noted that the split of the retrieved phases into one-photon and two-photon phases for the pathway including a virtual intermediate state has to be done with precaution. In principle, it is conceivable that also the IR excites a virtual state first and then the XUV ionizes. The reasoning which motivates the split into one-photon and two-photon matrix elements as given in Chapter 4 (or in more detail in [29]) is not valid here. Figure 7.6 a) shows the retrieved phase difference  $\varphi_s^{\pm} - \varphi_d^{\pm}$  between the *s*- and *d*-partial waves following the pathway including the absorption of HH 15 and additional absorption of an IR pho-

ton, together with the corresponding *cc*-phase differences for absorption for the higher sideband orders determined in Chapter 4. The additional data point for SB 16 clearly separates from the trend of the *cc*-phase differences observed in Chapter 4. On the other hand, for the phase difference  $\varphi_s^- - \varphi_d^-$  induced by the stimulated emission of an IR photon, the data point for SB 16 follows the trend of the *cc*-phase observed in Chapter 4.

## 7.5 Outlook

Ultrafast photoionization dynamics just above threshold are interesting for two main reasons. i) Generally, large photoionization time delays can be expected, which, in turn, enables a rich potential for an attosecond control. ii) For numerical simulations, the regime just above threshold is challenging. Experimental measurements serve as relevant future benchmarks.

As demonstrated throughout this chapter, attosecond photoionization spectroscopy just above threshold enables the observation of ultrafast excited state dynamics in unprecedented detail. It is demonstrated that RABBITT constitutes an excellent tool for the monitoring of ultrafast population dynamics of different excited states in the target system. The measurement of attosecond photoionization time delays resulting from helium excited state resonances as well as a study of the ultrafast Stark-shift of the helium  $1s4p$ -state have been presented. These studies serve as proof-of-principle experiments for the investigation of excited state dynamics in other, more complex systems. For molecules, the understanding and control of excited state dynamics are essential towards the light-control of chemical reactions. As an example, the decay of an excited state via a conical intersection could be directly monitored.

# Conclusion

In this thesis novel attosecond interferometry schemes have been developed and fundamental physics discoveries presented. Hence, this thesis shall not only expand the scientific knowledge horizon at the time of writing but faithfully contribute to the field of attosecond science in the long-term.

A COLTRIMS detector, combined with an XUV-IR pump-probe delay line has been used to measure time-, energy-, and angle-resolved photoelectron spectra. The developed attosecond interferometry schemes build on the RABBITT technique. In contrast to the latter, the here presented interferometry techniques exploit not only the phase but also the amplitude and modulation depth of the observed oscillations in the delay-dependent photoelectron spectra, in order to retrieve information about the underlying attosecond dynamics.

In the conventional RABBITT technique, photoionization time delays are retrieved via phase differences between angle-integrated sideband oscillations. The angular dependence of the oscillation is only scarcely analyzed. In Chapter 4, an experimental procedure has been presented which enables the quantification of time delays arising from single-photon transitions, particularly by exploiting the sideband angular distribution. To this end, an angle-resolved RABBITT experiment in helium has been carried out. Via a simultaneous fit of the sideband anisotropy parameters, the relative phases of all contributing quantum pathways with different

angular momentum have been retrieved. The phase difference between two-photon quantum pathways following the absorption of the same XUV harmonic allowed for the isolation of time delays arising from the single-photon transitions.

On a high-level perspective, this procedure completes the conventional RABBITT analysis procedure. Making use of the entire angular information of the quantum beating, the complete information about the interfering pathways is retrieved. The found delays demonstrate an angular momentum contribution to the photoionization time delay. When carrying angular momentum, the reduced radial energy share leads to a delay in the emission process. The measured delays, together with numerical simulations and analytical estimates, suggest a universal character of the angular momentum contribution to the photoionization time delay across different chemical species.

Employing narrowband high harmonics, the conventional RABBITT technique leads to long interferograms, which enable a precise phase retrieval. However, typically only short sections of the full interferograms are captured. In Chapter 5 a RABBITT-type experiment employing spectrally broad, overlapping high harmonics has been carried out. While leading to shorter interferograms, the broad harmonics reveal more detailed phase information. In particular, the broad high harmonics enable a beating between one-photon and two-photon quantum pathways, which leads to a  $1\omega$ -oscillation in the photoelectron angular asymmetry, in addition to the  $2\omega$ -oscillation of the angle integrated photoelectron yield. The amplitude and phase of these oscillations enable the retrieval of phase differences, continuously as a function of energy over the full spectral range of the APT.

In the presented experiment the additional phase information allowed the observation of periodic oscillations in the spectral phase of the employed APT. These spectral phase oscillations have been predicted more than 15 years ago and are a consequence of the individual chirp of each harmonic.

Since in RABBITT photoionization time delays are retrieved via actual phase measurements, the question arises if attosecond pump-probe mea-

---

measurements are at all required to achieve attosecond precision. In Chapter 6 the TURTLE method has been developed which demonstrates a retrieval of attosecond delays from RABBITT-type measurements, without attosecond pulses and without attosecond delay control. In turn, the TURTLE method relaxes technical demands for future attosecond experiments and enables XUV-IR pump-probe measurements at large scale facilities, where a femtosecond timing jitter is present.

In the last chapter of this thesis, RABBITT measurements in the regime just above threshold have been presented. These measurements demonstrate the great potential of the technique for the investigation of ultrafast excited state dynamics. The monitoring of ultrafast excited state dynamics is particularly interesting for molecules and the observation of conical intersections.

Finally, at the time of writing this thesis, attosecond spectroscopy experiences a trend towards free-electron lasers [17] and other large scale facilities [138]. The major playground of the here presented interferometry methods are table-top experiments. However, also for the large scale facilities, interferometric measurements play a major role [17, 139]. Therefore, even if certain adaptations may be required, the methods presented in this thesis hopefully contribute to any path that attosecond science may take.





## Author contributions

In this chapter the contributions of Jaco Fuchs to the different journal publications printed in this thesis are listed.

### **Time delays from one-photon transitions in the continuum**

*Jaco Fuchs, Nicolas Douquet, Stefan Donsa, Fernando Martin, Joachim Burgdörfer, Luca Argenti, Laura Cattaneo, Ursula Keller*

Optica (2020).

- Lead of the study
- Main contribution to all results except the SAE and *ab initio* calculations.
- Development of the analysis method and the fitting procedure.
- Conduction and analysis of the experiments.
- Main contribution to the manuscript.

## **Towards the complete phase profiling of attosecond wave packets**

*Jaco Fuchs, Nicolas Douguet, Stefan Donsa, Fernando Martin, Joachim Burgdörfer, Luca Argenti, Laura Cattaneo, Ursula Keller*

Arxiv (2021), submitted to Physical Review Research.

- Lead of the study
- Main contribution to all results except the SAE and *ab initio* calculations.
- Development of the analysis method the phase retrieval procedure.
- Conduction and analysis of the experiments.
- Main contribution to the manuscript.

## **Attosecond resolution from free running interferometric measurements**

*Constantin Krüger\*, Jaco Fuchs\*, Laura Cattaneo and Ursula Keller*

\* These authors contributed equally to this work. Optics express (2020).

- Lead of the study.
- Development of the method.
- Conduction of the experiments.
- Co-analysis of the experiments.
- Contribution to the manuscript.

## References

1. T. H. Maiman, «Stimulated optical radiation in Ruby», *Nature* **187** (1960).
2. D. E. Spence, P. N. Kean, and W. Sibbett, «60-fsec pulse generation from a self-mode-locked Ti:sapphire laser», *Opt. Lett.* **16**, 42 (1991).
3. M. Hentschel, R. Kienberger, C. Spielmann, G. A. Reider, N. Milošević, T. Brabec, P. Corkum, U. Heinzmann, M. Drescher, and F. Krausz, «Attosecond metrology», *Nature* **414**, 509–513 (2001).
4. P. M. Paul, E. S. Toma, P. Breger, G. Mullot, F. Auge, P. Balcou, H. G. Muller, and P. Agostini, «Observation of a train of attosecond pulses from high harmonic generation.», *Science* **292**, 1689–92 (2001).
5. A. L. Cavalieri et al., «Attosecond spectroscopy in condensed matter», *Nature* **449**, 1029–1032 (2007).
6. M. Schultze et al., «Delay in photoemission.», *Science* **328**, 1658–62 (2010).
7. P. Eckle, A. N. Pfeiffer, C. Cirelli, A. Staudte, R. Dörner, H. G. Muller, M. Büttiker, and U. Keller, «Attosecond ionization and tunneling delay time measurements in helium», *Science* **322**, 1525–1529 (2008).
8. S. Haessler et al., «Phase-resolved attosecond near-threshold photoionization of molecular nitrogen», *Phys. Rev. A - At. Mol. Opt. Phys.* **80**, 011404 (2009).

9. I. Jordan, M. Huppert, D. Rattenbacher, M. Peper, D. Jelovina, C. Perry, A. von Conta, A. Schild, and J. Wörner, «Attosecond spectroscopy of liquid water», *Science* **369**, 974–979 (2020).
10. M. Schultze et al., «Attosecond band-gap dynamics in silicon», *Science* **346**, 1348–1352 (2014).
11. M. Schultze et al., «Controlling dielectrics with the electric field of light», *Nature* **493**, 75–78 (2013).
12. M. F. Ciappina et al., «Attosecond physics at the nanoscale», *Reports Prog. Phys.* **80**, 54401 (2017).
13. H. Muller, «Reconstruction of attosecond harmonic beating by interference of two-photon transitions», *Appl. Phys. B* **74**, s17–s21 (2002).
14. A. McPherson, G. Gibson, H. Jara, U. Johann, T. S. Luk, I. A. McIntyre, K. Boyer, and C. K. Rhodes, «Studies of multiphoton production of vacuum-ultraviolet radiation in the rare gases», *J. Opt. Soc. Am. B* **4**, 595 (1987).
15. P. B. Corkum, «Plasma perspective on strong field multiphoton ionization», *Phys. Rev. Lett.* **71**, 1994–1997 (1993).
16. M. Lewenstein, P. Balcou, M. Y. Ivanov, A. L’Huillier, and P. B. Corkum, «Theory of high-harmonic generation by low-frequency laser fields», *Phys. Rev. A* **49**, 2117–2132 (1994).
17. P. K. Maroju et al., «Attosecond pulse shaping using a seeded free-electron laser», *Nature* **578**, 386–391 (2020).
18. Y. Mairesse et al., «Attosecond Synchronization of High-Harmonic Soft X-Rays», *Science* **302**, 1540–1544 (2003).
19. A. L’Huillier, K. J. Schafer, and K. C. Kulander, «Theoretical aspects of intense field harmonic generation», *J. Phys. B At. Mol. Opt. Phys.* **24**, 3315–3341 (1991).
20. A. L’Huillier, K. J. Schafer, and K. C. Kulander, «Higher-order harmonic generation in xenon at 1064 nm: The role of phase matching», *Phys. Rev. Lett.* **66**, 2200–2203 (1991).
21. I. J. Sola et al., «Controlling attosecond electron dynamics by phase-stabilized polarization gating», *Nat. Phys.* **2**, 319–322 (2006).

22. H. Mashiko, S. Gilbertson, C. Li, S. D. Khan, M. M. Shakya, E. Moon, and Z. Chang, «Double Optical Gating of High-Order Harmonic Generation with Carrier-Envelope Phase Stabilized Lasers», *Phys. Rev. Lett.* **100**, 103906 (2008).
23. F. Ferrari, F. Calegari, M. Lucchini, C. Vozzi, S. Stagira, G. Sansone, and M. Nisoli, «High-energy isolated attosecond pulses generated by above-saturation few-cycle fields», *Nat. Photonics* **4**, 875–879 (2010).
24. M. Drescher, «X-ray Pulses Approaching the Attosecond Frontier», *Science* **291**, 1923–1927 (2001).
25. H. Vincenti and F. Quéré, «Attosecond Lighthouses: How To Use Spatiotemporally Coupled Light Fields To Generate Isolated Attosecond Pulses», *Phys. Rev. Lett.* **108**, 113904 (2012).
26. E. Goulielmakis et al., «Real-time observation of valence electron motion», *Nature* **466**, 739–743 (2010).
27. H. Wang, M. Chini, S. Chen, C. H. Zhang, F. He, Y. Cheng, Y. Wu, U. Thumm, and Z. Chang, «Attosecond time-resolved autoionization of argon», *Phys. Rev. Lett.* **105**, 143002 (2010).
28. J. Itatani, F. Quéré, G. L. Yudin, M. Y. Ivanov, F. Krausz, and P. B. Corkum, «Attosecond Streak Camera», *Phys. Rev. Lett.* **88**, 4 (2002).
29. J. M. Dahlström, D. Guénot, K. Klünder, M. Gisselbrecht, J. Mauritson, A. L’Huillier, A. Maquet, and R. Taïeb, «Theory of attosecond delays in laser-assisted photoionization», *Chem. Phys.* **414**, 53–64 (2013).
30. K. Klünder et al., «Probing single-photon ionization on the attosecond time scale», *Phys. Rev. Lett.* **106**, 143002 (2011).
31. E. P. Wigner, «Lower Limit for the Energy Derivative of the Scattering Phase Shift», *Phys. Rev.* **98**, 145–147 (1955).
32. F. T. Smith, «Lifetime matrix in collision theory», *Phys. Rev.* **118**, 349–356 (1960).
33. D. Guénot et al., «Measurements of relative photoemission time delays in noble gas atoms», *J. Phys. B At. Mol. Opt. Phys.* **47**, 245602 (2014).

34. M. Sabbar, S. Heuser, R. Boge, M. Lucchini, T. Carette, E. Lindroth, L. Gallmann, C. Cirelli, and U. Keller, «Resonance Effects in Photoemission Time Delays», *Phys. Rev. Lett.* **115**, 133001 (2015).
35. M. Sabbar, S. Heuser, R. Boge, M. Lucchini, T. Carette, E. Lindroth, L. Gallmann, C. Cirelli, and U. Keller, *Erratum: Resonance Effects in Photoemission Time Delays [Phys. Rev. Lett. 115, 133001 (2015)]*, Nov. 2017.
36. M. Huppert, I. Jordan, D. Baykusheva, A. von Conta, and H. J. Wörner, «Attosecond Delays in Molecular Photoionization», *Phys. Rev. Lett.* **117**, 093001 (2016).
37. M. Ossiander et al., «Attosecond correlation dynamics», *Nat. Phys.* **13**, 280–285 (2017).
38. J. Vos, L. Cattaneo, S. Patchkovskii, T. Zimmermann, C. Cirelli, M. Lucchini, A. Kheifets, A. S. Landsman, and U. Keller, «Orientation-dependent stereo Wigner time delay and electron localization in a small molecule», *Science* **360**, 1326–1330 (2018).
39. L. Cattaneo, J. Vos, R. Y. Bello, A. Palacios, S. Heuser, L. Pedrelli, M. Lucchini, C. Cirelli, F. Martín, and U. Keller, «Attosecond coupled electron and nuclear dynamics in dissociative ionization of H<sub>2</sub>», *Nat. Phys.* **14**, 733–739 (2018).
40. L. Miaja-Avila, C. Lei, M. Aeschlimann, J. L. Gland, M. M. Murnane, H. C. Kapteyn, and G. Saathoff, «Laser-assisted photoelectric effect from surfaces», *Phys. Rev. Lett.* **97**, 113604 (2006).
41. L. Kasmi, M. Lucchini, L. Castiglioni, P. Kliuiev, J. Osterwalder, M. Hengsberger, L. Gallmann, P. Krüger, and U. Keller, «Effective mass effect in attosecond electron transport», *Optica* **4**, 1492 (2017).
42. M. Ossiander et al., «Absolute timing of the photoelectric effect», *Nature* **561**, 374–377 (2018).
43. M. Sabbar, «Attosecond XUV coincidence spectroscopy», PhD thesis (2014).
44. P. M. W. French, J. A. R. Williams, and J. R. Taylor, «Femtosecond pulse generation from a titanium-doped sapphire laser using non-linear external cavity feedback», *Opt. Lett.* **14**, 686 (1989).

45. D. K. Negus, L. Spinelli, N. Goldblatt, and G. Feugnet, «Sub-100 Femtosecond Pulse Generation by Kerr Lens Mode-locking in Ti:Al<sub>2</sub>O<sub>3</sub>», in *Adv. solid state lasers* (1991), SPL7.
46. M. Kakehata, H. Takada, Y. Kobayashi, K. Torizuka, Y. Fujihira, T. Homma, and H. Takahashi, «Single-shot measurement of carrier-envelope phase changes by spectral interferometry», *Opt. Lett.* **26**, 1436 (2001).
47. D. Strickland and G. Mourou, «Compression of amplified chirped optical pulses», *Opt. Commun.* **56**, 219–221 (1985).
48. M. Sabbar, S. Heuser, R. Boge, M. Lucchini, L. Gallmann, C. Cirelli, and U. Keller, «Combining attosecond XUV pulses with coincidence spectroscopy», *Rev. Sci. Instrum.* **85**, 103113 (2014).
49. M. Chini, H. Mashiko, H. Wang, S. Chen, C. Yun, S. Scott, S. Gilbertson, and Z. Chang, «Delay control in attosecond pump-probe experiments», *Opt. Express* **17**, 21459 (2009).
50. R. Dörner, V. Mergel, O. Jagutzki, L. Spielberger, J. Ullrich, R. Moshhammer, and H. Schmidt-Böcking, «Cold Target Recoil Ion Momentum Spectroscopy: a ‘momentum microscope’ to view atomic collision dynamics», *Phys. Rep.* **330**, 95–192 (2000).
51. S. Heuser et al., «Angular dependence of photoemission time delay in helium», *Phys. Rev. A* **94**, 063409 (2016).
52. C. Cirelli et al., «Anisotropic photoemission time delays close to a Fano resonance», *Nat. Commun.* **9**, 955 (2018).
53. D. Busto et al., «Fano’s Propensity Rule in Angle-Resolved Attosecond Pump-Probe Photoionization», *Phys. Rev. Lett.* **123**, 133201 (2019).
54. P. Hockett, «Angle-resolved RABBITT: theory and numerics», *J. Phys. B At. Mol. Opt. Phys.* **50**, 154002 (2017).
55. J. Fuchs, N. Douguet, S. Donsa, F. Martin, J. Burgdörfer, L. Argenti, L. Cattaneo, and U. Keller, «Time delays from one-photon transitions in the continuum», *Optica* **7**, 154 (2020).

56. S. Nagele, R. Pazourek, J. Feist, K. Doblhoff-Dier, C. Lemell, K. Tókési, and J. Burgdörfer, «Time-resolved photoemission by attosecond streaking: Extraction of time information», *J. Phys. B At. Mol. Opt. Phys.* **44**, 081001 (2011).
57. R. Pazourek, S. Nagele, and J. Burgdörfer, «Attosecond chronoscopy of photoemission», *Rev. Mod. Phys.* **87**, 765–802 (2015).
58. G. Sansone et al., «Electron localization following attosecond molecular photoionization», *Nature* **465**, 763–766 (2010).
59. M. Isinger et al., «Photoionization in the time and frequency domain», *Science* **358**, 893–896 (2017).
60. L. Cattaneo, J. Vos, M. Lucchini, L. Gallmann, C. Cirelli, and U. Keller, «Comparison of attosecond streaking and RABBITT», *Opt. Express* **24**, 29060 (2016).
61. J. M. Dahlström, A. L’Huillier, and A. Maquet, «Introduction to attosecond delays in photoionization», *J. Phys. B At. Mol. Opt. Phys.* **45**, 183001 (2012).
62. I. A. Ivanov and A. S. Kheifets, «Angle-dependent time delay in two-color XUV+IR photoemission of He and Ne», *Phys. Rev. A* **96**, 13408 (2017).
63. J. Wätzel, A. S. Moskalenko, Y. Pavlyukh, and J. Berakdar, «Angular resolved time delay in photoemission», *J. Phys. B At. Mol. Opt. Phys.* **48**, 025602 (2015).
64. I. A. Ivanov, J. M. Dahlström, E. Lindroth, and A. S. Kheifets, «On the angular dependence of the photoemission time delay in helium», *arXiv* (2016).
65. A. W. Bray, F. Naseem, and A. S. Kheifets, «Simulation of angular-resolved RABBITT measurements in noble-gas atoms», *Phys. Rev. A* **97**, 63404 (2018).
66. X. Zhao, H. Wei, W.-W. Yu, and C. D. Lin, «Reconstruction of the complex angle-dependent photoionization transition dipole from a laser-dressed streaking experiment», *Phys. Rev. A* **98**, 053404 (2018).



67. Á. Jiménez-Galán, F. Martín, and L. Argenti, «Two-photon finite-pulse model for resonant transitions in attosecond experiments», *Phys. Rev. A* **93**, 023429 (2016).
68. G. Laurent, W. Cao, H. Li, Z. Wang, I. Ben-Itzhak, and C. L. Cocke, «Attosecond control of orbital parity mix interferences and the relative phase of even and odd harmonics in an attosecond pulse train», *Phys. Rev. Lett.* **109**, 083001 (2012).
69. J. J. Moré, «The Levenberg-Marquardt algorithm: Implementation and theory», in *Numer. anal.* (Springer, Berlin, Heidelberg, 2006), pp. 105–116.
70. A. N. Grum-Grzhimailo, M. N. Khaerdinov, and K. Bartschat, «Effects of numerical approximations in the treatment of short-pulse strong-field ionization of atomic hydrogen», *Phys. Rev. A* **88**, 055401 (2013).
71. N. Douguet, A. N. Grum-Grzhimailo, E. V. Gryzlova, E. I. Staroselskaya, J. Venzke, and K. Bartschat, «Photoelectron angular distributions in bichromatic atomic ionization induced by circularly polarized VUV femtosecond pulses», *Phys. Rev. A* **93**, 033402 (2016).
72. X. M. Tong and C. D. Lin, «Empirical formula for static field ionization rates of atoms and molecules by lasers in the barrier-suppression regime», *J. Phys. B At. Mol. Opt. Phys.* **38**, 2593–2600 (2005).
73. M. S. Pindzola et al., «The time-dependent close-coupling method for atomic and molecular collision processes», *J. Phys. B At. Mol. Opt. Phys.* **40**, R39–R60 (2007).
74. T. N. Rescigno and C. W. McCurdy, «Numerical grid methods for quantum-mechanical scattering problems», *Phys. Rev. A* **62**, 032706 (2000).
75. J. Feist, S. Nagele, R. Pazourek, E. Persson, B. I. Schneider, L. A. Collins, and J. Burgdörfer, «Nonsequential two-photon double ionization of helium», *Phys. Rev. A* **77**, 043420 (2008).
76. S. Donsa, I. Brezinová, H. Ni, J. Feist, and J. Burgdörfer, «Polarization tagging of two-photon double ionization by elliptically polarized XUV pulses», *Phys. Rev. A* **99**, 023413 (2019).

77. J. Vinbladh, J. M. Dahlström, and E. Lindroth, «Many-body calculations of two-photon, two-color matrix elements for attosecond delays», *Phys. Rev. A* **100**, 043424 (2019).
78. U. Heinzmann and J. H. Dil, «Spinorbit-induced photoelectron spin polarization in angle-resolved photoemission from both atomic and condensed matter targets», *J. Phys. Condens. Matter* **24**, 173001 (2012).
79. U. Heinzmann, *Attosecond Physics*, Vol. 177, Springer Series in Optical Sciences (Springer Berlin Heidelberg, Berlin, Heidelberg, 2013), pp. 231–253.
80. M. Fanciulli, H. Volfová, S. Muff, J. Braun, H. Ebert, J. Minár, U. Heinzmann, and J. H. Dil, «Spin Polarization and Attosecond Time Delay in Photoemission from Spin Degenerate States of Solids», *Phys. Rev. Lett.* **118**, 067402 (2017).
81. L. H. Haber, B. Doughty, and S. R. Leone, «Energy-dependent photoelectron angular distributions of two-color two-photon above threshold ionization of atomic helium», *Phys. Rev. A* **84**, 013416 (2011).
82. M. Lucchini, A. Ludwig, T. Zimmermann, L. Kasmi, J. Herrmann, A. Scrinzi, A. S. Landsman, L. Gallmann, and U. Keller, «Anisotropic emission in quantum-beat spectroscopy of helium excited states», *Phys. Rev. A* **91**, 063406 (2015).
83. G. Wentzel, «Eine Verallgemeinerung der Quantenbedingungen für die Zwecke der Wellenmechanik», *Zeitschrift für Phys.* **38**, 518–529 (1926).
84. H. A. Kramers, «Wellenmechanik und halbzahlige Quantisierung», *Zeitschrift für Phys.* **39**, 828–840 (1926).
85. V. Gruson et al., «Attosecond dynamics through a Fano resonance: Monitoring the birth of a photoelectron», *Science* **354**, 734–738 (2016).
86. D. Busto et al., «Time–frequency representation of autoionization dynamics in helium», *J. Phys. B At. Mol. Opt. Phys.* **51**, 044002 (2018).

87. R. Locher, L. Castiglioni, M. Lucchini, M. Greif, L. Gallmann, J. Osterwalder, M. Hengsberger, and U. Keller, «Energy-dependent photoemission delays from noble metal surfaces by attosecond interferometry», *Optica* **2**, 405 (2015).
88. R. Pazourek, J. Feist, S. Nagele, and J. Burgdörfer, «Attosecond Streaking of Correlated Two-Electron Transitions in Helium», *Phys. Rev. Lett.* **108**, 163001 (2012).
89. C. Marante, M. Klinker, T. Kjellsson, E. Lindroth, J. González-Vázquez, L. Argenti, and F. Martín, «Photoionization using the xchem approach: Total and partial cross sections of Ne and resonance parameters above the  $2s^2 2p^5$  threshold», *Phys. Rev. A* **96**, 022507 (2017).
90. M. Kotur et al., «Spectral phase measurement of a Fano resonance using tunable attosecond pulses», *Nat. Commun.* **7**, 10566 (2016).
91. V. Stooß, S. M. Cavaletto, S. Donsa, A. Blättermann, P. Birk, C. H. Keitel, I. Březinová, J. Burgdörfer, C. Ott, and T. Pfeifer, «Real-Time Reconstruction of the Strong-Field-Driven Dipole Response», *Phys. Rev. Lett.* **121**, 173005 (2018).
92. D. Polli et al., «Conical intersection dynamics of the primary photoisomerization event in vision», *Nature* **467**, 440–443 (2010).
93. L. Barreau et al., «Disentangling Spectral Phases of Interfering Autoionizing States from Attosecond Interferometric Measurements», *Phys. Rev. Lett.* **122**, 253203 (2019).
94. S. Donsa, N. Douguet, J. Burgdörfer, I. Březinová, and L. Argenti, «Circular Holographic Ionization-Phase Meter», *Phys. Rev. Lett.* **123**, 133203 (2019).
95. G. Laurent, W. Cao, I. Ben-Itzhak, and C. L. Cocke, «Attosecond pulse characterization», *Opt. Express* **21**, 16914 (2013).
96. V. Loriot et al., «Angularly resolved RABBITT using a second harmonic pulse», *J. Opt. (United Kingdom)* **19**, 114003 (2017).
97. V. Loriot, A. Marciniak, S. Nandi, G. Karras, M. Hervé, E. Constant, E. Plésiat, A. Palacios, F. Martín, and F. Lépine, «High harmonic generation-2  $\omega$  attosecond stereo-photoionization interferometry in N 2», *J. Phys. Photonics* **2**, 024003 (2020).

98. H. J. Shin, D. G. Lee, Y. H. Cha, K. H. Hong, and C. H. Nam, «Generation of Nonadiabatic Blueshift of High Harmonics in an Intense Femtosecond Laser Field», *Phys. Rev. Lett.* **83**, 2544–2547 (1999).
99. H. J. Shin, D. G. Lee, Y. H. Cha, J. H. Kim, K. H. Hong, and C. H. Nam, «Nonadiabatic blueshift of high-order harmonics from Ar and Ne atoms in an intense femtosecond laser field», *Phys. Rev. A - At. Mol. Opt. Phys.* **63**, 9 (2001).
100. Y. Mairesse and F. Quéré, «Frequency-resolved optical gating for complete reconstruction of attosecond bursts», *Phys. Rev. A* **71**, 011401 (2005).
101. S. Haessler, L. B. Bom, O. Gobert, J. F. Hergott, F. Lepetit, M. Perdrix, B. Carré, T. Ozaki, and P. Salières, «Femtosecond envelope of the high-harmonic emission from ablation plasmas», *J. Phys. B At. Mol. Opt. Phys.* **45**, 074012 (2012).
102. F. Ardana-Lamas, C. Erny, A. G. Stepanov, I. Gorgisyan, P. Juranić, R. Abela, and C. P. Hauri, «Temporal characterization of individual harmonics of an attosecond pulse train by THz streaking», *Phys. Rev. A* **93**, 043838 (2016).
103. K. T. Kim, C. Zhang, T. Ruchon, J. F. Hergott, T. Auguste, D. M. Villeneuve, P. B. Corkum, and F. Quéré, «Photonic streaking of attosecond pulse trains», *Nat. Photonics* **7**, 651–656 (2013).
104. K. Varjú et al., «Frequency chirp of harmonic and attosecond pulses», in *J. mod. opt.* Vol. 52 (Jan. 2005), pp. 379–394.
105. J. Mauritsson, P. Johnsson, R. López-Martens, K. Varjú, W. Kornelis, J. Biegert, U. Keller, M. B. Gaarde, K. J. Schafer, and A. L’Huillier, «Measurement and control of the frequency chirp rate of high-order harmonic pulses», *Phys. Rev. A* **70**, 021801 (2004).
106. S. Nagele, R. Pazourek, J. Feist, K. Doblhoff-Dier, C. Lemell, K. Tórkési, and J. Burgdörfer, «Time-resolved photoemission by attosecond streaking: extraction of time information», *J. Phys. B At. Mol. Opt. Phys.* **44**, 081001 (2011).
107. V. Véniard, R. Taïeb, and A. Maquet, «Phase dependence of (N +1)-color (N >1) ir-uv photoionization of atoms with higher harmonics», *Phys. Rev. A* **54**, 721–728 (1996).

108. S. Donsa, I. Březinová, H. Ni, J. Feist, and J. Burgdörfer, «Polarization tagging of two-photon double ionization by elliptically polarized XUV pulses», *Phys. Rev. A* **99**, 023413 (2019).
109. M. Lewenstein, P. Salières, and A. L’Huillier, «Phase of the atomic polarization in high-order harmonic generation», *Phys. Rev. A* **52**, 4747–4754 (1995).
110. M. B. Gaarde and K. J. Schafer, «Quantum path distributions for high-order harmonics in rare gas atoms», *Phys. Rev. A - At. Mol. Opt. Phys.* **65**, 4 (2002).
111. D. You et al., «New Method for Measuring Angle-Resolved Phases in Photoemission», *Phys. Rev. X* **10**, 31070–31071 (2020).
112. J. Gagnon, E. Goulielmakis, and V. Yakovlev, «The accurate FROG characterization of attosecond pulses from streaking measurements», *Appl. Phys. B* **92**, 25–32 (2008).
113. S. Pabst and J. M. Dahlström, «Eliminating the dipole phase in attosecond pulse characterization using Rydberg wave packets», *Phys. Rev. A* **94**, 013411 (2016).
114. M. Chini, S. Gilbertson, S. D. Khan, and Z. Chang, «Characterizing ultrabroadband attosecond lasers», *Opt. Express* **18**, 13006 (2010).
115. C. Krüger, J. Fuchs, L. Cattaneo, and U. Keller, «Attosecond resolution from free running interferometric measurements», *Opt. Express* **28**, 12862 (2020).
116. M. Ferray, A. L’Huillier, X. F. Li, L. A. Lompre, G. Mainfray, and C. Manus, «Multiple-harmonic conversion of 1064 nm radiation in rare gases», *J. Phys. B At. Mol. Opt. Phys.* **21**, L31–L35 (1988).
117. P. Antoine, A. L’Huillier, and M. Lewenstein, «Attosecond Pulse Trains Using High-Order Harmonics», *Phys. Rev. Lett.* **77**, 1234–1237 (1996).
118. M. Drescher, M. Hentschel, R. Kienberger, M. Uiberacker, V. Yakovlev, A. Scrinzi, T. Westerwalbesloh, U. Kleineberg, U. Heinzmann, and F. Krausz, «Time-resolved atomic inner-shell spectroscopy», *Nature* **419**, 803–807 (2002).

119. E. Goulielmakis, «Direct Measurement of Light Waves», *Science* **305**, 1267–1269 (2004).
120. C. Palatchi, J. M. Dahlström, A. S. Kheifets, I. A. Ivanov, D. M. Canaday, P. Agostini, and L. F. DiMauro, «Atomic delay in helium, neon, argon and krypton», *J. Phys. B At. Mol. Opt. Phys.* **47**, 245003 (2014).
121. S. Haessler et al., «Attosecond imaging of molecular electronic wavepackets», *Nat. Phys.* **6**, 200–206 (2010).
122. F. Calegari et al., «Ultrafast electron dynamics in phenylalanine initiated by attosecond pulses», *Science* **346**, 336–339 (2014).
123. M. Krüger, M. Schenk, and P. Hommelhoff, «Attosecond control of electrons emitted from a nanoscale metal tip», *Nature* **475**, 78–81 (2011).
124. J. White and Z. Chang, «Attosecond streaking phase retrieval with neural network», *Opt. Express* **27**, 4799 (2019).
125. L. Pedrelli, P. D. Keathley, L. Cattaneo, F. X. Kärtner, and U. Keller, «Complete phase retrieval of photoelectron wavepackets», *New J. Phys.* **22**, 053028 (2020).
126. M. Isinger, D. Busto, S. Mikaelsson, S. Zhong, C. Guo, P. Salières, C. L. Arnold, A. L’Huillier, and M. Gisselbrecht, «Accuracy and precision of the RABBIT technique», *Philos. Trans. R. Soc. A Math. Phys. Eng. Sci.* **377**, 20170475 (2019).
127. G. T. Foster, J. B. Fixler, J. M. McGuirk, and M. A. Kasevich, «Method of phase extraction between coupled atom interferometers using ellipse-specific fitting», *Opt. Lett.* **27**, 951 (2002).
128. E. Savelyev et al., «Jitter-correction for IR/UV-XUV pump-probe experiments at the FLASH free-electron laser», *New J. Phys.* **19**, 043009 (2017).
129. H.-S. Kang et al., «FEL performance achieved at PAL-XFEL using a three-chicane bunch compression scheme», *J. Synchrotron Radiat.* **26**, 1127–1138 (2019).
130. M. B. Danailov et al., «Towards jitter-free pump-probe measurements at seeded free electron laser facilities», *Opt. Express* **22**, 12869 (2014).

- 
131. J. Duris et al., «Tunable isolated attosecond X-ray pulses with gigawatt peak power from a free-electron laser», *Nat. Photonics* **14**, 30–36 (2020).
  132. L. L. Lazzarino et al., «Shaping femtosecond laser pulses at short wavelength with grazing-incidence optics», *Opt. Express* **27**, 13479 (2019).
  133. F. Schlaepfer, M. Volkov, N. Hartmann, A. Niedermayr, Z. Schumacher, L. Gallmann, and U. Keller, «Phase stabilization of an attosecond beamline combining two IR colors», *Opt. Express* **27**, 22385 (2019).
  134. *fminsearchbnd, fminsearchcon - File Exchange - MATLAB Central*.
  135. N. Hartmann, S. Bhattacharyya, F. Schlaepfer, M. Volkov, Z. Schumacher, M. Lucchini, L. Gallmann, U. Rothlisberger, and U. Keller, «Ultrafast nuclear dynamics of the acetylene cation C<sub>2</sub>H<sub>2</sub><sup>+</sup> and its impact on the infrared probe pulse induced C-H bond breaking efficiency», *Phys. Chem. Chem. Phys.* **21**, 18380–18385 (2019).
  136. P. H. Bucksbaum, R. R. Freeman, M. Bashkansky, and T. J. McIlrath, «Role of the ponderomotive potential in above-threshold ionization», *J. Opt. Soc. Am. B* **4**, 760 (1987).
  137. M. Chini, B. Zhao, H. Wang, Y. Cheng, S. X. Hu, and Z. Chang, «Sub-cycle ac Stark Shift of Helium Excited States Probed with Isolated Attosecond Pulses», *Phys. Rev. Lett.* **109**, 073601 (2012).
  138. S. Kühn et al., «The ELI-ALPS facility: the next generation of attosecond sources», *J. Phys. B At. Mol. Opt. Phys.* **50**, 132002 (2017).
  139. D. Hammerland et al., «Reconstruction of attosecond pulses in the presence of interfering dressing fields using a 100 kHz laser system at ELI-ALPS», *J. Phys. B At. Mol. Opt. Phys.* **52**, 23LT01 (2019).





# Curriculum Vitæ

Name Jaco Fuchs  
Date of Birth 20<sup>th</sup> September 1993  
Citizenship German

## Education

Feb. 2017 - Feb 2021 Doctoral studies, ETH Zürich, Switzerland  
Sept. 2014 - Sept. 2016 Master in Physics, Universität Stuttgart, Deutschland  
Sept. 2011 - Sept. 2014 Bachelor in Physics, Universität Stuttgart, Deutschland  
Sept. 2003 - Aug. 2011 Allgemeine Hochschulreife, Backnang, Deutschland

## Research and Professional Experience

Feb. 2017- Feb. 2021 Doctoral studies at the *Ultrafast Laser Physics* group, supervised by Prof. Ursula Keller, ETH Zürich, Switzerland.  
*"Novel schemes for attosecond interferometry"*  
Feb. 2017- Feb. 2021 Teaching assistant of the Department of Physics, ETH Zürich, Zürich, Switzerland.  
Okt. 2015 - Sept. 2016 Master thesis at the 2. *Institut für theoretische Physik* supervised by Prof. Udo Seifert, Universität Stuttgart.  
*"Information und thermodynamics of neurons"*  
Apr. 2014 - Sept. 2014 Bachelor thesis at the 4. *Physikalisches Institut* supervised by Prof. Harald Giessen, Universität Stuttgart.  
*"Nonlinear plasmonics"*

## Awards

May 2020 *Maiman award*  
CLEO conference, San Jose, USA  
Feb. 2020 *KPMG Ideation challenge*, Swiss champion  
Zürich, Switzerland



## Acknowledgements

I would like to devote these last pages to thank all people who supported me during my PhD work. The past four years at ETH have been an intense and as well as fantastic time. This thesis would not have been possible without you.

First of all, I would like to thank Prof. Ursula Keller. You gave me both freedom and support, and from both a lot! This freedom was definitely not easy to handle, but looking back, I learned so much from it. I am truly thankful.

Second, I would like to thank Prof. Anne L'Huillier for being the co-examiner for this thesis. I know that it is not the easiest piece of literature to read. I strongly hope that you can take some fruitful thoughts from it.

Next, I would like to thank my co-authors from the "cc"- and  $1\omega$ -paper. I am happy that we could drive our collaboration for more than three years. Meanwhile, 6 out of the 8 collaborators are/became professors/group leaders. There was definitely a lot of brainpower in this setting, and it was a great pleasure to be a part of it. Special thanks go to Prof. Luca Argenti. You always found the right arguments, particularly in challenging situations. Most importantly, we share the same passion for writing *spicy* texts.

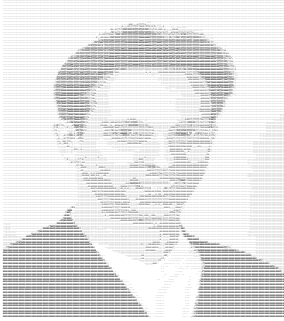
One of the most important persons contributing to this thesis was Dr. Laura Cattaneo. After little issues in the beginning, I think that we had a great time together in the COLTRIMS team. You always had an open ear if needed and you always had the best advice, both private and work-related. I wish you all the best for your future academic career and your new family!

On the same lines, I would like to gratefully thank my master student Constantin Krüger. It was a pleasure to work with you for almost one year. I think nobody else could have handled my chaotic supervision style. I was impressed by you many times. I will always remember how you asked if we can give our technique an animal name. I replied something

like," you could try backward engineering starting with a list of all animal names from Google" - I was just joking, perhaps even with some sarcasm. A few hours later, you presented TURTLE.

Next, I would like to express deep gratitude towards all current and former ULP group members. It is fantastic to work in such a group of smart minds. Luca, no pain, no gain:D I will always remember how you dreamed of putting the COLTRIMS in a ball of aluminum foil and roll it away. Benni, you were always up for a discussion, any topic, any time. I still think you should become a professor at some point. I am looking forward to the next multi-pitch with you. Arthur, it was fantastic to discuss our own state-of-the-art crevasse rescue techniques with you and how our little competitions inspired our climbing. Francesco, you were like a career mentor for me. I hope we can still make it to Seoul once:D Zeno and Sergej, you were always so helpful and you are such a great team. I strongly hope that the surface chamber will pay off - you deserve it. Sandra Schmid, you give us so much, but you hardly get anything back from us. You are the good soul of this group. Thank you very much for all your help! Lukas Gallmann, thanks for many interesting lunch-time discussions. Leo, let's go for some more Bruchharsch! And, of course, I would like to thank all others for a great time: Ajanta, Alexander, Aline, Andreas, Carolin, Cesare, Chris, Dominik, Erik, Fabian, Fabschla, Ivan, Jacob, Janni, Jochen, Jonas, Justas, Lamia, Lukas, Marco, Matthias, Micha, Nadja, Nico, Özgür, Pierre, Sandro C., Sandro L. and Stefan.

My final words go to my family and girlfriend. My parents, Sonia and Hasi, supported me along any way that I took and in every situation, unconditionally. In difficult periods I could always refill my batteries on our black couch. You are the main reason that I made it to where I am now. Finally, I would like to thank my girlfriend Ladina. You shared a large time of my PhD with me and I hope this is just the beginning. Thank you very much for your endless patience, understanding and love!



Zurich, January 2021

*Jaco Fuchs*